ENERGY EFFICIENCY ANALYSIS, PERFORMANCE EVALUATION AND MULTISCALE MODELLING OF CAPACITIVE DEIONIZATION

By

LI WANG

Dissertation
Submitted to the Faculty of the
Graduate School of Vanderbilt University
in partial fulfillment of the requirements
for the degree of

DOCTOR OF PHILOSOPHY
in

Environmental Engineering

December 14, 2019

Nashville, Tennessee

Approved:

Shihong Lin, Ph.D.
Peter Pintauro, Ph.D.
George Hornberger, Ph.D.
Alan Bowers, Ph.D.
Kelsey Hatzell, Ph.D.

To the family and friends
who encouraged me along the way

ACKNOWLEDGEMENTS

I would like to thank my advisor, Dr. Shihong Lin for his support and guidance over the past four years. He encouraged me to pursue new subjects and provided a research environment that has a lot of flexibility and freedom. In addition, he infiltrates me with a mind-set of critical thinking and of being fearless in changing the status quo in research. His enthusiasm towards work and research also affects me profoundly in the long term of academic career. I benefit tremendously from the adviser-advisee relationship with him. I would also like to extend my appreciation to the committee members, Drs. Peter Pintauro, George Hornberger, Alan Bowers, and Kelsey Hatzell, for the insights and generous research support you have provided over the years.

I would like to thank my colleagues who have shared fruitful discussions and assistances in experimental work. There are too many to name. To Yuxi, Zhangxin, Yuanzhe, Kofi, Drew and Ruoyu, thank you for countless hotpots, and for making the lab cheerful and reliable.

Finally, I would like to thank my parents and family for unconditional love and support. Having me as the only child, my parents sacrifice a lot to support me to study abroad. Though we merely discuss my study and research, they are always caring which powers me to move forward. I am so lucky that my parents trust and support me in every major decision I made.

I sincerely thank everyone along this journey!

TABLE OF CONTENTS

Page

LIST OF TABLES

Table Page

LIST OF FIGURES

Figure Page

NOMENCLATURE

Abbreviation/Symbol	Description
α	Charge dependence coefficient of Stern capacitance
Λ	Charge efficiency
p_{sp}	Spacer porosity
p_{ma}	Electrode macroporosity
p_{mi}	Electrode microporosity
Δg	Specific Gibbs free energy of separation
AC	Activated carbon
ACC	Activated carbon cloth
ASAR	Average salt adsorption rate
c_0	Feed concentration
c_B	Brine concentration
c_D	Dilute concentration
$C_{st,vol,0}$	Volumetric stern layer capacitance at zero charge
CC	Constant current
CV	Constant voltage
CDI	Capacitive deionization
D_e	Effective diffusion coefficient
D_{mem}	Diffusion coefficient in ion exchange membrane
EDL	Electrical double layer
FCDI	Flow-electrode capacitive deionization
GCS	Gouy-Chapman-Stern
IEM	Ion exchange membrane
L_{elec}	Electrode thickness
L_m	Ion exchange membrane thickness
L_{sp}	Spacer thickness
M	Total mass of electrodes
MCDI	Membrane capacitive deionization
mD	Modified Donnan
N	Number of electrode pair
$R_{contact}$	Specific contact and external resitance
$R_{electrode}$	Specific electrode resistance
RC	Reverse current
RO	Reverse osmosis
SEC	Specific energy consumption
TEE	Thermodynamic energy efficiency
WR	Water recovery
X	Intrinsic charge of ion exchange membrane
ZV	Zero voltage

CHAPTER 1

INTRODUCTION

1.1. Overview

Capacitive deionization (CDI) is an emerging technology that uses charged porous electrodes to electrostatically remove ions from feed water. For a typical flow-by CDI, it consists of two porous electrodes with a spacer channel in between where water passes by. It is operated repeatedly in charge and discharge steps.[1] Upon charging the electrodes, ions migrate to the electrodes and form the electrical double layers (EDLs) at the interface between the electrode matrix and the solution.[2] When the electrodes become saturated, they can be regenerated by desorbing the stored ions into a brine stream.

Because CDI is powered by low-voltage (~1.2 V) electric energy, it is readily integrated with various renewable energy sources like solar energy,[3] which enables CDI a wide range of potential applications, such as portable fresh water devices, mobile desalination stations for disaster response, and for those remote or developing areas where access to grid power is limited.[4]

In addition to water desalination, CDI also has the great potential for removing ionic impurities from water. CDI can extract ions of all types from water, including sodium, calcium, magnesium, chloride, sulfate, and fluoride. Several studies have suggested that CDI selectively removes some impurities relative to sodium chloride.[5-7]

Compared to the most widely used technologies for water desalination such as membrane processes (reverse osmosis), and thermal process (multi-stage flash distillation, multi-effect evaporation and et al.), CDI is a low pressure and low temperature separation process. Therefore, CDI does not require expensive auxiliary equipment and become capitally economical. In addition, CDI has been claimed to be an energy-efficient process for desalting feed water with low to moderate salinity (e.g. brackish water and wastewater), especially considering possible energy recovery during the discharge step.[8, 9]

A recent major development of CDI is the introduction of ion exchange membranes (IEMs) to the CDI cell by inserting IEMs in front of the porous electrodes. This configuration is called membrane CDI (MCDI). Several advantages over CDI have been testified with MCDI, including

enhanced charge efficiency,[10, 11] suppressed side reactions,[12] and increased salt adsorption capacity.[1] The inserted IEMs prevent co-ions (i.e. ions with same charge with electrode) from being repelled to the spacer channel. Here, the charge efficiency is defined as the number of ions per electrode stored in the capacitor.[13]

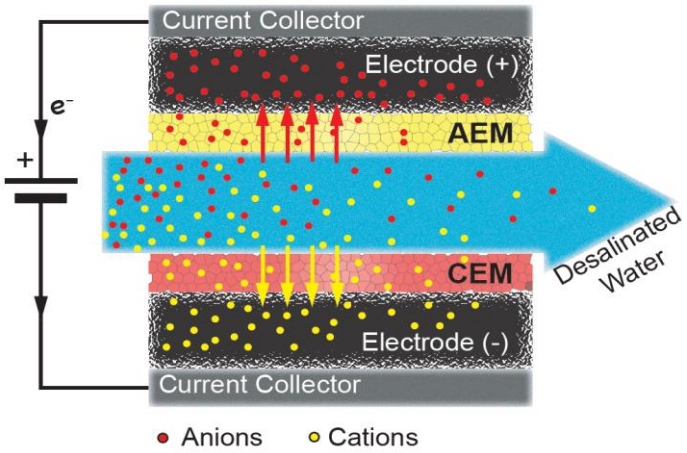

Figure 1.1 Schematic of a typical flow-by capacitive deionization with ion exchange.

1.2. CDI Fundamentals

For the theoretical analysis, we consider two different kinds of pores in the carbon electrode: 1) micropores where EDLs form and ions stored; 2) macropores that serves as pathways for ion transport.

To model the ion storage, EDL theory is employed in our study. The classic Gouy-Chapman-Stern (GCS) model is found problematic when dealing with ion storages in the micropores. Instead, the modified Donnan (mD) model is used. The dynamics of ion transport is modelled with Nernst-Planck (NP) equation, which describes the ion transport from the spacer channel towards the micropores of the electrodes. Details are discussed in the following section.

1.2.1. Electrical double layer theory

To describe the ion adsorption in the EDLs, the classic GCS model is often used. The theory assumes that the electrode is ideally polarized and the electrode surface is a flat plate. It is composed of three layers: the carbon surface, the Stern layer and the diffuse layer. Electrical charges accumulate at the carbon electrode surface, to compensate such charged ions are stored in the diffuse layer with Stern layer in between the charged electrode surface and the diffuse layer. The Stern layer is a charge-free layer, which is introduced because the ions cannot infinitely approach the electrode surface due to the hydration shell of the charged ions.

Given the fact that ions are stored in the micorpores of electrode that have dimensions of less than 2 nm, the diffuse layer is strongly overlapping. We will explain this by a simple calculation. The salt concentrations are usually low in CDI. According to the GCS model, the Debye length, which is a measure of the thickness of the diffuse layer, is about 3 nm when salt concentration is 10 mM at 293 K. The diffuse layer is 2 to 3 times of the Debye length. In that sense, the EDLs are strongly overlapping, and GCS model is not the best approach to describe the ion storage in CDI.

Following the pioneering work by Biesheuvel et al., the mD model that assumes a constant electrical potential in the micropores is used in our study.[10] Similar to the GCS model, an charge-free Stern layer is included between the charged carbon electrode matrix and the electrolyte-filled micropores. When charging the electrode matrix, the micropores begin to preferentially adsorbthe ions with opposite charges (i.e. counter ions). This process is accompanied by the repelling of co-ions (i.e. ions with same charges) to the macropores that are outside of the micropores. Within the macropores, charge neutrality is maintained, meaning that cations and anions have the same equivalent concentration.

1.2.2. Ion transport

The dynamics of ion transport can be modelled by coupling the ion storage (mD theory) and the ion transport (Nernst-Planck equation). The later is used to describe the ions transport through the spacer channel, and across the IEMs when modelling MCDI. This equation is expressed as:

$$J_i = -D_i\left(\frac{\partial c_i}{\partial x} + z_i c_i \frac{\partial \phi}{\partial x}\right) \quad (1.1)$$

where J_i is the flux of ion I, D_i is the diffusion coefficient, c_i is the concentration, z_i is the ion charge, ϕ is the dimensionless electrical potential (i.e. normalize by the thermal energy, 25.6 mV at room temperature), and x is the distance along the transport pathway which is usually only considers the direction perpendicular to the spacer channel.

CDI cells can be operated in several different schemes in terms of charging methods. Two most commonly applied methods are constant voltage and constant current for the charging step.

In the mode of constant voltage (CV) charging, a constant voltage is applied across the CDI cell, as shown in Figure 1.2 (A). As a result, current spikes immediately before exponentially decay to approach zero. Because of the transport of electrical current, ions migrate to the pores of the electrodes. The effluent salinity decreases sharply then rises up as the electrical current diminishes. When no more ions being removed, the electrodes have to be regenerated by discharging the cell. Often times, the discharge is carried out by short-circuiting both electrodes or applying a zero voltage across the cell. Similar to the charging step, the magnitude of discharge current spikes up but in a different direction as opposed to the charging step. The effluent salinity increases before equating the feed salinity. For a dynamic steady state, usually after a few charging/discharge cycles, the salt removed during the charging step equals that released in the discharge step.

Another common operation is to apply constant current (CC) for the charging step as sketched in Fig 1.2 (B). This approach is usually with MCDI, as the effluent salinity remains at a fairly stable level. As the spacer salinity decreases, and the ions stores in the electrode pores, the cell voltage increases continuously. Similarly, it can be discharged at a zero voltage (or equally short-circuited).

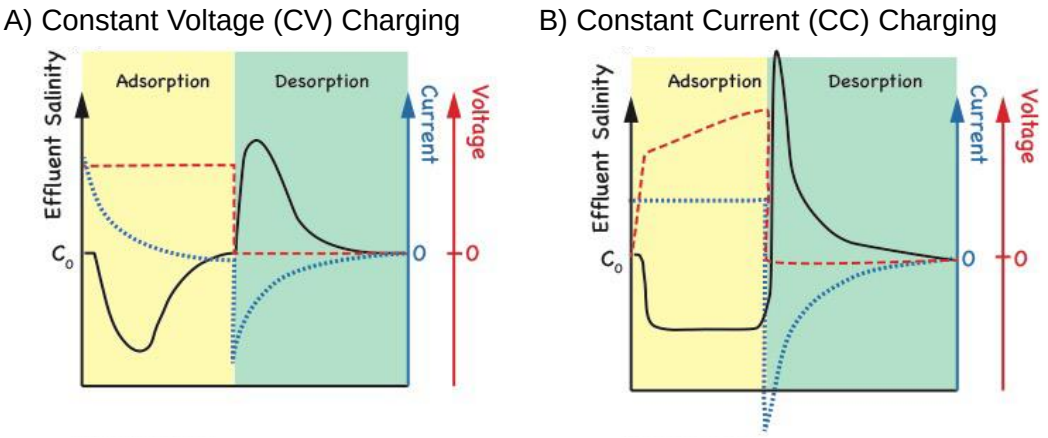

Figure 1.2 Illustration of constant voltage charging and constant current charging. (A) Constant voltage (CV) charging and zero voltage discharge, effluent concentration profile and current responses. (B) Constant current (CC) charging and zero voltage discharge, effluent concentration profile and cell voltage responses.

1.2.3. CDI cell architectures

In recent years, many efforts have been devoted to innovate new cell architectures for CDI. Cell architecture is important for CDI cell operation. The classic flow-by or flow-between cell is most commonly used in CDI studies. For the past decades, several novel cell architectures have been developed to introduce interesting features. We will discuss the recent developments of cell architectures in this section.

1.2.3.1. Flow-by cell

This is possibly the most common CDI cell architecture. Feed water flows in between two porous electrodes (Fig 1.1). This design is also the cell type we use for the work in this dissertation. The cell has to be operated alternatively from charging to discharge steps.

1.2.3.2. Flow-through cell

In this architecture, feed water flows through the inter-particle pores of electrodes. It is claimed that the distance for ion passage is shortened in this architecture.

1.2.3.3. Flow-electrode cell

Instead of static film electrode, carbon flow electrodes, or carbon slurry electrodes are pumped through the cell, and this is called flow-electrode CDI (FCDI). There are two benefits with FCDI. First, the cell is able to continuously desalinate feed water as the discharge of electrodes can be realized in a separate downstream cell. Another benefit of FCDI is that it can always take fresh uncharged carbon slurries so that the capacitance is improved above the conventional static film electrodes.

1.2.4. Performance metrics

Several metrics are introduced lately to evaluate the performance of CDI systems:

1) Salt adsorption capacity (SAC): the amount of salt adsorbed per mass or projected area of porous electrodes. This value depends on the cell voltage and feed salinity, along with the electrode properties. If the SAC is obtained when the cell is at equilibrium, it is termed eqSAC.
2) Average salt adsorption rate (ASAR): the amount of salt adsorbed divided by either the charging duration or the full cycle time. Without further explanation, this thesis adopts the latter definition.
3) Specific energy consumption (SEC): the energy consumed to reduce feed water salinity, either normalized by the amount of removed ions (SEC_i) or by the volume of desalinated water (SEC_w).
4) Water recovery (WR): the ratio of desalinated water volume over the total volume of water fed into the CDI system.
5) Thermodynamic energy efficiency (TEE): the ratio of the specific Gibbs free energy of separation (i.e. energy consumed in a thermodynamic reversible cycle) over the actual energy consumption (i.e. SEC).
6) Charge efficiency (Λ): the ratio of salt adsorbed over the electrons transferred to the capacitor. The value is subjected to the cell voltage and the electrolyte salinity. Also the properties of the electrode, such as resistance to side reactions and the capacitance affect the charge efficiency.

1.3. Overarching Goal of this Dissertation

As a highly popular research topic in the past few years, many efforts have been devoted to elucidate the ion transport theory,[10, 14, 15] develop new cell configurations,[16, 17] explore operation methods,[18] and fabricating high-performance electrode materials.[19, 20] Nevertheless, the energy efficiency of CDI systems are quite low, which is ascribed, to a large extent, by the significant entropy generation from the suboptimal operation strategies. Furthermore, the assertion that CDI is more energetically efficient than reverse osmosis (RO) for desalinating low-salinity brackish water, lacks a solid theoretical ground. As of now, we still lack of a valid and applicable approach to assess the energy efficiency of CDI processes and compare them with other desalination technologies. Therefore, to significantly advance CDI energetic performance and potentially promote its practical applications, we need to improve our fundamental understandings of CDI processes, followed by optimization and enhancement of CDI performance inspired by the understandings. The solutions discussed in this dissertation are comprised of the following components: (1) we develop a rational approach to accurately gauge the energy efficiency of CDI; (2) we demonstrate that the energy efficiency could not be divorced from the kinetic efficiency, and quantify their trade-off; (3) we evaluate the commonly charging schemes for CDI so as to optimize the processes; (4) we reduce the resistance of macropores of the carbon electrodes by infiltrate with ion-conductive polyelectrolytes, and demonstrate this modification could drastically enhance the energy efficiency; (5) we model the steady state of continuous operation FCDI in the purpose of expanding our understandings to a practical level.

1.4. Specific Objectives

The objectives of the research include: (1) develop a rational approach to accurately gauge the energy efficiency of CDI, and compare it with the state-of-art desalination processes; (2) quantify the intrinsic trade-off between energetic and kinetic efficiencies in CDI; (3) Optimize the operation conditions so as to lower the energy consumption producing fresh water.

First, to achieve the objectives, we construct a thermodynamic reversible process for CDI, so that we can pinpoint how far away it is in its current condition from the ideal scenario. The

thermodynamic reversible process could provide insights to analyze and optimize the energetic performance of CDI.

In addition, we develop a concept called thermodynamic energy efficiency by comparing the actual energy consumption with the Gibbs free energy of separation. This will allow us to assess the energy efficiencies of different desalination processes. A systematic assessment will be conducted by extracting data from published literatures on CDI and evaluate the corresponding thermodynamic energy efficiency.

Secondly, we demonstrate that the energy efficiency is strongly related to the kinetic efficiency. Quantification of such relationship is important for process evaluation, optimization and system design.

Thirdly, the dependence of energy efficiency on operational modes is yet resolved. We study the various operations of CDI process and find out which of them is more energetic efficient achieving the same separation. There are two common operation modes for charging CDI, that is applying either constant current (CC) or constant voltage (CC) across the cell. By comparing the voltage of each operation mode with the voltage of reversible process, we can explain the disparate performances of the two modes in energy efficiency.

Furthermore, with the understanding how the energy efficiency is affected and where the energy is dissipated, we will proceed to enhance the CDI performance. In this regard, we reduce the impedance of the electrode macropore in order to enhance the energy efficiency of the CDI.

Finally, yet importantly, the nature of intermittent operation limits CDI application, which leads to the rise of continuous operation of an alternative, flow-electrode CDI (FCDI). We develop a system-level for FCDI so as to investigate the performance and to shed light on the optimization.

1.5. Dissertation Structure

Following the above objectives and approaches, this dissertation is divided into eight chapters. In Chapter 2, we construct the thermodynamic reversible cycle for CDI, followed by a survey of literatures studying CDI in Chapter 3 where we analyze the data in respect to the energy efficiency, and identify the directions to improve the performance. In the following Chapter 4, we quantify the kinetic-energetic tradeoff curves in MCDI, and discuss the significance of the tradeoff

curves in performance analysis and practical system design. Then we evaluate the two common charging methods, i.e. constant current and constant voltage, by employing the tradeoff curve developed in the previous chapter. In Chapter 6, we discuss the importance of electrode macroporous resistance, and enhance the performance by infiltrating a conductive polyelectrolyte into the macropores. Lastly, in the purpose of scale up of CDI techniques, we model the steady-state operation of flow-electrode CDI with equivalent film-electrode CDI model in Chapter 7.

CHAPTER 2

THERMODYNAMIC ANALYSIS OF CAPACITIVE DEIONIZATION

This chapter has been published in Journal of Colloidal and Interface Science as part of the following peer-reviewed manuscript: Wang, L.; Biesheuvel, P.M.; Lin, S., Reversible thermodynamic cycle analysis for capacitive deionization with modified Donnan model. Journal of Colloidal and Interface Science, 512(2018). p. 522-528. doi:10.1016/j.jcis.2017.10.060.

2.1. Overview

Carbon electrode based capacitive deionization (CDI) utilizes the formation of electrical double layers (EDL) to temporarily store the charged ions in the micropores of the carbon electrodes. The capacity of temporary ion retention for a given mass of electrode is dependent on the cell voltage and will thus be eventually exhausted as more ions are stored in the electrodes[1, 8, 21]. Upon the saturation of carbon electrodes at a given cell voltage, one needs to recover the ion removal capacity by either short-circuiting the electrodes, or reducing the cell voltage, or even applying a reverse cell voltage, in which cases part or all of the temporarily stored ions are released back to the bulk solution.

To achieve an overall desalination separation, the system has to remove ions from the feed solution in the charging (or adsorption) stage, and to discharge these temporarily stored ions to the brine solution in the discharge (or desorption) stage, which is usually accomplished in two approaches in practical CDI operations. The first approach involves periodically feeding the CDI system with two streams from the same source water, one serving as the feed stream to be desalinated and the other as the brine stream to receive the discharged salts. Typical CDI configurations, such as flow-by and flow-through CDI[16, 22], belong to this approach. The second approach employs moving electrodes that are forced to be in alternating contact with the feed and brine streams for adsorption and desorption, respectively. CDI systems with flow electrodes[23, 24] or rotating-rod electrodes[17] belong to this approach. While systems adopting the first approach are

structurally simpler and thus more prevalent, the second approach offers the advantages of continuous operation and a greater potential to desalinate high salinity feed stream.

Regardless of the operational approach, a CDI process always achieves a separation that is defined by the water recovery and the salinities of the feed solution, dilute solution, and brine solution. Solution thermodynamics dictates that a minimum amount of energy has to be consumed to achieve a given separation or, in other words, to achieve the non-spontaneous reduction of the solution entropy[25]. The minimum energy of separation, or the Gibbs free energy of separation, is consumed if and only if the separation process is thermodynamically reversible, whereas all practical processes involving thermodynamic irreversibility consume more energy than such a thermodynamic minimum[26]. This has been shown in reverse osmosis (RO) in which thermodynamic reversibility can be attained by adjusting the applied pressure to be always equal to the brine osmotic pressure[27, 28]. Demonstrating the same phenomenon (i.e. a reversible process consumes the minimum energy of separation) is significantly more challenging for CDI, but has nonetheless been successfully carried out with the Gouy-Chapman-Stern (GCS) model in a previous study[29].

Conducting a reversible thermodynamic analysis on a CDI process requires the quantification of equilibrium ion retention by the electrodes under different cell voltages[29]. The EDL theory suggests the existence of a well-defined relationship between the surface charge density and the surface potential when the EDL is in thermodynamic equilibrium[30]. For a planar surface with a fully developed EDL, the GCS model can be applied to relate the surface potential to the areal surface charge density. In the GCS model, the EDL is decomposed into a charge-free Stern layer with a step potential drop and a diffuse layer the potential distribution of which is governed by the Poisson-Boltzmann (PB) equation[30, 31]. However, in realistic carbon electrodes used in CDI, micropores with a pore size of 2 nm and below are primarily responsible for ion retention[31, 32]. While the PB equation still applies within the framework of mean-field theory, the direct application of the GCS model in this case is challenging as EDLs cannot fully develop due to the geometric constraint, i.e., the EDLs significantly overlap in these micropores the dimension of which is comparable or even smaller than the Debye length[10]. This challenge of quantifying equilibrium ion retention in micropores has been overcome in recent CDI transport models by employing a modified Donnan (mD) model[33].

The previous study on a reversible CDI process analyzed a three-stage process comprising a charging stage, a solution switch stage, and a discharge stage[13]. It was shown that as cell voltage returns to zero, the areal surface charge density also returns zero. However, in an mD model with micropores, the micropore solute concentration is dependent on the bulk solute concentration and can thus assume different values at zero cell voltage. This implies that while the previously analyzed three-stage CDI process appeared to be a cycle based on the relationship between charge density and cell voltage, it was not actually cyclic if the micropore solute concentration is also considered. While a non-cyclic process can also be thermodynamic reversible, a cyclic analysis is preferred to better reflect the nature of practical CDI operations.

This study aims to analyze the energy consumption of a thermodynamically reversible cycle for a CDI process using carbon electrodes with micropores. Specifically, we quantify the energy consumption a four-stage CDI cycle using the modified Donnan (mD) model and compare that to the Gibbs free energy of the separation achieved by such a cyclic CDI process. We derive the equilibrium relationships between cell voltage, volumetric charge density in the micropores, solute concentration in the micropores, and bulk concentration, based on the mD model. These equilibrium relationships, along with solute mass balance, are applied to analyze the energy consumption of four-stage batch CDI cycles. Finally, we compare the energy consumptions of these reversible CDI cycles with the Gibbs free energy of the separations resulting from those cycles.

2.2. Specific Gibbs free energy of separation

Regardless of the mechanism involved, a CDI process always separates the saline water (i.e. the feed solution) to a dilute solution and a concentrated solution (i.e. the brine). In general, we can define a separation by specifying the feed concentration, c_0, the dilute solution concentration, c_D, the brine concentration, c_B, and the water recovery, γ, which is simply the volume of the dilute solution over that of the feed solution (i.e. $\gamma = v_D/v_0$).

Of these four parameters that define a generic separation, only three are independent based on solute mass balance specified by eqn 2.1:

$$c_0 = c_B(1-\gamma) + c_D\gamma \tag{2.1}$$

A generic separation defined by c_0, c_D, c_B, and γ always requires a minimum amount of energy to generate a unit volume of the dilute solution as determined by reversible thermodynamics. This thermodynamically minimum energy is often referred to as the *specific* Gibbs free energy of separation, Δg, which can be quantified by computing the entropy change of the system induced by the separation[34]:

$$\Delta g = nRT\left\{\frac{c_0}{\gamma}\ln\left[\frac{c_0-\gamma c_D}{c_0(1-\gamma)}\right]-c_D\ln\left[\frac{c_0-\gamma c_D}{c_D(1-\gamma)}\right]\right\} \quad (2.2)$$

Here, n is the van't Hoff factor, R is the ideal gas constant, and T is the absolute temperature. Throughout the following discussion, we will focus on ideal solutions of 1:1 strong electrolytes (i.e. fully dissociated), rendering n =2. However, eqn 2.2 applies to any ideal solutions of strong electrolytes with any van't Hoff factor. We note that Δg, unlike the total Gibbs free energy of separation, is independent of the scale of desalination, thanks to the normalization by the volume of the dilute solution.

2.3. Modified Donnan (mD) model for ion retention by porous carbon electrodes

The mD model provides a very good approximation to the solution of the PB equation for micropores with a characteristic dimension smaller than or comparable to the Debye length[35]. It assumes a uniform potential distribution throughout the diffuse layer within the micropores, i.e., there is a single electrical potential instead of a potential distribution within the micropores (but outside the Stern plane)[36]. Two potential drops are present in the mD model: the Stern potential, $\Delta\phi_S$, which is the potential drop across the Stern layer; and the Donnan potential, $\Delta\phi_D$, which is a step potential drop across the micropore-macropore interface. For convenience, the mD model also uses volumetric charge density within the micropores, σ_{mi}, instead of the areal surface charge density that is more relevant to fully developed EDLs at solid-water interfaces. Moreover, the Stern layer capacitance, C_S, is assumed to be dependent on σ_{mi} [17, 33]. The mD model has been adopted for modeling ion retention performance for CDI[10, 33, 36, 37]. When the cell voltage, V_{cell}, is equally distributed between the two half cells, the relationship between σ_{mi} and V_{cell} at a given bulk concentration, c_∞, can be derived following the mD model presented below.

At equilibrium, the concentration of ion species i in the micropores ($c_{i,mi}$) is related to the Donnan potential and the macropore ion concentration according to

$$c_{i,mi} = c_{i,mA} \exp(-z_i \cdot \Delta\phi_D) \tag{2.3}$$

where $c_{i,mA}$ is the macropore concentration of ion i, z_i is the ion charge number (+1 for cations and -1 for anions), and $\Delta\phi_D$ is the dimensionless Donnan potential which can be multiplied by the thermal voltage, V_t (i.e. 25.6 mV at room temperature) to obtain the actual Donnan potential with the unit Volt. Due to charge neutrality in macropores, $c_{i,mA}$ for the cation and anion equal each other and is also identical to the salt concentration (c_{mA}) for 1:1 electrolyte discussed. No differentiation is made between macropore and bulk in this analysis as equilibrium is maintained throughout the reversible thermodynamic process, i.e., the ion transport rate is infinitely slow such that no concentration gradient develops due to rate limited ion transport. Therefore, $c_{i,mA}$ is the same as the bulk concentration, c_∞.

For a 1:1 salt, the micropore volumetric charge density (σ_{mi}) is expressed as

$$\sigma_{mi} = \sum_i c_{i,mi} F = -2c_\infty \sinh(\Delta\phi_D) F \tag{2.4}$$

where F is the Faraday constant. The relationship between σ_{mi} and the dimensionless Stern layer potential, $\Delta\phi_S$, is given by

$$\sigma_{mi} = -C_{St,vol} \Delta\phi_S V_t \tag{2.5}$$

where $C_{St,vol}$ is the volumetric Stern layer capacitance. An empirical expression is often used to account for the increased Stern layer capacitance with increasing charge density due to electrostatic compression[38, 39].

$$C_{St,vol} = C_{St,vol,0} + \alpha(\sigma_{mi}/F)^2 \tag{2.6}$$

In equilibrium, the sum of $\Delta\phi_S$ and $\Delta\phi_D$ equals half of the potential across the cell ϕ_{cell} for symmetric cells

$$2(\Delta\phi_S + \Delta\phi_D) = V_{cell}/V_T \tag{2.7}$$

Here, potential drops due to resistances in the circuit, electrode, bulk solution and at the interfaces can be ignored because of the zero electrical current in a thermodynamically reversible process. Solving equations 2.3) to 2.7 yields the relationship between σ_{mi} and V_{cell} for a given c_{mA} (which is also c_∞ in equilibrium) when the system reaches thermodynamic equilibrium. Representative "σ_{mi} vs. V_{cell}" curves for c_∞ of 1, 10, and 100 mM are given in Figure 2.1. The

volumetric charge density, σ_{mi}, grows with increasing V_{cell}. At the same V_{cell}, σ_{mi} is higher with a higher bulk concentration, c_{∞}.

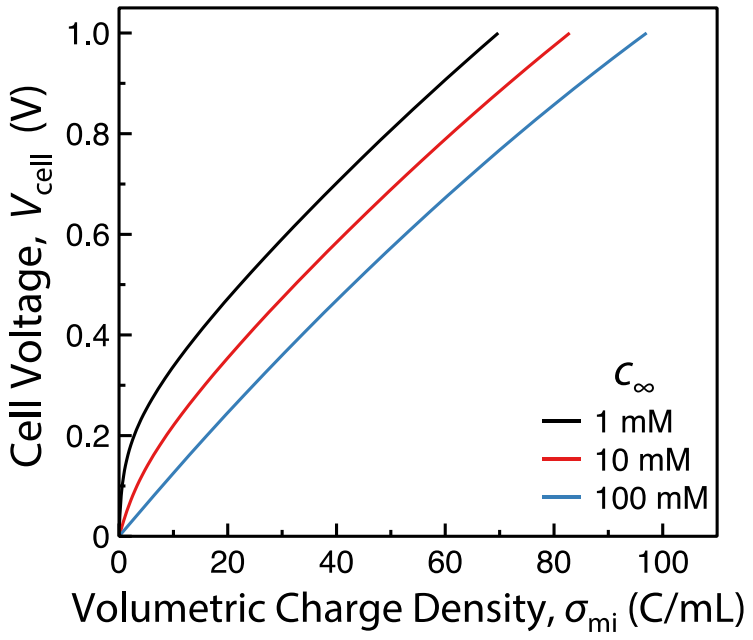

Figure 2.1 The quantitative relationship between cell voltage, V_{cell}, and the volumetric charge density in the micropores, σ_{mi}. The curves are modelled when an electrode is in equilibrium with a bulk solution with different bulk salinity, c_{∞}. These curves are generated using the mD model given by Eqns 2.3 to 2.7.

2.4. A four-stage reversible cycle for batch-mode capacitive deionization

The reversible thermodynamic cycle is composed of four stages: a charging stage, a discharge stage, and two stages responsible for switching the bulk solutions at the end of the charging and discharge stages. To facilitate discussion, we define four distinct states that are connected by, and demarcate, the four stages (Figure 2.2). In addition, ideal carbon electrodes without intrinsic surface charges are assumed in this analysis[37], in other words, $\sigma_{mi} = 0$ if and only if $V_{cell} = 0$. Analysis of reversible thermodynamic cycle involving electrodes with intrinsic

surface charge[37] or electrodes involving Faradaic reaction or ion intercalation[40, 41], which might be possible, is not considered in the current study. Here, we will describe, with the help of Figure 2.2, the thermodynamic cycle in a batch operation using the four stages and the four states. We note that all processes described in the following text occur in an infinitely slow manner to maintain thermodynamic equilibrium throughout the process.

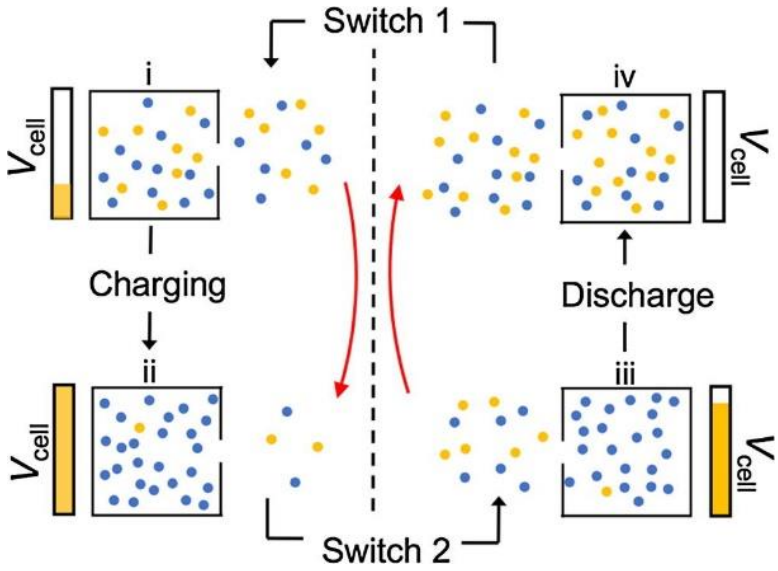

Figure 2.2 Graphical illustration of a batch-mode and thermodynamically reversible CDI process. The square box with a small opening represents the micropore potential of which differs from the bulk solution (i.e. outside the micropores) by $\Delta\phi_D$. The areas of the micropore and bulk solution on the figure do not scale with their actual volumes in real systems. The progression from state (i) to (ii) represents the adsorption (charging) stage, whereas the progression from state (iii) to (iv) represents the desorption (discharge) stage. In the "switch 1" stage, the brine in the bulk solution is replaced by the feed solution, while the micropore concentration remains constant. In the "switch 2" stage, the dilute bulk solution is replaced by the feed solution that will receive the ions to be released from micropores, whereas the micropore concentration also remains constant. In both switching stages, the micropore salt concentrations, c_{mi}, are maintained to be constant by adjusting cell voltage, V_{cell}.

State (i) represents the point when bulk solution switching is completed and the system is ready for a new cycle of ion adsorption. In state (i), the bulk concentration, c_∞, is the feed concentration, c_0. However, the micropore concentration, $c_{mi,(i)}$, is maintained at the same micropore concentration as that before solution-switch ("Switch 1" in Figure 2.2), i.e., based on our chosen assumption of fixed micropore concentration during solution-switch, $c_{mi,(i)}$ is equal to the c_{mi} in state (iv), $c_{mi,(iv)}$. The condition of constant c_{mi} can be achieved by varying V_{cell} to yield an $\Delta\phi_D$ that always equals $cosh^{-1}(c_{mi}/c_\infty)$ during the switch to maintain equilibrium.

The charging stage involves increasing V_{cell} to a predetermined maximum V_{cell} that defines state (ii). In state (ii), c_{mi} and σ_{mi} both reach maxima, whereas c_∞ attains minimum which is the concentration of the dilute solution, c_D. Once the charging stage is completed, the bulk solution at concentration c_D is switched to a new batch of bulk solution at concentration c_0. During this solution-switch ("Switch 2" in Figure 2.2), the dilute solution is extracted from the system whereas the micropore concentration is maintained constant by reducing V_{cell} to maintain equilibrium. At the end of this solution-switch stage, the system is in state (iii).

The discharge stage is carried out by reducing V_{cell} to release the ions from the micropores to the bulk solution. In most cases, the cell voltage is reduced to zero at the end of the discharge stage, bringing the system to state (iv). The zero V_{cell} in state (iv) results in zero $\Delta\phi_D$ and zero micropore charge density, i.e. $\sigma_{mi,(iv)} = 0$. Consequently, the system in state (iv) has the same concentration for both micropore and the bulk solution, both being the brine concentration, c_B. We note that although here we introduce a reversible cycle with the V_{cell} in state (iv) being zero, the final discharge voltage can also be positive, in which case less retained ions are discharged.

The last stage of the cycle switches the bulk solution from the brine resulting in state (iv) to the feed solution with a concentration c_0, which is necessary for the next cycle CDI operation to begin. Here, V_{cell} is again controlled during this stage to maintain a constant micropore concentration (i.e. $c_{mi,(iv)} = c_{mi,(i)}$). This last solution-switch stage completes a CDI cycle. The system at the end of this switching stage is in state (i), which is also the beginning state of the next cycle. The net effect of a complete cycle elaborated above is the reduction of the salinity of a batch of feed solution from c_0 to c_D, and increasing the salinity of another batch of feed solution from c_0 to c_B (red arrows in Figure 2.2), which is a separation completely defined by c_0, γ, c_B, and c_D. Certainly, energy has to be supplied to the system in order to run through this complete cycle.

To numerically construct the V_{cell}—σ_{mi} curve for a thermodynamic reversible CDI cycle describe above, we apply the mass balance equation about the solute as given by eqn 2.8:

$$(c_{mi}^0 - c_{mi})v_{mi} = (c_\infty - c_\infty^0)v_{bulk} \quad (2.8)$$

where c_{mi}^0 and c_∞^0 are the initial micropore and bulk concentrations respectively; c_{mi} and c_∞ are the micropore and bulk concentrations at any given time during the charging and discharge stages, which change as the charging/discharge occurs; v_{mi} is the total electrode micropore volume, and v_{bulk} is the bulk solution volume. It is worth noting that both initial concentrations refer to the state before either charging or discharge stage, which are also the concentrations at the end of either solution-switching stages. In the switching stages, c_{mi} remains constant while c_∞ decreases or increases to c_0 in 'Switch 1' or 'Switch 2', respectively. The cell voltage is continuously adjusted to maintain an equilibrium between micropore and macropore.

Eqns 2.3 to 2.8, which are essentially based on equilibrium condition and solute mass balance, are solved numerically to construct a full cycle consisting of charging, discharge, and two solution-switch stages. A reversible cycle can be presented using two separate figures, one showing the relationship between V_{cell} and σ_{mi} and the other showing the relationship between c_{mi} and c_∞. In this study, the final charging voltage is chosen to be 1V, whereas zero and non-zero voltage discharge are both investigated.

2.5. Reversible CDI cycles consume Gibbs free energy of separation

Figure 2.3 shows the "V_{cell} vs. σ_{mi}" and "c_{mi} vs. c_∞" curves for two representative separations. The first separation (Figure 2.3A and 2.3B) reduces the salinity of 90% of the feed solution from 20 mM to 0.5 mM, converting 10% of the feed water into a brine with a salinity of 195.5 mM. The specific Gibbs free energy of separation, Δg, calculated using eqn (2), is 0.066 kWh m^{-3}. The second separation (Figure 2.3C and 2.3D) recovers 50% of feed solution to become a dilute solution of 1 mM, turning the other 50% of the feed water to be a brine solution of 39 mM, which requires a Δg of 0.032 kWh m^{-3}.

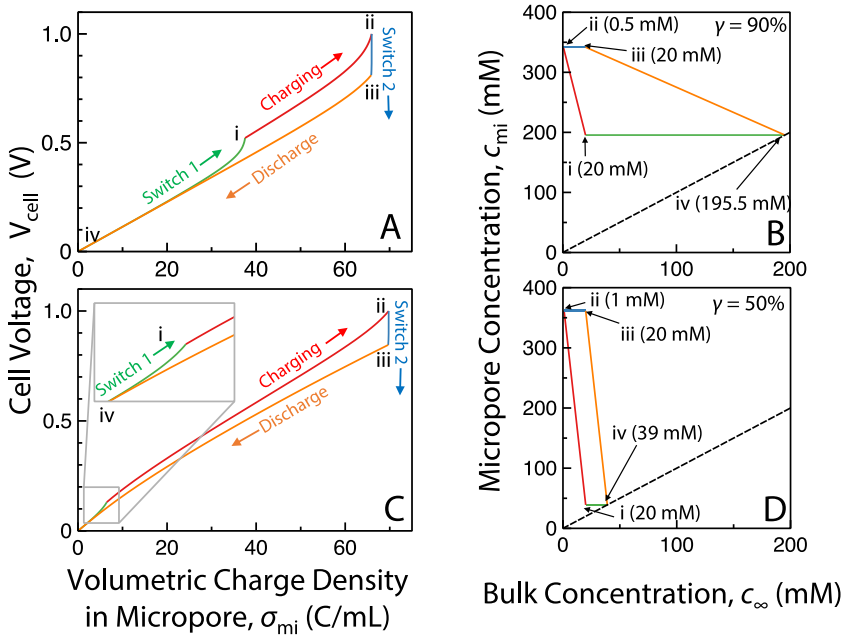

Figure 2.3 Relationship between cell voltage and micropore charge density, and that between the micropore and bulk concentrations. (A) and (C) the relationship between volumetric charge density in the micropores, σ_{mi}, and the cell voltage, V_{cell}, in thermodynamically reversible CDI cycles. (B) and (D) the relationship between micropore concentration, c_{mi}, and the bulk concentration, c_∞, in the corresponding reversible CDI cycles. The dashed lines in (B) and (D) represent cases where c_{mi} is equal to c_∞. The separation described by (A) and (B) is defined as c_0=20 mM, c_D=0.5 mM, c_B=195.5 mM and γ=90%. The separation described by (C) and (D) is defined as c_0=20 mM, c_D=1 mM, c_B=39 mM and γ=50%. The four states (i, ii, iii, and iv) and the four stages (featured by different colors) are shown in the figures. Each point on the cycles is derived using the mD model to establish the relation between σ_{mi} and V_{cell} at a given c_∞. However, unlike Fig. S1, each point on the cycles corresponds to a different bulk salinity, c_∞, to account for the change of the bulk solution during the charging/discharging and switch stages. SEC of a reversible CDI cycle is proportional to the area outlined by the respective cycles (A) and (C).

The total electrical work required to run such thermodynamic reversible CDI cycles, W_R, can be determined by subtracting the electrical work done by the system during the discharge stage (W_d) and the second switching stage (W_{s2}) from the electrical work done to system during the first switching stage (W_{s1}) and the charging stage (W_c), i.e., $W_R = W_{s1} + W_c - W_{s2} - W_d$. This

can be quantified by multiplying the total micropore volumes, v_{mi}, with the area of the "cycles" in Figure 2.2A and 2.2C, which represent the electrical work done to the system per micropore volume. Specific energy consumption (*SEC*) of such a reversible CDI cycle, SEC_R, is defined as the energy consumed per volume of dilute solution:

$$SEC_R = \frac{W_R}{v_D} = \frac{v_{mi}}{v_D} \oint V_{cell}(\sigma_{mi}) d\sigma_{mi} \tag{2.9}$$

We note that no system-specific parameter is needed when quantifying SEC_R using eqn 2.9 except the two parameters used in the empirical expression for the volumetric Stern layer capacitance, $C_{St,vol}$. The values of these parameters ($C_{St,vol,0}$ and α in eqn 2.6), which are determined mostly by the physics of the Stern layer rather than the properties of the materials and are thus relatively universal, are chosen according to what have been reported in literature[33, 42].

Numerical integrations were carried out to find SEC_R, based on eqn 2.9, for both separations presented in Figure 2.3. SEC_R for the first separation (Figure 2.3A and 2.3B) and the second separation (Figure 2.3C and 2.3D) are found to be 0.066 and 0.032 kWh m^{-3}, respectively. These SEC_R, calculated using eqn 2.9, are almost exactly the same as Δg for the respective separations calculated using eqn 2.2, with less than 0.3% numerical deviation. This exceptional numerical consistence between SEC_R and Δg demonstrates that a thermodynamically reversible CDI processes consume Gibbs free energy of separation.

The thermodynamic cycle analysis can also be conducted on a CDI process in which the final voltage of the discharge stage is positive. Such an incomplete discharge is relevant as it has been shown that increased discharge voltage can enhance charge efficiency and reduce energy consumption in practical operations[43]. Fig. 4 shows a CDI cycle with a final discharge voltage of 0.7 V (solid cycle) as compared to a reference cycle with a final discharge voltage of 0 (dotted cycle).

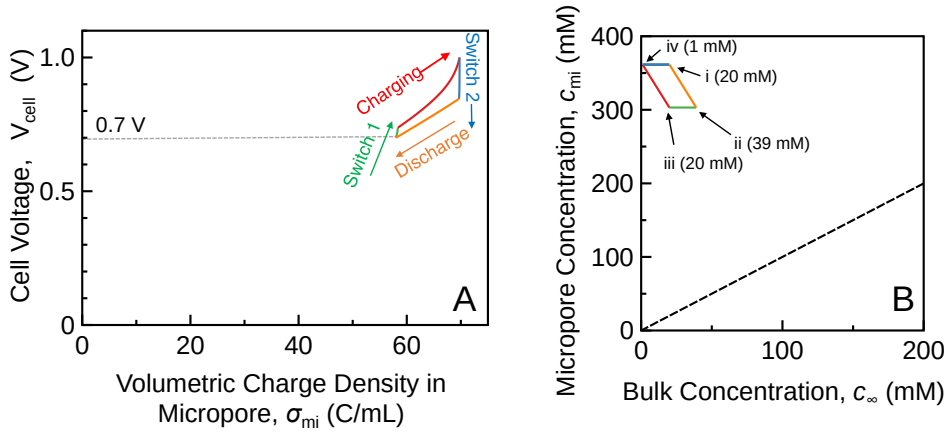

Figure 2.4 The relationships (A) between σ_{mi} and V_{cell}, and (B) c_{mi} and c_∞, in a thermodynamically reversible CDI cycle. The separation is defined as c_0=20 mM, c_D=1 mM, c_B=39 mM and γ=50%. The final voltage of the discharge stage is 0.7 V as shown in Figure 4A. The reference cycle presented using dotted lines/curves is the same as that in Fig. 3, which achieves the same separation but with a final discharge voltage of 0V.

Because the difference between the initial and final σ_{mi} for the charging stage in this case is significantly lower than that in a CDI cycle with a final discharge voltage of 0V, the CDI cycle in Fig. 4 requires a significantly larger micropore volume (equivalent to more electrode mass) per volume of dilute solution to achieve the same separation attained using a CDI cycle fully discharged to zero voltage. Therefore, even though the integrals $\oint V_{cell}(\sigma_{mi})d\sigma_{mi}$ is significantly smaller for a CDI cycle with a final discharge voltage of 0.7 V, as shown in Figure 2.4A, than that for CDI cycle with a final discharge voltage of 0, the SEC_R in these two CDI processes turn out to be exactly the same after accounting for the different v_{mi}.

The exceptional numerical consistence between SEC_R and Δg is not limited to the three specific scenarios discussed above. We have tested several other CDI cycles with different resulting separations and the numerical consistence between SEC_R and Δg is observed in all cases (Figure 2.5). So far, we have yet to observe any negative example in which such a numerical consistence does not apply.

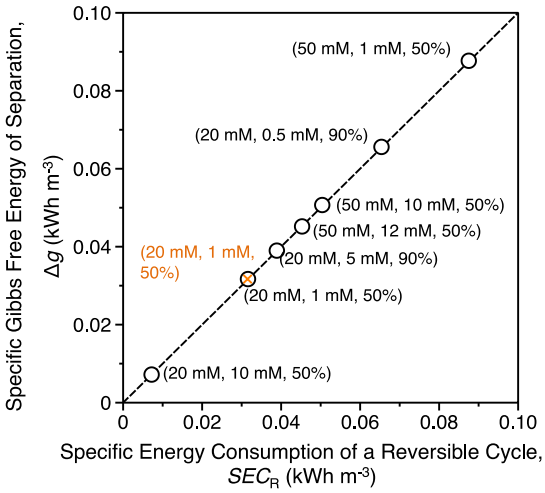

Figure 2.5 Specific Gibbs free energy of separation vs. specific energy consumption of a reversible CDI cycle for different separations. Each separation is defined by c_0, c_D, and γ that are given in the parentheses. All but the organe "x" are results from CDI cycles with a zero final discharge voltage. The organe "x" results from a CDI cycle with a final discharge voltage of 0.7 V. In all cases, the final voltage of the charging stage is 1 V. The dashed line represents the scenarios in which Δg is exactly equal to SEC_R. The linear regression of the data yileds a correlation (not shown in figure) of Δg=1.0024 SEC_R+0.00002, with an R^2 of 0.99998.

Admittedly, we cannot derive an analytical expression of SEC_R for a thermodynamically reversible CDI cycle and compare that to the analytical expression of Δg, as what has been done for RO[28, 44, 45] and pressure retarded osmosis (PRO) [46]. Nor can we exhaustively verify the numerical consistence between SEC_R and Δg for all possible separations. However, results from the mD model seem to provide confident support toward the widely-accepted principle that a separation process, if operated thermodynamically reversibly, consumes the Gibbs free energy of separation.

2.6. Conclusions

Analysis of thermodynamically reversible, four-stage batch CDI cycles using the mD model suggests that the electrical work consumed in such those reversible cycles are identical to the Gibbs free energy of the separations resulting from those cycles. Such an equality between SEC_R and Δg holds for all investigated scenarios with different feed salinity, dilute solution salinity, water recovery, and final discharge voltage. On the one hand, this equality is anticipated according to the widely recognized thermodynamic principle that a reversible separation process consumes the Gibbs free energy of separation. For example, such an equality has been demonstrated analytically in RO and PRO. It would be surprising if our analysis suggested otherwise.

On the other hand, it is rather impressive that numerical analyses based on the mD model in this study, and the GCS model in a previous study, both yield results that abide by this theoretically predicted equality to an exceptional precision. After all, both models only provide mean-field approximations of the realistic ion distribution in an EDL, and are based on empirical estimation of the Stern capacitance. While it is mechanistically very clear about how we arrived in such an equality for separating ideal solutions by RO, the fact that we can demonstrate this expected equality using numerical models with empirical parameters is both surprising and theoretically reassuring. Finally, the analysis of a thermodynamically reversible RO process has provided important insights to reduction of energy consumption in RO practice via innovative operation such as multi-stage and closed-circuit RO. We expect the elucidation of the thermodynamically reversible CDI cycle may also serve the theoretical foundation for us to better understand sources of inefficiency in practical CDI processes, and to develop novel operations or justify existing operations with higher thermodynamic reversibility and thus high energy efficiency.

CHAPTER 3

ENERGY EFFICIENCY OF CAPACITIVE DEIONIZATION

This chapter has been published in the journal *Environmental Science & Technology* as part of the following peer-reviewed manuscript: Wang L., Lin S., Energy efficiency of capacitive deionization. Environmental Science & Technology. **53** (2019). p. 3366-3378. doi:10.1021/acs.est.8b04858.

3.1. Overview

Capacitive deionization (CDI), though it has been invented almost 60 years ago, has started to make significant advances only in the last decade.[47, 48] Extensive effort has been devoted to developing high performance electrodes for CDI,[33, 49-58] designing novel cell configurations and operating schemes,[11, 16, 23, 59-66] elucidating fundamental mechanisms of ion adsorption and system behavior,[35, 37, 43, 67-70] and building numerical models that can predict process performance and be used in design optimization.[10, 15, 71-73] A major reason why CDI attracts intensive research interest is the belief that it is an energy efficient desalination technology with a strong potential to compete with the state-of-the-art desalination technologies, such as reverse osmosis (RO), at least for certain applications.[8, 9] Indeed, most CDI processes consume less absolute energy to generate a unit volume of product water. However, it is important to realize that the separations achieved by CDI are quite different from those achieved by conventional desalination technologies in terms of the feed salinity and the degree of salinity reduction. Similarly, the separations achieved in different CDI studies are also very different, which poses significant challenges for fair comparison of energy efficiency between different CDI processes.[74, 75]

The primary goals of this paper are to survey the literature for assessing the state-of-the-art energy efficiency of CDI and to analyze key factors that influence energy efficiency. In this review, we first describe a framework to ~~of~~ assess the energy efficiency of CDI based on comparing the energy consumption of a CDI process with the theoretical minimum energy of the separation achieved by that CDI process. We apply this framework to assess the energy efficiency

of CDI processes reported in literature, analyze possible sources of energy losses, and discuss factors that are strongly related to energy efficiency. In addition, we discuss possible reasons that lead to the very high energy efficiency in certain CDI processes with electrodes based on intercalation materials, and provide an empirical correlation using literature data to elucidate the dependence of energy efficiency on several key parameters. The focus of this paper is the energy efficiency of CDI. Other performance metrics are discussed only if they have strong relevance to energy efficiency. For more comprehensive and systematic discussions on various performance metrics and how CDI processes should be holistically evaluated, the readers are referred to several review papers including that by Porada et.al.,[1] Suss et. al.,[76] and more recently, Hawks et.al.[77]

3.2. Themordynamics of separation: benchmarking energy consumption

As one of the primary considerations in desalination technologies, energy consumption has been widely reported in CDI studies. In all cases, energy consumption is normalized in certain ways as *specific energy consumption* (*SEC*) that is independent of the system scale.[27] In desalination processes based on salt-rejecting mechanisms, such as RO and thermal distillation, the salinity of the product water is practically zero.[78, 79] *SEC* for these processes is usually defined as energy consumed per volume of product water generated (example unit: J/L or kWh/m^3). However, the more prevalently used *SEC* in scientific literature of CDI is defined as energy consumed to remove a certain amount of salts (example units: J/mg, J/mmole, or k_BT/ion),[9, 11] mainly because CDI operates based on a salt adsorption mechanism and there is a wide spectrum of product water salinity from different studies. Regardless of its definition, *SEC* as an absolute measure of energy consumption cannot be employed to quantify how efficiently energy is spent for achieving a given separation, because some separations are more "difficult" to achieve, and thus intrinsically require more energy, than others. Such "difficulty" of separation can be quantified by the specific Gibbs free energy of separation.[75, 80]

A generic separation can be defined by the feed concentration, c_0, the deionized water (i.e. the product water) concentration, c_D, the brine concentration, c_B, and water recovery, γ, defined as the volumetric fraction of the feed water that is recovered as the deionized water. Three of these parameters are independent according to solute mass balance given by $c_0 = c_B(1-\gamma) + c_D\gamma$.

Graphically, any separation can be visualized using a simple "separation line" (Figure 1A) that contains all the necessary information for defining a separation (see Supporting Information for interpretation of the separation line). An interesting and useful observation is that γ can be directly evaluated from Figure 1A as the ratio between $c_B - c_0$ and $c_B - c_D$. Intuitive comparison between two separations can be performed simply by juxtaposing two separation lines to each other.

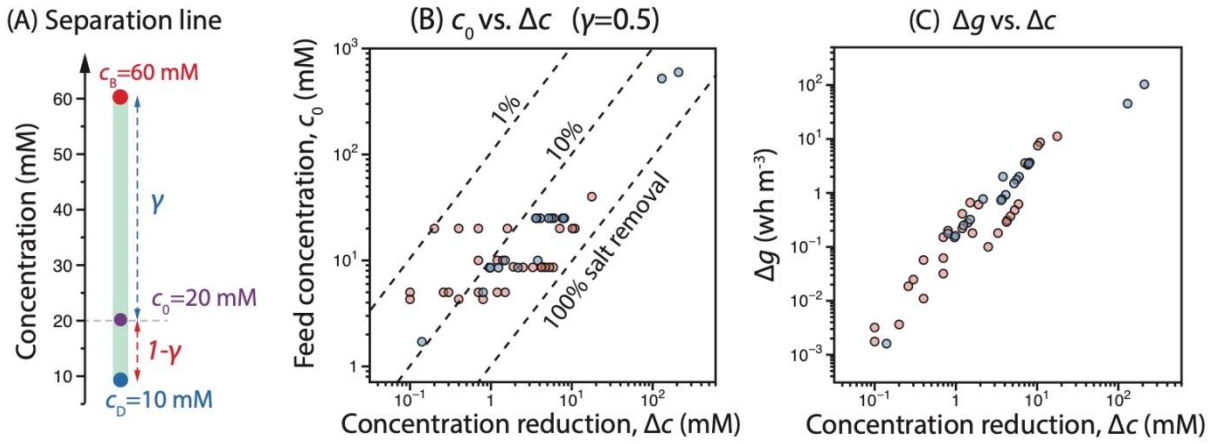

Figure 3.1 (A) A representative "separation line" that comprises c_0, c_B, and c_D. (B) Summary of the separations using c_0 vs. Δc for separations with $\gamma = 50\%$. (C) Δg vs. Δc for separations presented in panel B. Water recovery, γ, can be directly determined as the ratio between $c_B - c_0$ and $c_B - c_D$ in panel A. The dash line represents percentage salinity reduction (e.g. 1%, 10% and 100%) in panel B. For both panels B and C, red and blue circles represent data points from CDI with carbon electrodes and with electrodes based on intercalation materials, respectively. These data are from Table A1 which will be further analyzed in detail in Figure 3.2 for energy efficiency.

For the majority of CDI processes reported in literature, γ is 50%. The separation lines, in this case, are all composed of two equal halves each representing Δc ($= c_0 - c_D = c_B - c_0$). In this case, the representation of separation can further be simplified using a single point on a diagram with c_0 being the y-axis and $\triangle\, c$ being the x-axis (Figure 1B, data from Table S1). Figure 1B suggests that separations achieved in CDI processes reported in literature were dramatically different, with c_0 and Δc both spanning roughly three orders of magnitude. In general, Δc scales with c_0, which is necessary to observe any significant percentage reduction of salinity. However,

with a given c_0, Δc can span nearly two orders of magnitudes, which suggests that some CDI processes remove a large fraction of salt from the feed whereas some barely remove any. The CDI processes achieving the highest Δc were based on electrodes made of intercalation materials.[41, 81]

Thermodynamics of solution suggests that a generic separation defined by c_0, c_D, c_B, and γ always requires a minimum amount of energy to generate a unit volume of product water of concentration c_D .[25] This minimum *SEC*, achievable if and only if the separation is thermodynamically reversible, is the *specific* Gibbs free energy of separation, Δg,[29, 82] which can be obtained by computing the entropy change of the system resulting from the separation:

$$\Delta g = 2RT\left\{\frac{c_0}{\gamma}\ln\left[\frac{c_0-\gamma c_D}{c_0(1-\gamma)}\right]-c_D\ln\left[\frac{c_0-\gamma c_D}{c_D(1-\gamma)}\right]\right\} \quad (3.1)$$

Equation 3.1 is valid for fully dissociated 1:1 electrolyte solutions. Here, R is the ideal gas constant, and T is the absolute temperature. Like *SEC*, Δg is also normalized by the volume of the product water and is thus independent of the scale of separation. Theoretically, equation 3.1 is only applicable for ideal solutions. However, the thermodynamic principle that a separation always requires a minimum *SEC* holds also for non-ideal solutions. Numerical studies using the Gouy-Chapman-Stern model[29] and the modified Donnan model[82] demonstrate that thermodynamically reversible CDI processes indeed consume Δg. Very recently, Hemmatifar et.al. provided an elegant analytical proof that the work consumed by a thermodynamically reversible electrosoprtion process is exactly equal to Δg and that such an equality does not depend on the specific numerical model adopted in describing the EDL as long as parasitic reactions are not considered.[75] Therefore, specific Gibbs free energy sets the baseline for energy consumption of a CDI process. No CDI process, or any desalination process, can consume less *SEC* than Δg. For the data set we analyze, the calculated Δg roughly scale with Δc in a log-log plot (Figure 3.1C). However, for a given Δc, Δg can vary by more than an order of magnitude depending on other parameters such as feed salinity, which is consistent with equation 1 that shows Δg is a simple function of Δc.

3.3. Thermodynamic energy efficiency

As Δg quantifies the "difficulty" of the separation a CDI process achieves, it also serves as a reference to evaluate the relative energy efficiency of a CDI process. Such a relative energy

efficiency is the thermodynamic energy efficiency (*TEE*), which may allow the direct comparison between CDI processes resulting in different separations. Specifically, TEE is defined as the ratio between Δg of a separation and SEC of a CDI process resulting in that separation:

$$TEE = \Delta g / SEC \tag{3.2}$$

TEE represents the fraction of energy spent by a real CDI process that would have been spent by an ideal thermodynamically reversible process achieving the same separation, and can thus quantify the efficiency of energy utilization in a CDI process. By definition, TEE ranges from zero to unity. A low TEE indicates that only a small fraction of the consumed energy is utilized for separation and a large fraction is dissipated as heat. This concept of TEE was employed for systematic performance evaluation by Długołęcki and van der Wal[74] and has been recently revisited systematically by Hemmatifar et.al.[75] Here, we use the same approach to analyze a large group of experimental data from CDI studies in literature by first quantifying Δg and SEC, and then calculating TEE for these reported CDI processes using equation 3.2. The *SEC* and *TEE* are summarized in Figure 3.2 (details are reported in Table A1 and A2 in the Appendix). In most cases, c_0 and γ are directly reported, whereas c_D is the average effluent concentration in the charging step obtained following equation 3.3:

$$c_D = \frac{1}{\Delta t_{\mathrm{c}}} \int_{t_{\mathrm{c,0}}}^{t_{\mathrm{c,f}}} c_D(t) dt \tag{3.3}$$

where $c_D(t)$ is the effluent concentration at time t during the charging step, $t_{\mathrm{c,0}}$ and $t_{\mathrm{c,f}}$ are the initial and final time points of the charging step (i.e. $\Delta t_{\mathrm{c}} = t_{\mathrm{c,f}} - t_{\mathrm{c,0}}$ is the time of charging step). Values for c_0, c_D, and γ, Δg can be calculated from equation 3.1.

SEC of different CDI processes can be calculated using the following equation if all energy released in the discharge step is recovered:

$$SEC = \frac{1}{v_D} \int_{t_{\mathrm{c,0}}}^{t_{\mathrm{d,f}}} V_{cell}(t) i(t) dt \tag{3.4}$$

where $V_{cell}(t)$ and $i(t)$ are cell voltage and current at time t, and where $t_{\mathrm{d,f}}$ is the final time point of the discharge step (i.e. $t_{\mathrm{d,f}} - t_{\mathrm{c,0}}$ is the full cycle time), and v_D is the volume of the dilute water, which we calculate using $v_D = \phi_D \Delta t_{\mathrm{c}}$ with ϕ_D being the volumetric flow rate of the feed stream in the charging step. Alternatively, one can use $v_D = \phi_D \Delta t_{\mathrm{ads}}$, with Δt_{ads} being the period when the effluent concentration is lower than the feed water concentration, which is for short

desalination cycles often different from Δt_c. When $V_{cell}(t)i(t)$ is negative, the direction of the current is opposite to that of the cell voltage, and therefore recovery of energy can be achieved by charging the external capacitor or battery. If, however, no energy is recovered during the discharge step, SEC is defined as

$$SEC = \frac{1}{v_D}\int_{t_{c,0}}^{t_{c,f}} V_{cell}(t)i(t)\delta_{V,i}dt \tag{3.5}$$

where $\delta_{V,i}$ is a function that yields 1 when $V_{cell}(t)$ and $i(t)$ are of the same direction and 0 when $V_{cell}(t)$ and $i(t)$ are of different directions. In practice, for CDI processes with energy recovery, the efficiency of energy recovery is always less than 100% of the recoverable energy,[83] and consequently, SEC falls between the values calculated using equations 3.4 and 3.5. Alternatively, SEC is defined based on the amount of salt removed, and therefore the energy consumption is divided by the molar amount, or mass, of salt removed, instead of by v_D. In this section, we report SEC based on the definition of equation 3.4 (i.e. normalized by v_D) to be consistent with the reporting method adopted by most other desalination technologies.

To calculate Δg and SEC for CDI studies reported in literature, the necessary raw data include the time series of $c_D(t)$, $V_{cell}(t)$, $i(t)$, and values for ϕ_D, Δt_c, and the discharge time, Δt_d. We extracted data from a large number of CDI publications[2, 9, 11, 13, 19, 22, 33, 41, 43, 58, 59, 65, 74, 75, 81, 83-96] and analyzed the digitized data to obtain Δg and SEC using equations 3.1, 3.3, 3.4, and 3.5. For CDI experiments with non-zero voltage discharge (e.g. reverse current discharge), we calculate SEC using both equations 3.4 and 3.5 and use those results as the two boundaries of possible SEC which represent zero and full energy recovery, respectively. We note that full energy recovery does not mean recovering 100% of the energy spent in the charging step, but rather recovering 100% of the energy released during the discharge step, in which case SEC will be calculated by equation 3.4. These two boundaries define the top and the bottom of the bars in Figures 3.2A and 3.2B representing the possible range of SEC and TEE. A detailed example regarding the quantification of TEE from experimental results is given in the Supporting Information. We note that only papers reporting all necessary information required to calculate SEC and Δg were included in the analysis. Therefore, only a fraction of data from the CDI literature (see Table A1) is presented.

Figures 3.2A and 3.2B summarize the energy efficiency of CDI as *SEC* vs. Δg and *TEE* vs. Δg, respectively. Comparing these data to the reference lines representing thermodynamically

reversible processes, it is clear that most CDI processes reported in literature were thermodynamically highly irreversible. For CDI with carbon electrodes (i.e. not intercalation materials), *SEC* of desalination is typically one to three orders of magnitude higher than Δg of the resulting separation. The highest values of *TEE* seem to be achieved mostly using CDI with intercalation materials,[41, 81, 90, 91] for which we will provide possible explanations in the following sections. The data summarized here follow a similar trend as the data systematically collected in a recent study performed by Hemmatifar et.al (pink "ovals" denoted as "bg" in Figure 3.2, with details presented in respective insets).[75] In general, CDI processes have a higher *TEE* when they are operated to achieve a more "difficult" separation characterized by a higher Δg (Figure 3.2B).

The summarized data in Figure 3.2 show that, though the absolute energy consumption in terms of *SEC* is indeed quite low for most CDI processes (most considerably below 1 kWh m^{-3}), the relative energy efficiency of CDI in terms of *TEE* is quite low due to the very low Δg typical of separations achieved by CDI. Most CDI processes based on carbon electrodes did not achieve a *TEE* above 10%. Nevertheless, *TEE* above 10% was achieved in four recent CDI studies using intercalation materials as electrodes,[41, 81, 90] with the highest reaching 40%,[91] which is in the same order of magnitude as RO, the state-of-the-art desalination technology (a summary of *TEE* for RO applied to both seawater and brackish water desalination is listed in Table A3, and a more detailed theoretical comparison of energy consumption between CDI and RO is given by reference [97]).

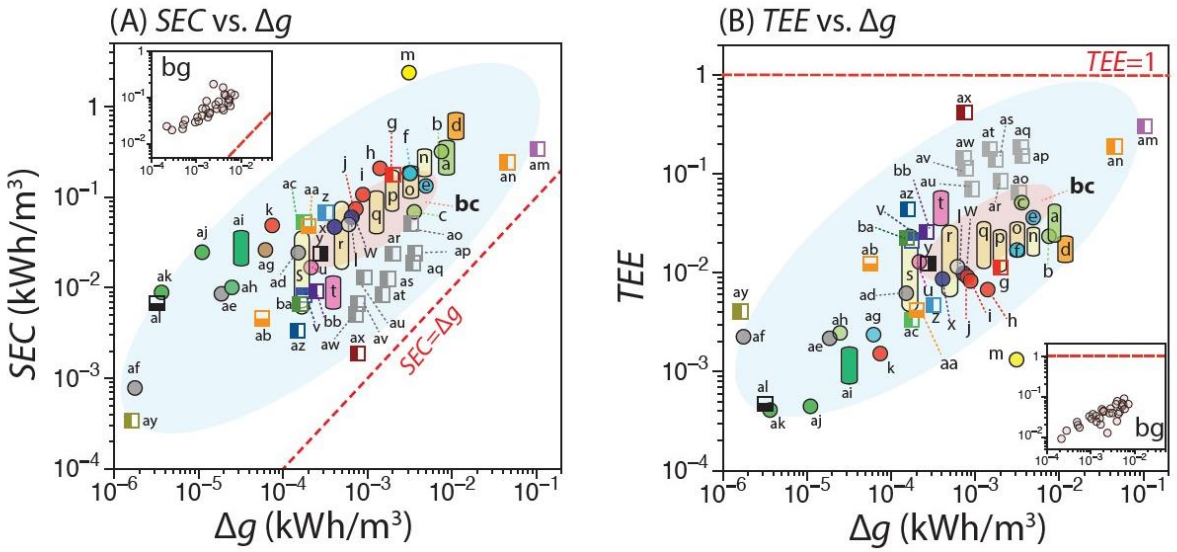

Figure 3.2 (A) SEC as a function of Δg. (B) TEE as a function of Δg. The red dash lines are the reference lines representing a thermodynamically reversible processes with $SEC = \Delta g$ and $TEE = 1$. Each data point in (A) and (B) is assigned a letter code that is referred to in Table S1 in Supporting Information. Different types of symbols represent different types of CDI processes: specifically, the circles are CDI with constant voltage (CV) charging and zero voltge (ZV) discharge; bars represent of CDI with constant current (CC) charging and reverse current (RC) discharge; solid-left represent CDI with intercalation materials; squares with solid-bottom represent inverted CDI; squares with solid-top ("v" and "bb") represent CDI with CV charging but non ZV discharge. For CDI with CC-RC operation, the bars represent the possible range of *SEC* and *TEE* for MCDI or CDI with controlled RC discharge, depending on the extent (0 to 100%) of energy recovery. Zero energy recovery corresponds to the top of the bars in panel A and bottom of the bars in panel B, while full energy recovery corresponds to the bottom of the bars in panel A and top of the bars in panel B. The "pink ovals" denoted as "bg" in both panels represent the range of data reported in the study of Hemmatifar et.al [40], with detailed data plotted in the insets. The axes for the insets are the same as those for the main figure.

3.4. Sources of energy losses in CDI and why TEE can be very low?

How can one explain the generally very low values for *TEE* reported for CDI? The first important reason is that most data in Figure 3.2 were acquired in CDI experiments using zero voltage (ZV) discharge with which no energy is recovered. With carbon electrodes, a large fraction of the energy spent in the charging step is stored in the electrical double layers (EDLs). Recovering this energy stored in the EDLs during the discharge step can enhance *TEE*.[74, 98] When the energy stored in EDLs is completely recovered, the values of *TEE* can be increased from the bottom to the top of the bars plotted in Figure 3.2B. We note that neither the energy consumed in the charging step nor the energy stored in the EDLs can be fully recovered. The theoretically recoverable energy is the energy consumed in the charging step minus the resistive energy losses in both the charging and discharge steps. In practice, a significant fraction of this theoretically recoverable energy can be recovered by a buck-boost converter in the discharge step.[83, 99]

Using flow-by CDI and MCDI (i.e. CDI with ion exchange membranes) processes with constant current charging and reverse current discharge (i.e. CC-RC operation) as examples, we illustrate the different contributions to the energy loss in Figure 3.3. We assume a current density of 30 A/m^2 and the absence of Faradaic energy loss in our numerical simulation using a one-dimensional dynamic steady-state model. The separation achieved is characterized by c_0=20 mM (1:1 electrolyte), c_D=12 mM, and γ = 50% (thus c_B=28 mM). Different voltages and potential drops are plotted in Figures 3.3A (for CDI) and 3.3B (for MCDI) as function of electrode charge density, σ, which quantifies to what extent the CDI cell has been charged or discharged. In Figure 3.3A and 3.3B, the dashed curves represent the potential drop over the EDL (Stern and Donnan). The thickness of color-coded region represents the potential drop due to one of several resistances (to be elaborated) or the difference of the Donnan potentials at both ion exchange membrane (IEM) interfaces. The models used to generate all panels in Figure 3.3 have been reported in detailed in literature[72] and are summarized in the Supporting Information.

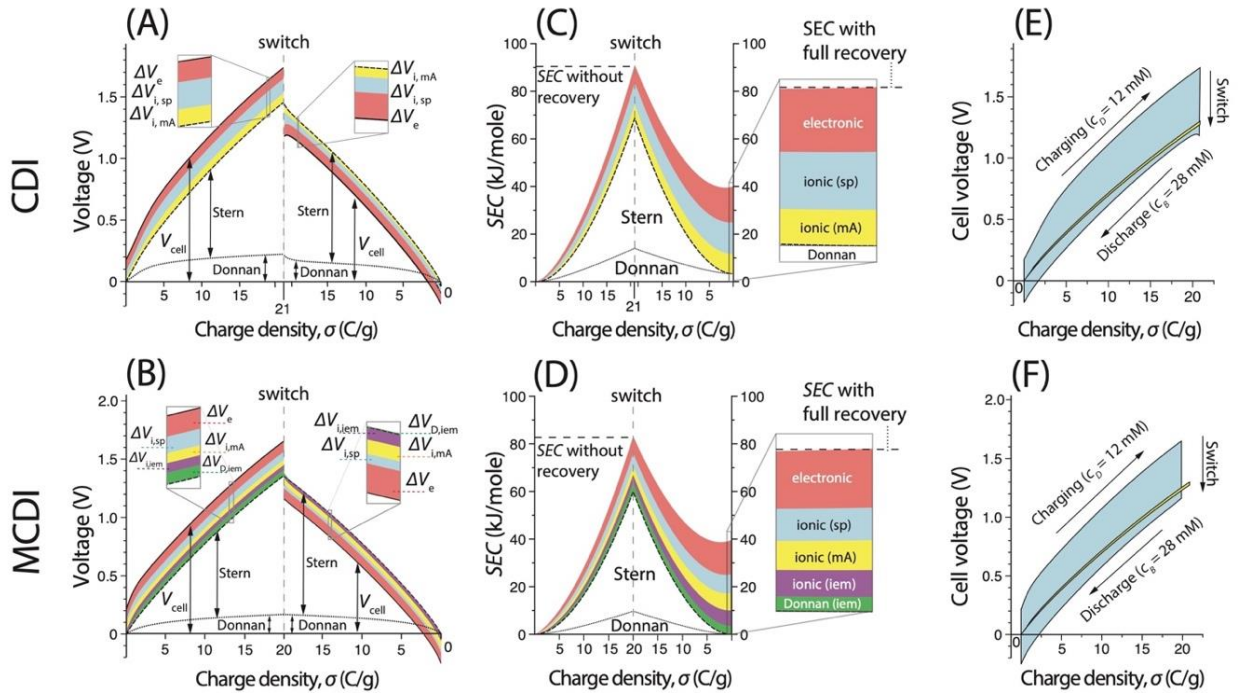

Figure 3.3 (A) and (B): different voltages and potential drops as functions of charge density, σ, for CDI and MCDI processes with CC-RC operations, respectively. (C) and (D): cumulative SEC and its contributions from different mechanisms as a function σ for CDI and MCDI. (E) and (F): simulated cycles with flow-by CC-RC operations (contours of blue region, including the yellow region) and the corresponding thermodynamically reversible cycles (contours of the very thin yellow regions) resulting in the same separation, for CDI (panel E) and MCDI (panel F), respectively. In panel A&B, The solid curves and dash curves represent V_{cell} and V_{eq} (i.e. the sum of Stern and Donnan potentials), respectively. The thickness of each color-coded region represents a potential drop due to the electronic resistance (red), the ionic resistance in the macropores (yellow) or in the spacer channel (blue) in both CDI and MCDI. For MCDI, the potential drop due to the ionic resistance in the IEM (purple) and due to the difference between the Donnan potentials at both membrane interfaces (green) are also plotted. The areas of blue and yellow regions are proportional to *SEC* (with complete energy recovery) and Δg, respectively. In panels A to D, the vertical dash line marked as "switch" represents the end of the charging step when the current direction is switched. The detailed equations and parameters used to generate all the curves in this figure are presented in the Supporting Information.

In the case of CDI without IEM, three major categories of energy losses are considered.[100-102] The first category arises from the electronic resistance in the solid matrix of the electrodes, current collectors, connecting wires, and the imperfect contacts between these components. The second category stems from the ionic resistance in the macropores arising from the limited rate of ion transport through the macropores. The third category is associated with the ionic resistance of the spacer channel due to the limited rate of ion transport across the (half) spacer channel to enter the macropores. The corresponding potential drops of these three categories, denoted as ΔV_e, $\Delta V_{i,mA}$, and $\Delta V_{i,sp}$, are represented by the thicknesses of the red, blue, and yellow regions, respectively. We note that the relative importantance of these contributions is system dependent.

The dashed curve in Figure 3.3A represents the sum of the Donnan and Stern potentials, or in other words, the *equilibrium voltage*, V_{eq}.[72] As a function of σ, $V_{eq}(\sigma)$ can be interpreted as the cell voltage required to maintain the existing σ and ion distribution without either discharging or further charging the system. If a CDI cell is always charged at a cell voltage that is infinitesimally higher than V_{eq}, the current density will be infinitesimal and there is no resistive energy loss. Obviously, this is not a practical operation condition as desalination will take infinitely long.

The total potential drop due to ionic and electronic resistances, quantified by the total thickness of the color-coded region in Figure 3.3A, is the difference between V_{cell} and V_{eq}. This total potential drop is the *excess voltage*, V_{ex}, required to operate the CDI system at a certain current density. The positive value for V_{ex} in the charging step suggests that energy is dissipated to charge the cell at a certain current density, and the negative V_{ex} in the discharge step implies that energy is also dissipated to discharge the cell (i.e., not all capacitive energy is recoverable). We note that V_{ex} increases with current density but not linearly because the ionic resistance depends on the spacer channel salinity which in turn on depends on current density.

Similar charging and discharge curves are also simulated for MCDI to achieve the same separation at the same current density (Figure 3.3B). Similar to the description of CDI in Figure 3.3A, the same concepts of V_{eq} and V_{ex} can be defined for MCDI. Compared to CDI without IEM, two extra potential drops are present in MCDI, including (i) the drop arising from the ionic resistance in the IEM, $\Delta V_{i,mem}$, and (ii) the sum of the Donnan potentials at the two interfaces of the IEMs, $\Delta V_{D,mem}$. The V_{eq} for MCDI includes $\Delta V_{D,mem}$ which originates from ion distribution instead of ion movement, whereas $\Delta V_{i,mem}$ adds to V_{ex} and contributes to the resistive energy

losses. We note that σ at the end of the charging step is higher for CDI (batch cycle, reversible) than for an MCDI process achieving the same separation, because MCDI, with a higher charge efficiency, transfers less charge than CDI to remove the same amount of salt.

Another informative way to present the breakdown of energy consumption in CDI and MCDI processes is to plot cumulative specific energy consumptions as a function of σ for the charging/discharge full cycle (Figures 3.3C and 3.3D), similar to what has been shown by Dykstra et. al.[102, 103] Surprisingly, even though the charge efficiency of MCDI is higher than that of CDI, *SEC* of the two processes, both achieving the same separation and with the same current density, are very similar (without considering possible Faradic reactions). This may be explained by the fact that the additional $\Delta V_{D,mem}$ and $\Delta V_{i,mem}$ in MCDI is offset by the significant reduction of $\Delta V_{i,mA}$ due to the much higher macropore concentration enabled by the IEMs.

The definition of *SEC* based on Equation 3.4 suggests that *SEC* is simply proportional to the area of the cycle encompassing the blue and yellow regions in Figure 3.3E, if complete energy recovery is assumed. Such a cycle is obtained by horizontally flipping the solid discharge curve (i.e. V_{cell} vs. σ) about the axis denoted as "switch" in Figure 3.3A. In comparison, Δg is proportional to the area of the very thin yellow cycle in Figure 3.3E. The yellow cycle represents a thermodynamically reversible CDI cycle obtained using a batch CDI operation. In this specific illustrative example, SEC and Δg are 110 and 4.5 Wh/m^3, respectively, which leads to a *TEE* of 4.07%. Similar comparison between *SEC* and Δg can also be performed using Figure 3.3F for MCDI, which results in a *TEE* of 4.11%.

The analyzed example, characterized with a *TEE* of only ~4.1%, reveals a very important insight for understanding the energy efficiency of CDI or MCDI. In the field of supercapacitors, which are energy storage devices based on the same fundamental principle as CDI, a common metric is the efficiency of energy storage (or "round-trip" efficiency), which is defined as the ratio between the energy released in the discharge step and the energy spent in the charging step.[8, 104] Applying the same concept in CDI, Figures 3.3E and 3.3F suggest that over 50% of energy consumed in the charging step can be theoretically recovered in the discharge step, even if we consider all the resistive energy losses. However, *TEE* by the definition based on Equation 3.2 has been calculated to be only 4.1%. It is of paramount importance to realize that the definitions of "round-trip" efficiency in supercapacitor energy storage and the energy efficiency in CDI are fundamentally different, which can be illustrated using Figures 3.3F and 3.3E. The efficiency of

energy storage, if the system were treated as a supercapacitor, is equal to the ratio of the area below the discharge curve (but above V_{cell}=0) and the area below the charging curve plus the area of the small "triangle" below V_{cell}=0, which is reasonably large.[105] *TEE*, however, is quantified by the ratio between the area of the yellow region, which is very small, and that of the blue region (including the yellow region). Such graphical illustrations clearly show why *TEE* is typically significantly lower than the "round-trip" efficiency of energy storage if the CDI system were treated as a supercapacitor.

In addition to CDI with CC-RC operation, another example that is more often encountered yet easier to analyze for energy efficiency is CDI with constant voltage charging and zero voltage discharge (CV-ZV). Figure 3.4 shows a CV-ZV cycle in which the CDI cell is charged and discharged to equilibrium (i.e. V_{ex}=0 at the end of charging and discharge steps). The separation resulting from this CDI cycle is chosen to be exactly the same as that achieved in the CDI and MCDI process shown in Figure 3.3. Such a CDI cycle with CV-ZV operation is represented in the "V_{cell} vs. σ" diagram as a rectangle with its height representing the charging voltage. For the specific case shown in Figure 3.4, *SEC* and Δg are 303.8 and 4.5 Wh/m^3, respectively, which results in a *TEE* of 1.5%.

Unlike CDI with CC-RC operation in which the energy consumed for transferring a unit charge is strongly dependent on current density and cell resistance, the energy consumption per transferred charge in CV charging is always eV_{cell} (e is the elementary charge). In addition, V_{ex}, as a function of σ, is independent of cell resistance as long as the target separation is achieved by charging and discharging the system to equilibrium (Figure 3.4). With CC-RC operation, as desalination rate is roughly proportional to current density and is thus constant, the resistive energy loss strongly depends on cell resistances. With CV-ZV operation, however, the resistive energy loss is proportional to the area of the blue region (excluding the yellow region) in Figure 3.4 and is thus independent of cell resistance. Therefore, for CDI that is operated in a CV-ZV mode and charged/discharged till equilibrium is reached, *TEE* is already determined once the cell voltage is specified, if parasitic energy losses due to leakage current and Faradaic reaction are not considered. It is important to emphasize again that Figure 3.4 only applies to CV-ZV operations in which equilibrium is reached at the end of the charging step. This may require prolonged charging as the driving force for charge transfer vanishes at the end of the charging step. Faster charging can be achieved by applying a V_{cell} higher than the V_{eq} at the end of the charging step to sustain a positive

driving force (i.e. V_{ex}) throughout the charging step, in which case more energy will be consumed for the same separation and *TEE* will decrease accordingly.

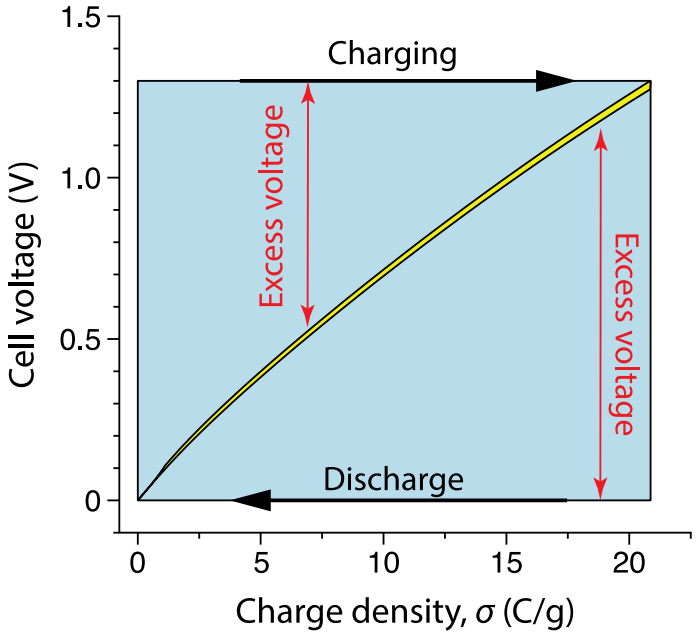

Figure 3.4 A CV-ZV cycle and the corresponding thermodynamically reversible cycle resulting in the same separation. A CV-ZV cycle and the corresponding thermodynamically reversible cycle resulting in the same separation. The CV-ZV is represented by the contour of the blue rectangle (include the yellow region), and the thermodynamically reversible cycle is the contour of the thin yellow region. The resulting separation is the same as that in Figure 3E and 3F.

Last but not least, there is one additional and important energy loss mechanism that is difficult to accurately simulate using the "V_{cell} vs. σ" diagrams shown in Figure 3.3 and 3.4. The parasitic Faradaic reactions that transfer charge to sustain reduction/oxidation reactions at the water/electrode interfaces can result in additional charge transfer that does not contribute to ion removal.[106] This effect is actually considered in charge efficiency, an important metric to be discussed later. Graphically, this makes the blue boxes in Figure 3.3E , 3.3F, and 3.4 considerably longer (in the direction of x-axis) than the yellow reversible cycle that they encompase, which in

turn leads to significantly lower *TEE*. For this reason, MCDI, especially at high current density, is more efficient than CDI without IEMs not only because IEMs mitigate co-ion repulsion from the electrode regime, but also because the presence of IEMs mitigates Faradaic reactions.[12]

3.5. High TEE in (some) CDI processes with intercalation materials

The pursuit of intercalation materials as promising CDI electrode material has been primarily driven by the belief that they can yield much higher specific adsorption capacity (*SAC*) as compared to conventional carbon-based electrodes.[40, 54, 107-110] The higher *SAC* is attributable to the ability of intercalation materials to store ions in their solid phase (i.e. the crystal structure),[40, 111] as compared to carbon electrodes that store ions by forming EDLs in the micropores. Interestingly, the summary of *TEE* in Figure 3.2 suggests that some CDI processes using electrodes based on intercalation materials (i.e. im-CDI, with "im" representing intercalation materials) also achieved significantly higher *TEE* than CDI with carbon electrodes. In fact, according to the studies covered in Figure 3.2, values of *TEE* higher than 10% were only achieved using im-CDI.

In theory, intercalation materials do not seem to have significant *direct* advantage over carbonaceous materials in terms of reducing cell resistance and resistive energy loss. In fact, most intercalation materials have poor electronic conductivity,[112, 113] which is detrimental to achieving high energy efficiency. However, intercalation materials have two major advantages that allow im-CDI systems to be operated in ways that significantly benefit *TEE*. The first advantage is the high *SAC*. Even though *SAC* is not directly relevant to *TEE*, the high *SAC* of intercalation materials enables im-CDI to remove a considerable amount of salt and thereby achieve an appreciable percentage reduction of salinity even when it is employed to desalinate high salinity feed solution.

This advantage has two implications. First, increasing the salinity reduction increases Δg, which has a very strong positive impact on *TEE* according to equation 3.2. This has been clearly demonstrated by the positive correlation between *TEE* and Δg shown in Figure 3.2B. In other words, the higher *SAC* of im-CDI allows it to achieve more "difficult" separations that are strongly beneficial to achieving higher *TEE*. Second, as im-CDI can be employed to desalinate high salinity feed solution, the higher feed salinity, c_0, reduces the ionic resistances in the spacer channel and the macropores which together comprise a significant portion of the overall resistance. The

reduced resistance may have a significant impact on *TEE* if the im-CDI system is operated in a CC-RC mode. However, most im-CDI studies were performed using CV-ZV mode, in which case the impact of cell resistance is primarily on desalination rate.

The second advantage of intercalation materials is the lower V_{cell} than that of carbon electrodes for achieving significant salt removal.[41, 81, 96] This is attributable not only to the higher *SAC* of intercalation materials, but also to the working mechanism of electrodes based on intercalation materials.[40, 111] In the case of carbon electrodes with which salt removal is based on formation of EDLs, V_{eq} rises very sharply as the electrodes are charged. A significant part of V_{eq} is the Stern potential as shown in Figure 3.3A and 3.3B. Electrodes with intercalation materials employ very different mechanisms for ion storage, with which the equilibrium may be described by the Frumkin intercalation isotherm.[111, 114, 115] For electrodes based on intercalation materials, the increase of V_{eq} as a function of charge density is significantly slower than that for carbon electrodes. In other words, im-CDI stores less energy in the charging step than CDI based on carbon electrodes for removing the same amount of salts.

With CC-RC operation, the amount of the "stored energy" at the end of charging step theoretically does not have impact on energy consumption if it can be fully recovered (excluding the resistive loss) in the discharge step, as in this case the energy consumption is primarily the resistive energy loss. However, no practical CDI process can fully recover the "stored energy" in the discharge step, which renders im-CDI more advantageous as less "stored energy" is available to lose. This is even more the case for CV-ZV operation adopted by most reported studies evaluated in this paper, as all "stored energy" is lost with ZV discharge. As Figures 3.3E, 3.3F and 3.4 illustrate, *TEE* is simply the ratio between the area of the yellow cycle (representing Δg) and the area of the blue boxes (representing *SEC*). The use of im-CDI, which has a lower V_{eq} at a given charge density, lowers the height and reduces the size of the blue rectangle, thereby leads to a higher *TEE*.

Based on the definition of *TEE* and following the above analysis, there should be a correlation between *TEE*, Δg, Δc, Λ_{Dyn} and ΔV_{cell}, following the form described in equation 3.6

$$TEE \approx \beta \frac{\Delta g \Lambda_{dyn}}{\Delta V_{cell} \Delta c} \tag{3.6}$$

Here, ΔV_{cell} is the difference between the charge-averaged (i.e. not time-averaged) voltages in charging and discharge steps, which is exactly equal to the charging voltage for CV-

ZV operation and roughly equal to the average height of the blue region in Figure 3.3E and 3.3F for CC-RC operation, and Λ_{dyn} is the dynamic charge efficiency to be further discussed in the section after next. The coefficient β is a constant that depends on the specific units chosen for the parameters. Equation 3.6 is proposed based on the argument that SEC_w is roughly proportional to $\Delta V_{cell}\Delta c/\Lambda_{dyn}$ (Supporting Information for detailed explanation).

We apply equation 3.6 to a subset of the data in Table S1 that provide sufficient information to calculate ΔV_{cell} and Λ_{dyn}. The results suggest that the correlation given by equation 6 works reasonably well, especially for im-CDI (Figure 3.5). The goodness of fit is less satisfactory for CDI with carbon electrodes, but the overall trend of *TEE* is successfully captured by the correlation. This correlation can be employed to justify the very high *TEE* of some im-CDI processes. For example, the two data points with the highest *TEE* were obtained from a im-CDI study that used a V_{cell} of only 0.55 V and ΔV_{cell} as low as 0.1 V,[41, 81] considerably lower than that in most other studies, to achieve Δg that are one to several orders of magnitude higher than that achieved by other studies.

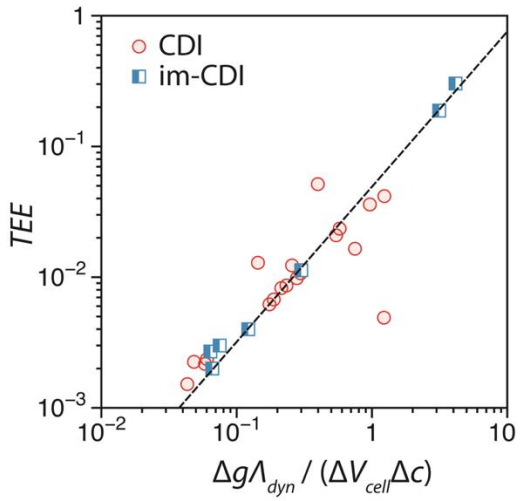

Figure 3.5 TEE vs. $\Delta g\Lambda_{dyn}/(\Delta V_{cell}\,\Delta c)$ for CDI with carbon electrodes (red circles) and im-CDI with electrodes based on intercalation materials (blue squares). The coefficient of determination is R^2=0.82. The specific position of the data cluster is dependent on the choice of units for different parameters, but the relative positions of the data points in the cluster and the goodness of fit is independent of unit choice.

Lastly, it is important to point out that many im-CDI systems employ a configuration that is fundamentally different from most configurations used in CDI with carbon electrodes. While silver electrodes have been used as anion (Cl^-) electrodes in one im-CDI study,[41] other im-CDI studies adopt a configuration that involves two cation intercalation electrodes (i.e. no electrode for anion adsorption) separated by an odd number of IEMs.[40, 90, 96, 109] The working mechanism of im-CDI systems with such a configuration is to a great extent similar to electrodialysis. Due to the very different configurations and ion-removal mechanisms between this specific type of im-CDI and typical CDI, the results from the above analysis comparing the energy efficiency of im-CDI and CDI must be interpreted with caution.

3.6. Energy efficiency and desalination rate: an intrinsic trade-off significance

In this section, we will discuss how the desalination rate affects *TEE*, as desalination rate is strongly related to ΔV_{cell}, which has a strong impact on *TEE* according to equation 3.6. In general, an effective way to enhance *TEE* is to reduce the resistive energy loss, which is graphically equivalent to reducing the area of the blue regions in Figure 3.3E, 3.3F and 3.4. With CV-ZV operation, this can be achieved by reducing the charging voltage. However, a reduced charging voltage leads to a reduced excess voltage which, with the same cell resistance, inevitably results in slower desalination. This inherent tradeoff between energy efficiency and desalination rate can also be quantified using the example of CC-RC operation in which desalination rate is roughly proportional to the current density that is constant. Here, we will quantify such a tradeoff by systematically evaluating an MCDI process with CC-RC operation at different desalination rate.

The quantification of desalination rate and energy consumption typically requires normalization to obtain scale-independent performance metrics. There are two general approaches for normalization. In the first approach, the performance metrics are normalized by the amount of removed salt. In this case, the desalination rate is quantified using average salt adsorption rate ($ASAR$), defined as the amount (either mass or mole) of salt adsorbed by unit electrode mass in unit time,[76] and *SEC* is defined as energy consumed per amount (either mass or mole) of salt removed (example unit: J $mole^{-1}$).[27] We denote *SEC* with this definition as SEC_i with the subscript "*i*" representing "ions".

The second approach, which is more relevant for practical evaluation and optimization of CDI processes for which Δc has been specified as the treatment goal, involves normalizing the desalination rate by the volume of the deionized product water. With this approach, the desalination rate is quantified by productivity, *P*, defined as the volume of product water generated by a unit area of electrode in a unit time.[77] Productivity has exactly the same unit as flux that is extensively used to quantify the desalination rate in RO. *SEC* in this case is defined as energy consumed to produce a unit volume of deionized (example unit: Wh m^{-3}), which we will denote as SEC_w with the subscript "*w*" representing "water". SEC_w is also consistent with the adopted approach for quantifying energy consumption in RO.[45, 116] We note that the approach of normalizing by the amount of removed salt is the most adopted approach for reporting *SEC* in most existing CDI literature, because SEC_i is more sensible than SEC_w for comparing different CDI processes with different salinity reduction.

A tradeoff curve can be constructed by plotting either the inverse of SEC_i (i.e. SEC_i^{-1}) as a function of *ASAR* or the inverse of SEC_w (i.e. SEC_w^{-1}) as a function of *P*. We note that SEC_i^{-1} has the same meaning as what has been called in literature as energy normalized adsorbed salt, *ENAS*.[101] The use of the inverse of *SEC* instead of *SEC* itself leads to a tradeoff curve that is monotonically decreasing, which is a more intuitive representation of a tradeoff relationship. We note that the conversion between SEC_i (or *ENAS*) and SEC_w, and between *ASAR* and *P*, can be readily performed if the salinity reduction Δc ($= c_0 - c_D$) and flowrate are known.[77, 117] A tradeoff curve is meaningful only if all points on a tradeoff correspond to the same separation. While current density can be readily controlled, the key in establishing a tradeoff curve in flow-by CDI processes is to simultaneously adjust the feed flowrate so that Δc remains constant at different current densities. Using this approach, tradeoff curves have been established both experimentally and by simulation.[77, 117] For illustration, simulated tradeoff curves are presented in Figure 3.6.

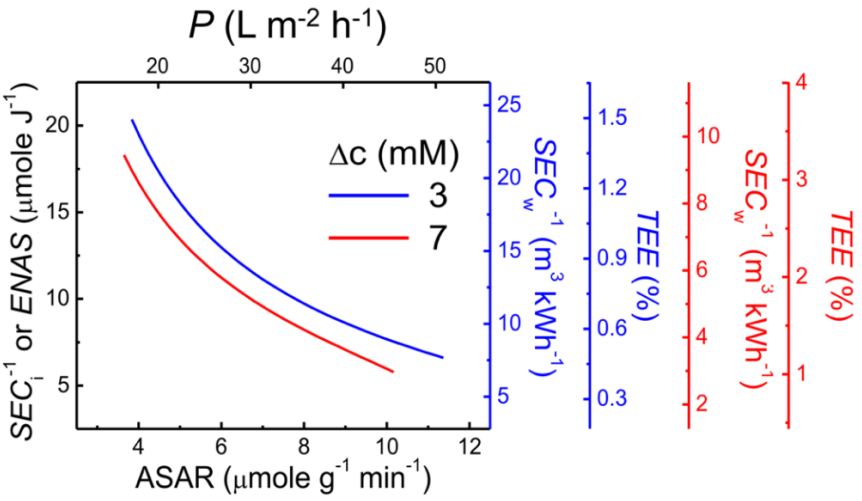

Figure 3.6 Example tradeoff curves that quantify the relationship between desalination rate (*ASAR* or *P*) and energy efficiency (*ENAS*, SEC_w^{-1}, or *TEE*). The tradeoff curves are simulated for an MCDI process with a feed solution of 20 mM and a water recovery of 50%.

The tradeoff curves in Figure 3.6 suggest that energy efficiency, as quantified by either inverse of *SEC*, is roughly inversely proportional to desalination rate, as quantified by either *ASAR* or *P*. Because all points on a tradeoff curve correspond to the same separation and thus the same Δg, *TEE* is simply proportional to SEC_w^{-1} for a given tradeoff curve (Figure 3.6, additional y-axis). Therefore, *TEE* is also inversely proportional to desalination rate. Because each tradeoff curve illustrated in Figure 3.6 involves a single MCDI system and results in the same separation, it suggests that *TEE* does not only depend on the resulting separation or the "goodness" of the CDI system, but also strongly on how fast the CDI process is performed to achieve the target separation. Enhancing the desalination rate inevitably consumes more energy (moving down the tradeoff curve), and vice versa.

3.7. Charge efficiency: correlation to energy consumption revisited

Another important and widely investigated performance metric strongly related to energy efficiency is the charge efficiency, Λ.[118-121] Charge efficiency, defined as the amount of adsorbed

salt over transferred charge, quantifies how efficient a CDI process utilizes charge transfer for ion adsorption.[1, 13] A recent study by Hawks et.al. suggests that the charge efficiency calculated using experimentally measured effluent salinity, which has been named dynamic charge efficiency, Λ_{dyn}, is not exactly Λ by its very definition.[122] The discrepancy is attributable to the fact that the charging step actually removes more salt from the feed solution than the measured salinity reduction suggests, as some adsorbed salt is released back to the deionized solution (in the spacer channel) that has not exited the CDI cell upon the charging/discharge switch. A metric named flow efficiency, Λ_{flow} (= Λ_{dyn}/Λ), which was introduced by Johnson and Newman,[123] was adopted to account for this effect. The flow efficiency is close to unity, which is desirable, if the residence time is considerably shorter than the charging time. We note that Λ_{flow} cannot be directly measured using experiments but has to be evaluated using a model with certain assumptions.[122] In addition to the effect accounted for by Λ_{flow}, we note that Faradaic reactions also contributes, but with different mechanism from co-ion repulsion, to the undesirable "waste" of electron transfer captured in Λ_{dyn}.

Many studies have been performed to investigate the dependence of Λ_{dyn} on operating conditions.[10, 11, 13, 43] It has been suggested, with supporting experimental evidence, that *SEC* negatively correlates with Λ_{dyn}.[76] Specifically, an inverse proportionality has been proposed to capture the dependence of SEC_i on Λ_{dyn} (see Figure 3.5 in the classic review paper by Suss et.al.).[76] Such a conclusion was primarily based on one large experimental data set in which the SEC_i and Λ_{dyn} were measured at different influent feed salinity with or without IEMs.[11] The most salient feature is that SEC_i has a clear negative correlation with Λ_{dyn}, which is particularly strong when Λ_{dyn} is low.

The inverse proportional correlation between SEC_i and Λ_{dyn} is theoretically justified by simply combining Equations 3.2 and 3.6 and noting that $SEC_i = SEC_w/\Delta c$:

$$SEC_i = \frac{1}{\beta}\frac{\Delta V_{cell}}{\Lambda_{dyn}} \tag{3.7}$$

However, equation 3.7 also suggests that SEC_i is strongly dependent on ΔV_{cell}. This implies that any inverse proportionality observed in a series of data is not universal but rather conditional upon the requirement of constant ΔV_{cell} for all data points in that series (e.g. all data points in such a series were collected from CV-ZV operation with the same charging voltage).

That is, SEC_i is not a simple one-to-one function of Λ_{dyn} as a universal inverse proportionality would have suggested.

For example, we analyze a set of data obtained in a recent study of MCDI with CC-RC operation and different operating conditions.[117] Due to the presence of IEMs, Λ_{dyn} is relatively high for the entire data set. The correlation between SEC_i and Λ_{dyn} is very weak (Figure 3.7A): within a relatively small range of relatively high values for Λ_{dyn} (from 0.70 to 0.97), *SEC* varies, without observable trend, from 0.054 to 0.243 J/μmole. Specifically, comparing data from experiments performed with two different sets of electrode materials suggests that the FM10K carbon cloth electrodes (red circles in Figure 3.7) consume more energy than PACMM electrodes (blue circles in Figure 3.7A) for achieving the same separation, even when their Λ_{dyn} values are very similar. Performing the same analysis using Λ, which was calculated using Λ_{dyn} and the flow efficiencies estimated using the approach proposed in ref. [[122]], slightly shifts the position of the data cluster but did not change the qualitative conclusion of the lack of correlation.

Dynamic charge efficiency is of critical significance because a low Λ_{dyn} means a large fraction of the energy is spent on charge transfer that does not result in ion removal from the bulk solution.[13, 76, 118] The "wasted" charge transfer can be attributed to co-ion repulsion, unintended discharging into already deionized water (as characterized by flow efficiency), and in some cases, also to Faradaic reactions. In contrast, a high Λ_{dyn} means that most of the energy is spent on charge transfer that results in ion removal from the bulk solution. Therefore, Λ_{dyn} quantifies the "utility" of charge transfer. However, SEC_i does not only depend on the utility of charge transfer but also strongly depends on how much energy is actually consumed to transfer charge, which is roughly quantified by $e\Delta V_{cell}$. Therefore, while a CDI process with low Λ_{dyn} cannot be energy efficient, a CDI process with very high Λ_{dyn} is not necessary energy efficient as much energy can be consumed for charge transfer (e.g. when resistance is high and/or desalination rate is fast, which leads to a large ΔV_{cell}). In summary, a high Λ_{dyn} is only a necessary, but not a sufficient, condition for an energy-efficient CDI process.

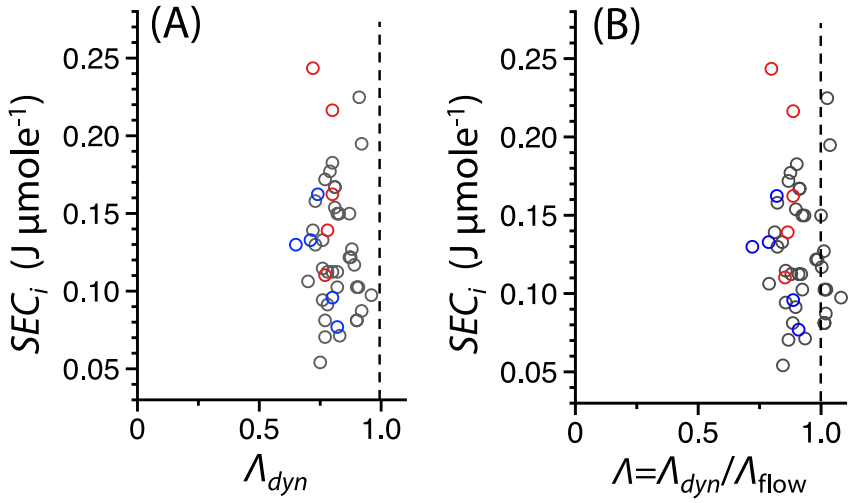

Figure 3.7 (A) *SEC* vs. Λ_{Dyn} and (B) *SEC* vs. Λ ($=\Lambda_{dyn}/\Lambda_{flow}$) for a series of data obtained using MCDI experiments reported by Ref. [117]. We note that $\Lambda>1$ is observed, likely due to errors in estimating the flow efficiency using a model with several ideal assumptions and/or the uncertainty in estimate the cell's fluid volume.

3.8. Conclusions

The recent intensive research pursuit in CDI has been to a certain extent motivated by the promise it may soon become a low-energy-consumption alternative to conventional and more mature desalination technologies. On the one hand, CDI is indeed a low-energy-consumption technology, as the majority of CDI studies have reported SEC_w values that are significantly lower than that of any typical desalination technologies. On the other hand, the very low SEC_w values of many CDI processes do not suggest that they are highly energy efficient, because the majority of reported CDI processes were employed to achieve "easy" separations that intrinsically require very little energy to achieve. The concept of *TEE* helps us account for the "difficulty" of separation when interpreting the energy consumption and assessing the energy efficiency of CDI processes. While no study on CDI with carbon electrodes has yet shown a *TEE* higher than 10%, CDI with electrodes based on intercalation materials have shown *TEE* as high as 40%. It suggests that it is possible for CDI to achieve a *TEE* in the same order of magnitude as that for RO, the state-of-the-art desalination technology. Our analysis also suggests that several factors are associated with high

TEE. These factors, which are summarized in Table 1, contribute to either a higher Δg or a lower SEC.

It is important to emphasize that, although *TEE* is an important performance metric, it is not a very useful performance metric for the purpose of designing and optimizing a CDI system to meet a certain desalination (i.e. reducing the feed salinity to a target effluent salinity). While we understand that achieving higher Δg is beneficial to enhancing *TEE*, we cannot and should not desalinate more saline feed water just for pursuing a higher *TEE*. Even with a given feed solution, we should not desalinate more than necessary to achieve a higher Δc just for a higher *TEE*, as doing so will lead to higher SEC_w which has more direct relevance to cost of water production. In general, it has been proposed that the technoeconomic analysis of CDI systems should simultaneously consider energy consumption and desalination rate on the basis of their tradeoff relationship.[77, 117] In this context, the energy consumption should be quantified using SEC_w which again has more direct relevance (than *TEE*) to practical cost consideration.

The use of *TEE* as a performance metric, however, helps us acquire a better understanding of how efficient various CDI processes are, which cannot be judged based on absolute performance metric such as SEC_i or SEC_w. For a specific CDI process, *TEE* helps us gauge how much room there is to further enhance the energy efficiency and understand the limit of *SEC* (which is essentially Δg). Within the research field, *TEE* enables us to compare across different processes that result in different separations and to identify strategies for enhancing the energy efficiency of CDI. Last but not least, *TEE* is the only performance metric that allows direct comparison of energy efficiency between different desalination technologies with vastly different working mechanisms and achieved separations. For example, it is very challenging to compare CDI with RO or thermal desalinations using *SEC*, due to the fact that not all technologies can be operated to achieve the same separation. Such a comparison, which may be imperfect yet informative, can be best achieved using *TEE*.

Table 3.1 Summary of factors associated with high *TEE*

	Factors	Mechanism	Note
	High salinity feed solution*	• reduce ionic resistance (*SEC* ↓)	Reduced ionic resistance increases *TEE* for CC-RC operation. For CV-ZV, it leads to faster desalination and does not affect *TEE*.
	More salinity reduction*	• more difficult separation (Δg ↑)	
	Energy recovery in the discharge step	• reduce effective energy use (*SEC* ↓)	Must be implemented to achieve very high *TEE*.
	Improved electrode and cell design	• reduce electronic and/or ionic resistance (*SEC* ↓) • minimize parasitic loss (*SEC* ↓) • improve flow efficiency (*SEC* ↓)	The most recognized strategy to enhance CDI performance. Also see note for factor (A) for CV-ZV operation.
	Low desalination rate#	• reduce "driving force" (*SEC* ↓)	Can be achieved by charging at low current density or voltage§. Loss due to parasitic reactions become significant when desalination rate is too low.[75]
	High charge efficiency Λ_{dyn}	• maximize the "utility" of charge transfer (*SEC* ↓)	Λ_{dyn} should be maximized but high Λ cannot guarantee high *TEE*.
	Use of intercalation electrodes	• more salinity reduction (see B, Δg ↑) • reduce charging voltage for the same separation (*SEC* ↓)	Lower charging is particularly beneficial to *TEE* when energy recovery is poor or absent.
	Batch mode	• eliminate "flow system limitations" (*SEC* ↓)	Relatively insignificant impact on practical systems unless *TEE* becomes very high.

* For a given desalination need (i.e. reducing the feed salinity to a target effluent salinity), these are not practical strategies to reduce energy consumption;

Lower desalination rate leads to a larger system and higher capital costs;

§ If the system is charged in CV mode until equilibrium is reached, charging voltage depends on the equilibrium charge density required by the target separation and cannot be freely adjusted. In other words, V_{cell} can be adjusted in CV mode to achieve the same separation but different desalination rate only if V_{cell} is higher than V_{eq} at the end of the charging step.

CHAPTER 4

KINETIC AND ENERGETIC TRADOFF IN MEMBRANE CAPACITIVE DEIONIZATION

This chapter has been published in the journal *Water Research* as part of the following peer-reviewed manuscript: Wang L., Lin S., Intrinsic tradeoff between kinetic and energetic efficiencies in membrane capacitive deionization. Water Research. **129** (2018). p. 394-401. doi:10.1016/j.watres.2017.11.027

4.1. Overview

Capacitive deionization (CDI) is an emerging desalination technology based on the formation of electrical double layers (EDLs) in the electrode micropores [1, 124]. While the state-of-the-art desalination process still remains reverse osmosis (RO) [27], it has been suggested that CDI may compete with RO for desalinating brackish water with low to moderate salinity [8, 9, 125]. Specifically, it has been suggested that, under certain circumstances, CDI is more energy efficient than RO for brackish water desalination. But more importantly, CDI has other operational advantages that may render it the technology of choice for desalinating inland brackish water, especially in remote areas where large scale infrastructure is not accessible [4, 21]. For example, CDI does not have any high pressure or high temperature components, which reduces the capital cost especially for small scale treatment systems. CDI is also strongly adaptable: the operating conditions can be readily adjusted for different feed water quality and target product water quality [11]. In addition, the absence of pressure driven permeation in CDI and the presence of periodic reversal of electric field also render CDI less susceptible to fouling problems that are common in RO. Last but not least, CDI is compatible with renewable energy the supply of which is often highly intermittent [126].

The research field of CDI has experienced an exponential growth in the past decade, with progress made in multiple directions. Various system configurations [16, 17, 59, 89, 127] and operation modes [11, 43, 61, 71, 104] have been developed to enhance the energy efficiency [11, 43, 61, 104] and mass transfer kinetics of CDI [71], to improve the electrodes' salt retention capacity [65, 128] and long-term

chemical stability [89, 129], and to enable continuous operation [16, 17, 64]. In particular, the introduction of ion exchange membranes to CDI system to mitigate co-ion repulsion has been shown to significantly enhance the energy efficiency of CDI and enable the more flexible and efficient constant current operation [127, 130]. Such a configuration, namely membrane CDI (MCDI), has widely been adopted due to its higher energy efficiency over CDI without membranes [11, 59]. Other active research areas in CDI include the development of high performance electrodes [33, 131-136], and advancing our fundamental understanding on the energy efficiency of, and mass transport phenomena in, CDI [13, 43, 101, 137, 138].

For a given CDI system, there are several primary operating parameters to control, including applied voltage or current, flow rate, charging and discharge durations. Optimizing system design and operation of a CDI system requires understanding the impacts of these parameters on system performance. To attain such understanding, however, system performance first needs to be defined. Previous studies have investigated the effect of current density on the mass transfer kinetics, quantified by average salt adsorption rate (*ASAR*), and the salt adsorption capacity (*SAC*) [139]. A tradeoff was identified between *ASAR* and *SAC*, which is analogous to the tradeoff between power density and energy density featured in the famous Ragone diagram for supercapacitors. However, while the *SAC* at a given operating conditions might be a critical parameter in evaluating the performance of an electrode, its implication on practical CDI operations is limited. After all, what matters most to a desalination process are, among other factors, how fast the process occurs and how much energy it consumes. In other words, the kinetic and energetic efficiencies should be the central performance indicators.

The energy efficiency of a desalination process is often quantified using specific energy consumption (*SEC*), typically defined as the energy consumed to generate unit volume of product water [116]. For CDI, however, *SEC* is more often defined as the energy consumed to remove a unit mole (or mass) of salt [11], which will be definition adopted in this study. While many existing studies concerned the SEC of a CDI operation and reported different ways to improve it, the discussion of energy efficiency should not be divorced from that of kinetic efficiency as there is an inherent tradeoff between the two. Quantifying the tradeoff between kinetic and energetic efficiencies is essential to optimizing the design and operation of an RO system [45], which has not been systematically conducted for CDI. On the other hand, one cannot attain such a tradeoff by simply varying the current density of a CDI operation while maintaining all other parameters

constant, because operations with different current densities may result in different effluent salinities and thus different underlying separations. Comparison of SEC between CDI processes resulting in different separations is problematic because different separations inherently require different Gibbs free energy of separation[82]. Therefore, a rational comparison of kinetic and energetic performance between different CDI operations has to be conducted in a way that the effluent salinity and the underlying separations are kept constant.

In this study, we experimentally and theoretically quantify the kinetics-energetics tradeoff in MCDI. The configuration of MCDI is chosen because (1) it is significantly more energy efficient than CDI without ion exchange membrane and thus expected to be more widely adopted in practice; and (2) because it allows constant current charging which is the chosen operation mode in our study. The kinetics-energetics tradeoff is quantified using *ASAR* and the inverse of specific energy consumption (SEC^{-1}) from MCDI experiments in which the current density and flowrate are simultaneously varied to achieve the same separations with different kinetic efficiencies. We also systematically assess the impacts of several parameters on the kinetics-energetics tradeoff. These parameters include the feed salinity, diluted water salinity, diluted water volume per charging cycle, and electrode materials. Finally, we discuss the implications of these tradeoff curves and demonstrate how they can be employed for optimizing system design and operation and for comparing the performance of electrode materials.

4.2. Materials and Methods

4.2.1. MCDI module.

The MCDI stack comprised 4 parallel cells that were sandwiched in an acrylic housing. Two types of electrode, a film electrode casted with activated carbon particles, PACMM (PACMM 203, Material Methods, Irvine, CA, USA, δe_1=290 μm) and an activated carbon cloth FM10K (Zorflex®, Pittsburg, PA, USA, δe_2=350 μm), were used in this study. Each cell consists of a pair of graphite foil as current collectors (Alfa Aesar, thickness δ=130 μm), a pair of porous electrodes (PACMM or FM 10K), a pair of anion- and cation-exchange membranes (Neosepta AMX, δ_{mem}=140 μm, and Neosepta CMX, δ_{mem}=170 μm, Tokuyama Co., Japan), and a glass fiber spacer

(Whatman, δ=250 μm). Each electrode was cut to a 6×6 cm^2 square with a 1.5×1.5 cm^2 square hole at the center, yielding a total active electrode area of 270 cm^2 for the entire stack. A peristaltic pump drives the water to enter from the periphery of the square MCDI stack, flow along the spacers sandwiched between the ion exchange membrane/electrode assemblies, and exit from the center square hole. A schematic showing the MCDI structure and flow direction is provided in the Supplementary Information. The total mass of the 4 pairs of electrodes were 2.56 g and 4.29 g for PACMM and FM 10K, respectively.

4.2.2. Experimental methods and design.

NaCl solutions were used as the model feed solution throughout the study. The feed solution was stored in a 10L feed tank with constant nitrogen purging to minimize the oxygen content for mitigating electrode oxidation. The feed solution was pumped through the MCDI stack by a peristaltic pump and the effluent of MCDI stack was sent back to the feed tank. The conductivity of the effluent was measured by a flow-through conductivity meter (isoPod EP357, eDAQ, Australia) installed right at the exit of the stack, which was further converted into salt concentration according to a pre-established calibration. Although pH fluctuation has been observed in previous CDI experiments due to possible oxidation/reduction of the carbon electrodes[140, 141], the measured concentrations of H^+or OH^- in the effluent is orders of magnitude lower than the NaCl concentration used in our experiments. It is therefore reasonable to assume that the removal of NaCl by a pair of electrodes is asymmetric, i.e., equal amount of Na^+ and Cl^- ions are removed in the CDI system. Desalination performance was evaluated with constant current charging and zero-voltage discharge as controlled using a potentiostat (SP 150, Bio-Logic, France) that recorded the real-time current and cell voltage.

To obtain a kinetics-energetics trade-off curve, we conducted MCDI experiments with different current densities and evaluated the *ASAR* (mg g min^{-1}), which represents the kinetic efficiency, and *SEC* (J mg^{-1}), which represents the energy efficiency. Previous studies using different current densities adopted an operation protocol that used a constant flow rate and terminated the charging when the cell voltage reached a pre-determined value [11, 139]. However, such a protocol led to different effluent salinities and thus achieved different underlying

separations. In this study, we choose to use a different approach by adjusting the flow rate to the various charging currents to maintain the same effluent salinity, and thereby achieving the same underlying separation with different current densities. The flow rates leading to the target effluent salinity were obtained using trial-and-error method. The impacts of feed concentration (c_0), diluted water concentration (c_D), volume of diluted water(V_D), i.e. volume of the effluent in the charge stage, and electrode materials on the kinetics-energetics tradeoff were systematically evaluated, with detailed conditions for different sets of experiments summarized in Table 4.1.

4.2.3. Data analysis

The kinetic efficiency of MCDI operations were quantified using *ASAR* defined as the mass of salt removed per gram of electrode per time. We only evaluated the *ASAR* for the charging half-cycle following convention, even though *ASAR* can also be defined based on the full charging and discharge cycle. *ASAR* (mg g min^{-1}) is calculated according to the following equation:

$$ASAR = MW_{NaCl}\frac{Q\int_0^{t_C}(c_0 - c(t))dt}{w_e t_C} \tag{4.1}$$

where MW_{NaCl} is the molecular weight of NaCl, c_0 is the salt concentration (mM) of the feed (or influent) stream, $c(t)$ is the effluent salt concentration (mM) and should be constant short after charging starts, Q is the flowrate (L min^{-1}), w_e is the total mass of electrodes (g), and t_C is the charging time (min).

The energetic efficiency of the process is quantified using *SEC* defined as the energy consumed (J) to remove a unit mass of salt (mg). *SEC* is calculated using equation 2 from experimental data:

$$SEC = \frac{I\int_0^{t_C}V(t)dt}{MW_{NaCl}Q\int_0^{t_C}(c_0 - c(t))dt} \tag{4.2}$$

where I is the applied current (A), and $V(t)$ is the time dependent cell voltage (V).

Table 4.1 Experimental conditions in MCDI tests

		Flow rate (mL/min)				
Applied Current (mA)		120	100	80	60	40
Current Density (mA/cm^2)		0.89	0.74	0.59	0.44	0.30
Series 1: Effluent concentration, c_D ($c_0 = 20$ mM, $V_D = 28.5$ mL, PACMM)	10 mM	7	5.6	4.2	3.9	2.7
	13 mM	9.5	8.1	6.4	4.8	3.4
	16 mM	13.0	11.8	9.5	7.7	4.5
Series 2: feed concentration, c_0 ($c_D = 13$ mM, $V_D = 28.5$ mL, PACMM)	16 mM	15.2	12.5	10.9	8.3	6.0
	20 mM	9.5	8.1	6.4	4.8	3.4
	24.2 mM	6.7	5.5	4.4	3.3	2.2
Series 3: diluted water volume, V_D ($c_0 = 20$ mM, $c_D = 13$ mM, PACMM)	19 mL	9.5	7.8	6.4	5.0	3.3
	28.5 mL	9.5	8.1	6.4	4.8	3.4
	33 mL	9.5	7.8	6.2	5.0	3.3
Series 4: Electrode Material ($c_0 = 20$ mM, $c_D = 16$ mM, $V_D = 33$ mL)	PACMM	13.0	11.8	9.5	7.7	4.5
	FM10K	16.8	14.3	11.0	8.3	5.4

In this study, we will quantify the kinetics-energetics tradeoff using the relationship between *ASAR* and the inverse of *SEC*, i.e., SEC^{-1} (unit: mg J^{-1}). The interpretation of SEC^{-1} is the mass of salt removed per amount of energy spent, which also serves equally well, if not even better, as an intuitive metric for energy efficiency. The charge efficiency, defined as the ratio between the salt removal and the electrical charge transferred between the electrodes, is calculated following equation 4.3:

$$\Lambda = MW_{NaCl} Q \frac{\int_0^{t_c} (c_0 - c(t)) dt}{I t_c} \quad (4.3)$$

4.3. Theoretical Modeling

We employed a one-dimensional MCDI model to fit our experimental data. The model only considers transport of ions in the direction normal to the membrane/electrode assembly, which is a reasonable approximation as the average travel distance along the spacer was only 2.6 cm in our system. The model assumes two scales of porosity for the electrode material: nanoscale micropores, which are responsible for the majority of the ion storage capacity, and microscale macropores, which provide pathway for fast ion transport. The modified Donnan (mD) model is employed to describe the potential difference between micropores and macropores [10, 33, 142]. Various resistive and interfacial potential drops within the cell are considered, so are external resistive potential drops outside the cell [100, 143]. The spacer channel resistance varies as ions are removed from or released to the spacer channel, and is thus time dependent [71]. The details of the model derivation are provided in Supplementary Information.

4.4. Results and Discussion

4.4.1. Experimental results and model validation

Four series and eleven sets of experiments (including 55 experiments in total) were conducted to investigate the effects of diluted water concentration, feed concentration, diluted water volume (per charging half-cycle) and electrode materials. Fig 1a presents the experimental data (solid curves) for one set of experiments (c_0 =20 mM, c_D = 13 mM, and v_D =28.5 mM) with PACMM electrodes. Upon the initiation of charging, the effluent concentrations declined and reached a stable effluent concentration (the target c_D) before long. Within this set of experiments, the flowrates were adjusted according to the applied current to maintain the same effluent concentration. The increase of flowrate is reflected by the shorter time for the charging half-cycle,

because the total diluted water volume was kept at 28.5 mL. The voltages across the MCDI stack increased sharply upon the start of charging and then transitioned to a linear regime (Fig 1b). Both the starting voltages and the slopes of linear regime were larger with higher currents, because the concentration-dependent spacer resistance increased faster due to faster removal of charged ions at higher current.

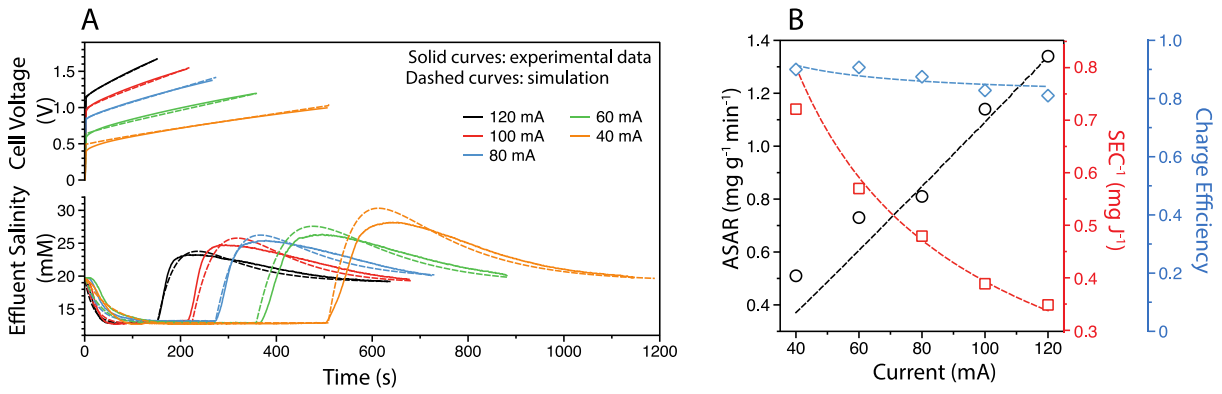

Figure 4.1 (A) Experimental and simulation results of the effluent concentration (bottom half) and cell voltage (top half) for MCDI process with constant current charging and zero-voltage discharge. The solid curves represent experimentally measured data, whereas the the dashed curves represent the data simulated using the MCDI transport model. Only the cell voltage of the charging half-cycle is reported, as that of the discharge half-cycle is set to be zero. Experimental conditions used in this series of experiments: c_0 =20 mM, c_D = 13 mM, and v_D =28.5 mL. The flowrates are 9.5 mL/min, 8.1 mL/min, 6.4 mL/min, 4.8 mL/min and 3.4 mL/min for currents of 120 mA, 100 mA, 80 mA, 60 mA and 40 mA, respectively. (B) ASAR (left y-axis, black), SEC (right y-axis, red), and charge efficiency (right y-axis, blue) as functions of current. The open symbols are experimental data, wherease the dashed curves are simulated results.

Experimental *ASAR* and SEC^{-1} were calculated following the method described in Data Analysis, with the results shown in Figure 4.1B. These results correspond to the raw data presented in Figure 4.1A. As the electrical current increased from 40 mA to 120 mA, *ASAR* increased, roughly proportional to the increase of the current, from 0.51 to 1.34 mg g^{-1} min^{-1}. On the other

hand, SEC^{-1} diminished from 0.72 mg J^{-1} at 40 mA to 0.35 mg J^{-1} at 120 mA. The opposite trends of *ASAR* and SEC^{-1} with respect to increasing electrical current clearly demonstrate the trade-off between the kinetic and energetic efficiencies in a MCDI processes: a faster process can be attained at the cost of spending more energy to achieve the same separation. This trade-off will be systematically discussed in the following sections. It is also worth noting that the charge efficiency also decreased with increasing current, but only to a small extent (Figure 4.1B). The charge efficiency, by definition, captures how much energy spent on transferring charges is actually utilized in removing ions. However, it does not account for how fast the charges are transferred and the ions removed, which certainly has a strong impact on the energy consumption based on the kinetic-energetic tradeoff. Therefore, charge efficiency should not be interpreted as equivalent to energy efficiency.

The experimental results from Figure 4.1A are fitted with simulated results from the MCDI transport model described in the theory section (with details provided in Supporting Information). With a single set of parameters (for each electrode) consistent with those reported in literature and being used consistently in all our simulations (Table 4.2), the MCDI model can generate simulation results that fit the experimental results with excellent precision. The experimental and simulation results are particularly matched for the charging half-cycle which is of the most significance in the current study. Theoretical predictions of SEC^{-1} and *ASAR* from the simulated effluent concentration and cell voltage profiles were also validated using the experimentally measured results (Figure 4.1B). Overall, the MCDI dynamic ion transport model can provide very good prediction of the system performance of our MCDI stack.

4.4.2. Kinetics and energetics tradeoff

The *ASAR* vs SEC^{-1} curves for the four series experiments summarized in Table 4.1 are presented in Figure 4.2. In all cases, the concave negative correlations between *ASAR* and SEC^{-1}, which are characteristic of the kinetics-energetics tradeoff, can be observed. In general, an operation that leads to both high *ASAR* and SEC^{-1} (i.e. toward the upper right of the figures) is preferred. However, practical operations are governed by the tradeoff between *ASAR* and SEC^{-1}, and thus have to be optimized within such a constraint.

Table 4.2 Parameters used in the MCDI transport model

Symbols	Description	Value	
		PACMM	FM 10K
p_{sp}	Spacer porosity	$0.5^{(*1)}$	
p_{ma}	Electrode macroporosity	$0.43^{(*2)}$	
p_{mi}	Electrode microporosity	0.4	0.25
L_{elec}	Electrode thickness (μm)	290	350
L_{sp}	Space thickness (μm)	250	
A	Electrode area (cm^2)	33.75	
D_e	Effective ion diffusion coefficient ($cm^2\ s^{-1}$)	$1.68\times10^{-5(*3)}$	
D_{mem}	Ion diffusion coefficient in the membrane ($cm^2\ s^{-1}$)	$1.12\times10^{-5(*3)}$	
R	Specific electrode resistance (Ω mmol cm^{-1})	$1.2^{(*3)}$	2
ESR	Equivalent series resistance (Ω)	9.5	14
$C_{st,vol}$	Stern capacitance (F mL^{-1})	$160^{(*2)}$	100
X	Fixed ion exchange membrane charge density (mmol mL^{-1})	$3^{(*4)}$	

Parameter references: *1) Ref. [43]; *2) Ref. [100]; *3) Ref. [71]; *4) Ref. [11]

Figure 4.2A shows that attaining a lower diluted water concentration, c_D, shifted the tradeoff curves towards the left, i.e., the operations become systematically less favorable. Specifically, when the MCDI system is operated to remove more salt from a given volume (28.5 mL) of a given feed water (20 mM), either the process became slower, as reflected by a lower *ASAR*, if the energy efficiency was maintained constant; or the process became less energy efficient, as quantified by a lower SEC^{-1}, if the mass transfer rate were maintained constant. This shift of the tradeoff curve has two mechanistic contributions. First, reducing a feed solution of a

given concentration, c_0, to different diluted water concentrations, c_D, results in different underlying separations. The specific Gibbs free energy of separation, which is the theoretical minimum energy required to achieve separation in a thermodynamically reversible manner, is higher if the difference between c_0 and c_D is larger [29, 82]. Perhaps more importantly, the lower c_D also leads to a lower average ionic conductivity in the spacer channel, thereby increasing the overall ionic resistance of the system [100]. These two effects both increased the *SEC* at a given mass transfer kinetic rate and thus shift the tradeoff curve toward the unfavorable direction.

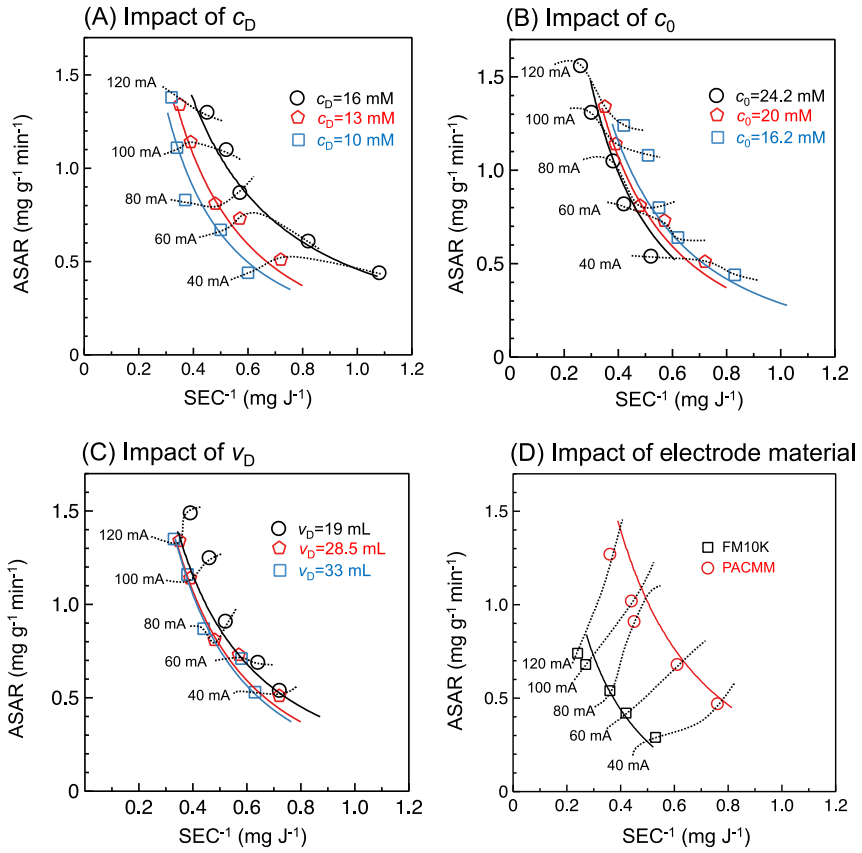

Figure 4.2 Experimental and theoretical results of *ASAR* vs. *SEC*$^{-1}$ curves for different c_D (A), c_0 (B), v_D(C), and electrode materials (D). The open symbols are experimental data and the solid curves are simulated results. The dotted curves connect the experimental results that were obtained using the same current.

In the second series of experiments, c_D was maintained at 13 mM whereas c_0 increased from 16.2 mM to 24.2 mM. Increasing c_0 has a similar qualitative impact as decreasing c_D, but to a less extent. The two effects that both increase the SEC when c_D is reduced, as discussed in Figure 4.2A, act against each other when c_0 is increased. On the one hand, increasing c_0 results in a higher specific Gibbs free energy of separation. On the other hand, a higher c_0 also reduces the overall ionic resistance of the spacer channel, especially near the cell entrance. The shift of the "*ASAR* vs. SEC^{-1}" curve in response to changing c_0, as shown in Figure 4.2B, suggests that the first effect slightly outcompeted the second effect.

When c_0 and c_D are both specified, increasing the diluted water volume per charging half-cycle, v_D, entails storing more ions in the micropores of the electrode. Consequently, the MCDI stack has to be charged to a higher voltage to generate a higher Donnan potential, according to the modified Donnan theory employed in the MCDI transport model. For this reason, an MCDI system with a higher v_D should theoretically consume more energy as the average cell voltage is higher yet the current is maintained constant. Both experimental and simulated results in Fig 2C support this hypothesis, but the impact is relatively insignificant: increasing v_D from 19 mL to 33 mL only resulted in a small shift of the "*ASAR* vs. SEC^{-1}" curve, which was also confirmed by the results simulated from the MCDI transport model.

The electrode materials used in the MCDI stack seems to have very significant impact on the position of the tradeoff curve. Figure 4.2D shows that PACMM electrode was appreciably better than the FM10K carbon cloth electrode. With the PACMM electrode, the MCDI system consumed far less energy to achieve a given ASAR or attained much faster salt removal with a given level of energy consumption. The better performance of the PACMM electrode over that of FM10K electrode can be explained by the significantly lower electrode resistance and higher microporosity as suggested by the fitting parameters for the MCDI transport model (Table 2). It is worth mentioning that the MCDI stacks with both FM 10K and PACMM electrodes yielded similarly high charge efficiency—a parameter often employed to gauge the energy efficiency of CDI processes in general. Therefore, the "*ASAR* vs. SEC^{-1}" curves provide valuable information regarding the performance of the CDI system that neither charge efficiency nor SAC can fully capture.

4.5. Practical Implications for System Design

The tradeoff between kinetic and energetic efficiencies is universal, intrinsic, and important for all desalination processes. Regardless of the technological platforms, more energy is always required to achieve a faster process that generates more entropy [26, 144]. Indeed, the most energy efficient process is a thermodynamically reversible process that is infinitely slow and generates no entropy [80]. While the thermodynamic principle behind such a tradeoff may seem straightforward and well-known, quantifying this tradeoff is important for optimizing system design and operation, which will be illustrated below.

Imagine building a brackish water desalination plant based on MCDI for a certain community. The feed water and diluted water concentrations are determined by the feed water quality and the target treated water quality, respectively. The water flowrate of MCDI system, Q, is determined by the target service capacity of the desalination plant, i.e., the volume of water to be produced per day. If c_0, c_D and Q are all specified, the required total salt removal rate of the plant (unit: kg min^{-1}) is simply $Q(c_0 - c_D)$. With simple algebraic conversions, the tradeoff curve established in this study, which is more fundamental to an MCDI process, can be translated to an equivalent tradeoff curve for more practical optimization (Figure 4.3). Specifically, the electrode mass needed, M_e, can be calculated as

$$M_e = \frac{Q(c_0 - c_D)}{ASAR} \tag{4.4}$$

The practically more relevant specific energy consumption (denoted as SEC^*), defined as energy consumption per volume of product water treated, is simply

$$SEC^* = SEC(c_0 - c_D) \tag{4.5}$$

To illustrate, let us consider designing an MCDI system for reducing the brackish water from a salinity of c_0=20 mM to c_D=10 mM at a service capacity of 100,000 GPD (equivalent to 263 L min^{-1}). For a given electrode material (e.g. PACMM), we can conduct MCDI experiments varying applied current and flow rate simultaneously to maintain a constant c_D of 10 mM, which yields a set of data in the form of "$ASAR$ vs. SEC^{-1}" as presented in Figure 4.2A. Because the target service capacity is essentially the water flowrate of the MCDI system to be design (Q), we can employ equations 4.3 and 5.4 to translate the more fundamental "$ASAR$ vs. SEC^{-1}" curve (Figure 4.3A) into a "M_e vs SEC^*" curve (Figure 4.3B) that allows more straightforward interpretation.

Figure 4.3B suggests that, to achieve the target desalination defined by c_0, c_D and Q, one can either operate at a low current density (0.30 mA cm^{-2}) to reduce energy consumption (0.27 kWh m^{-3}) at the cost of using significantly more electrode material (420 kg), or operate at a high current density (0.89 mA cm^{-2}) to reduce electrode mass (134 kg) at the cost of higher energy consumption (0.51 kW m^{-3}). The electrode mass, which represents the scale of the MCDI system, has a large impact on the capital cost of the system. Not only that the electrode itself comprises a significant fraction of the capital cost, but the costs of other components, including ion exchange membranes, current collectors and spacer, all scale with the electrode mass. To reduce the capital cost, one can reduce the electrode mass by enhancing *ASAR* via increasing the current density, which, however, inevitably leads to a lower SEC^{-1} (or higher *SEC*) that has a significant impact on the operation cost.

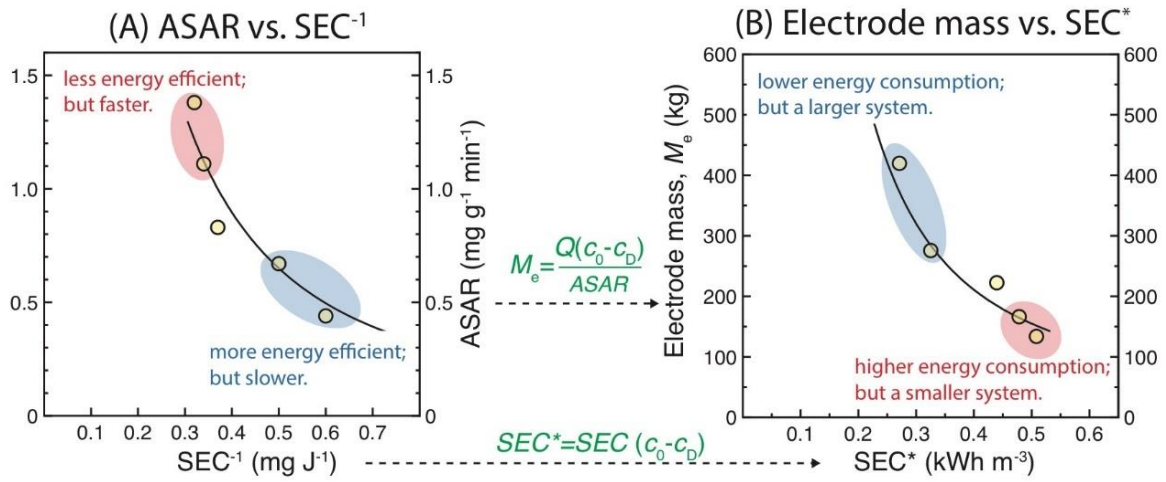

Figure 4.3 Illustration of how an *ASAR* vs. SEC^{-1} tradeoff curve (A) can be translated to represent the more practical tradeoff between the scale of an MCDI system and energy consumption (B). In this scenario, c_0 is 20 mM, c_D is 10 mM, and the electode material is PACMM. The treatment capacity of the system is 100,000 gallon per day (~263 L min^{-1}). The data on Figure 4.3A are part of the data presented in Figure 4.2A.

The analysis above suggests that the fundamental tradeoff between *ASAR* and SEC^{-1} eventually becomes the practical tradeoff between capital and operating costs, and that optimizing

the system design and operation comes down to selecting the optimal applied current density. Conducting such an optimization is beyond the scope of this paper as it involves many practical cost considerations and assumptions. In addition, other practical factors, such as different energy cost for pumping water through the MCDI stack at different flowrates should also be considered. However, the framework presented here highlights the importance of quantifying the tradeoff between energetic and kinetic efficiencies in designing a cost-effective MCDI system for real world applications.

Lastly, the tradeoff between *ASAR* and SEC^{-1}, when established using the same operating conditions (i.e., c_0, c_D, and v_D), can also be utilized to gauge the performance of the electrode material, or more broadly, of the CDI or MCDI cell stacks. Experimental results in Figure 4.2D have already shown that we can compare the quality of the electrode simply by comparing the positions of their "*ASAR* vs. SEC^{-1}" tradeoff curves as long as they do not intersect. The kinetics-energetics tradeoff curve provides different information from the CDI Ragone chart, even though the CDI Ragone chart can also be constructed using the same sets of data. The kinetics-energetics tradeoff curve captures the two most critical performance factors of an MCDI process, informing how fast the salt is removed, how much energy the process consumes, and the relationship between the two.

4.6. Conclusions

By careful and simultaneous control of the current and flowrate in MCDI with constant current operation, we managed to achieve identical separation with different currents and quantitatively demonstrate the intrinsic tradeoff between energetic and kinetic efficiencies. Faster ion removal inevitably consumes more energy, and vice versa. This tradeoff between kinetic and energetic efficiencies captures the two of the important aspects in evaluating MCDI or any desalination technology, and has significant practical implications. This tradeoff can be translated to the tradeoff between capital and operating costs, and can thus be employed for optimizing the design and operation of MCDI system. The *ASAR* and SEC^{-1} curves, reflecting the kinetic-energetic tradeoff, can also be utilized for assessing and comparing the performance of MCDI processes with different materials, designs, and configurations.

CHAPTER 5

COMPARING CONSTANT VOLTAGE AND CONSTANG CURRENT CHARGING METHOD IN CAPACITIVE DEIONIZION

This chapter has been published in the journal *Environmental Science & Technology* as part of the following peer-reviewed manuscript: Wang L., Lin S., Membrane capacitive deionization with constant current vs. constant voltage charging: Which is better. Environmental Science & Technology. **52** (2018). p. 4051-4060. doi:10.1021/acs.est.7b06064

5.1. Overview

Capacitive deionization (CDI) is an emerging technology for water desalination by the means of adsorbing ions in charged electrodes.[1] Compared to existing desalination technologies such as thermal distillation and reverse osmosis, CDI has several technological features, including the capability of desalinating low-to-moderate salinity feed water with low energy consumption,[8, 9] flexibly tailorable effluent salinity,[11] and the compatibility with intermittent operation.[17] These advantages render CDI a promising technology for desalinating brackish water with low-to-moderate feed salinity, especially in the context of off-grid and on-demand desalination powered by renewable energy.[4, 126]

Over the past decades, CDI has received extensive academic and industrial interest and experienced a significant growth in research and development. Advances have been made in multiple aspects, including developing high-performance electrodes,[50, 134, 135, 145, 146] modeling dynamic ion transport in CDI electrodes,[10, 73, 147, 148] designing novel cell stack structures that enhance performance or enable continuous operation,[16, 17, 63, 64, 81] and elucidating the impacts of the operating modes and electrode properties on CDI performance.[11, 61, 65, 68, 89, 104, 118] Of these technological advancements, membrane CDI, or MCDI, i.e., CDI coupled with ion exchange membranes(IEMs), received particular attention due to its higher charge efficiency and better energy efficiency.[10, 149]

The two most common charging modes in CDI/MCDI are constant voltage (CV) and constant current (CC).[1] In CV charging, a constant voltage is applied across the CDI/MCDI cell

throughout the charging stage. The electrical current through the cell and the kinetic rate for ion removal spike immediately after charging starts, and then decrease as the electrodes become increasingly saturated with the adsorbed ions. In CC charging, the cell voltage is automatically increased to maintain a constant current during the charging stage. Since ion transfer kinetic rate is roughly proportional to the charging current, ions are also removed in a constant rate during CC charging.

Both CC and CV charging have been heavily studied and proven viable in CDI/MCDI. Several previous studies compared CDI/MCDI performance with the two charging modes, the results of which are summarized in Table 1. With only one exception, all studies suggest that CC charging consumes less energy than CV charging to remove the same amount of salt, and is thus a more energy efficient charging mode. In addition, one study found that MCDI with CV operation adsorbs more salt per charging stage than that with CC operation when the charging voltage in CV equals the final charging voltage in CC.[86, 150] Interestingly, however, the study by Zhao et.al. suggested that there exist subtle differences between the energy consumption with CC and CV charging, and that such differences depend on the charging time, the feed salinity, and the levels of the applied voltage in CV operation and current in CC operation.[11] It is worth noting that the experimental protocols of these studies are all different, thus the interpretation of the conclusions in Table 5.1 has to be practiced with caution regarding their specific experimental protocols.

Answering the question of whether CC or CV is a better charging mode for MCDI requires the definition of "better". From a practical operation perspective, a better charging is one that either consumes less energy at the same ion removal rate, or removes ion faster with the same energy consumption, or even consumes less energy and removes ion faster. This performance evaluation metric composed of the energetic and kinetic efficiencies can be directly employed to evaluate the capital cost, which is related to the footprint and material cost of the system, and the operating cost, which is strongly dependent on the energy cost of desalination.[45, 151] In this sense, the widely investigated parameter, specific adsorption capacity (SAC) in the charging stage, is only of indirect significance that would ultimately be integrated to the kinetic and/or energetic efficiencies.

Table 5.1 Summary of previous studies that compared CC and CV operations

CDI Type	Experimental Protocol	Conclusions	Ref
MCDI	• CV charging voltage equals CC cutoff voltage (0.4 to 1.4 V) • CC with fixed current density • Identical charging time	• CC more energy efficient • CV adsorbs more salt	150
CDI	• CV charging voltage and CC cutoff voltage both @ 1.2V • CC with different current densities • Equal total charge transferred or total amount of salt adsorbed	• CC more energy efficient	86
CDI	• CV charging voltage equals CC cutoff voltage (1.2V)	• CC more energy efficient	98
Flow-through CDI	• CV charging voltage @ 1V with different charging time • Equal total charge transferred • Identical charging time	• CC more energy efficient	137
MCDI & CDI	• CV charging voltage @ 1.2V with a charging time of 300s • CC charging current @ 1.0 A* and cutoff voltage @ 1.6V • Various feed salinity	• MCDI more energy efficient than CDI • No conclusive advantage in energy efficiency for CC or CV	11

[#] All CDI or MCDI processes are of flow-by configuration unless specified otherwise.

* the corresponding current density was 38.4 A m^{-2}.

Following the rationale above, a performance evaluation framework has been recently developed to quantify the tradeoff between energetic and kinetic efficiencies using tradeoff curves that relate the inverse of specific energy consumption, SEC^{-1} (i.e. amount of salt per unit energy consumed), and the average salt adsorption rate, *ASAR* (i.e. amount of salt adsorbed per mass of electrode per time).[151] Increasing the *ASAR*, which quantifies the kinetic efficiency, along the "SEC^{-1} vs. *ASAR*" tradeoff curve, reduces the SEC^{-1}, which reflects the energetic efficiency. Each point on a "SEC^{-1} vs. *ASAR*" tradeoff curve represents a charging operation defined by the selection of three parameters, including the applied voltage in a CV operation or the applied current in a CC operation, the flowrate of the flow stream through the system, and the duration of the charging

stage. These parameters are carefully adjusted so that all points on a "*SEC*$^{-1}$ vs. *ASAR*" tradeoff curve correspond to an identical "target adsorption". Different charging operations are considered to achieve the same "target adsorption" if the dilute solution volume, v_D, the initial salinity, c_0, and the average dilute solution salinity, $\bar{c}_D$, are maintained the same in these operations. It is of critical importance to ensure that all points on one "*SEC*$^{-1}$ vs. *ASAR*" tradeoff curve result in the same target adsorption because different target adsorption intrinsically, regardless of how they are achieved, require different minimum energy to charge the electrode to an end state characterized by the final voltage and charge density.[82]

Similarly, a rational comparison between CC and CV charging also requires that the two operations compared achieve the same target adsorption defined by v_D, c_0, and $\bar{c}_D$. Most previous studies comparing CC and CV charging did not make the deliberate effort to ensure the target adsorptions the two operations achieve are identical, except for a recent study in which the charging duration and total transferred charge for both CC and CV charging were maintained the same[31]. To compare the two charging modes systematically, two series of experiments can be conducted to construct two "*SEC*$^{-1}$ vs. *ASAR*" tradeoff curves, one for CC charging and the other for CV charging, both resulting in an identical target adsorption. Theoretically, the intersection between two tradeoff curves implies the existence of an *ASAR* above which one charging mode is better and below which the other charging mode outperforms. Otherwise, one can conclude that a charging mode is consistently superior to the other, at least for achieving a specific target adsorption. This is the theoretical framework we will employ to systematically compare CC and CV charging in MCDI.

In this study, we employ both experimental and simulation approaches to investigate the kinetic and energetic efficiencies of MCDI with CV and CC charging. The performance comparison between these two charging modes is carried out by comparing the relative positions of their tradeoff curves that relate the kinetic and energetic efficiencies of a series of operations resulting in the same target adsorption. We also evaluate the equilibrium voltage and excess voltage over a charging stage, from which we calculate the excess energy to elucidate why one charging mode outperforms the other. We focus our comparing on the charging (or adsorption) stage in this study, instead of the full charging-discharge MCDI cycle because the flexibility of choosing different discharge modes and kinetic rates for a given charging stage complicates the comparison of a full cycle and renders the analysis more arbitrary and less insightful. Our primary

goal is to determine if there exists one charging mode that universally outperforms other, and if not, to identify factors affect their relative performance.

5.2. Materials and Methods

5.2.1. MCDI stack

The MCDI stack design has been described in our previous publication and its details are given in Supporting Information.[151] Briefly, four electrodes/membranes/spacer assemblies were firmly compacted into a MCDI stack in an acrylic housing. Each assembly consisted of two porous carbon electrodes (PACMM 203, Materials & Methods LLC, Irvine, CA) with a thickness of δ_e=280 µm, an anion exchange membrane (Neosepta AMX, Tokuyama Co., Japan) with a thickness of δ_{amem}=140 µm, a cation exchange membrane (Neosepta CMX, Tokuyama Co., Japan) with a thickness of δ_{cmem}=170 µm, and a glass fiber spacer (Whatman) with a thickness of δ_{sp}=250 µm. Each assembly was cut into a 6×6 cm^2 square with a 1.5×1.5 cm^2 square hole at the center. The total mass of the 4 pairs of electrodes was 3.06 g. The feed solution enters from periphery of the stack, flows along the spacer channels, and exits through the square cutout in the center.

5.2.2. Experimental methods

In all experiments, the feed solution was 20mM NaCl solution. The feed reservoir was constantly purged with nitrogen to remove dissolved oxygen for minimizing long-term electrode oxidation. The feed solution was peristaltically pumped through the MCDI stack, and the effluent of the MCDI stack was sent back to the feed reservoir. The effluent conductivity was measured using an inline conductivity meter (isoPod EP357, eDAQ, Australia) installed right at the exit of the MCDI cell, and was further converted to salt concentration based on a pre-established calibration curve. Both CV and CC charging modes were applied using a potentiostat (SP 150, Bio-Logic, France) that also measured the real-time electrical current in the CV mode and the real-time cell voltage in the CC mode.

5.2.3. Identical target adsorption and kinetic rate

Following the rationale presented in the introduction, the fair comparison of the performance between two CDI/MCDI systems, either with different electrode materials, configurations, or operation modes, entails that the two operations achieve identical target adsorption at the same kinetic rate. This rationale was implemented throughout this study for comparing CC and CV charging. Specifically, we carefully adjusted the experimental conditions to make sure that the *average dilute solution salinity,* $\bar{c}_D$, and the *dilute solution volume,* v_D, were kept constant in MCDI experiments with both CC and CV charging. (c_0 was also constant in all cases). To achieve identical target adsorption with both CC and CV modes, we first run MCDI experiments with CV charging to obtain $\bar{c}_D$, and then adjusted the current in CC charging to achieve a mean effluent concentration that is equal to the $\bar{c}_D$ in CV charging. The first series of experiments in this study were conducted to achieve a $\bar{c}_D$ of 14.4 mM (from c_0=20 mM), for a dilute solution volume of v_D=100 mL. Other target adsorptions were also investigated, with their detailed parameters given in discussion. The operating parameters for the experiments, including flowrate and charging duration, applied voltage in CV charging, and applied current in CC charging are all reported in Table S5.1. The MCDI cell was operated for several cycles to allow the electrode to reach dynamic adsorption-desorption equilibrium. All charge/discharge cycles selected for data analysis were chosen from a series of at least three consecutive full cycles that yield very similar time series of effluent salinity. The actual $\bar{c}_D$ with different experimental conditions, which are supposed to be around 14.4 mM, are reported in Table S5.2.

In addition to identical target adsorption, another requirement for direct comparison of the energy efficiency between two charging modes is that they remove salts at the same kinetic rate, which is typically quantified by *ASAR*. Because the total amount of salt removed in the adsorption stage is $(c_0 - \bar{c}_D)v_D$, and also because $\bar{c}_D$ and v_D are both controlled to be the same for achieving identical target adsorption, the total amount of salt removed in the adsorption stage is the same for the two charging modes. Therefore, an equal *ASAR* also requires that the same charging duration and cross flowrate are maintained for both CC and CV charging. The detailed conditions for different sets of experiments are summarized in Appendix Table C1.

5.2.4. Data analysis

For CV charging, the effluent salinity, c_D, varies over the entire charging stage. Even for CC operation in which c_D is supposed to be constant, c_D also varies briefly at the beginning of the charging stage before becoming stable, because the effluent exiting the cell right after the charging starts is exposed to the applied electric field for a duration less than hydraulic contact time. Because of the temporal variability of c_D, the average effluent salinity for an MCDI charging stage, $\bar{c}_D$, is estimated for each adsorption mode using equation 5.1:

$$\bar{c}_D = \frac{\int_0^{t_C} c_D(t)dt}{t_C} \tag{5.1}$$

where $c_D(t)$ is the real-time effluent salinity and $\mathrm{t_C}$ is the time of the charging duration.

The energy efficiency of an MCDI process has been traditionally quantified using specific energy consumption, *SEC*, defined as the energy consumed to remove a unit mole of NaCl:

$$SEC = \frac{\int_0^{t_C} I(t)V(t)dt}{Q\int_0^{t_C}(c_0 - c_D(t))dt} \tag{5.2}$$

where $I(t)$ is the electrical current, $V(t)$ is the cell voltage, Q is the flowrate, and c_0 is the feed concentration. Alternatively, we can also quantify energy efficiency of an MCDI process using the inverse of *SEC*, i.e. SEC^{-1}. SEC^{-1}, being the mass of salt removed with a unit energy input, directly reflects how efficiently energy is utilized for salt removal. Notably, SEC^{-1} is essentially the same as energy-normalized adsorbed salt (*ENAS*) that was used in a previous study.[101] We use SEC^{-1} instead of *SEC* to present our data in this study because the negative correlation between SEC^{-1} and kinetic rate of salt removal better reflects the intrinsic tradeoff between energetic and kinetic efficiencies.

Finally, the kinetic efficiency of an MCDI process is quantified by *ASAR* which can be evaluated using equation 5.3:

$$ASAR = \frac{Q\int_0^{t_C}(c_0 - c_D(t))dt}{\theta_e t_C} \tag{5.3}$$

where θ_e represents either the mass or the apparent area of the electrode. While the definition of *ASAR* based on electrode mass is most commonly used in literature, defining *ASAR* based on apparent area of electrode and IEM assembly may be more informative in practical system design because it better reflects the demand for both electrode and IEM. Therefore, both definitions of *ASAR* will be reported in this study.

The comparison between two MCDI charging operations can be performed by simultaneously comparing their SEC^{-1} and *ASAR*, provided that they achieve the same target adsorption. For example, if two charging operations are of the same SEC^{-1}, i.e., they are equally energy efficient, the one with a higher *ASAR*, i.e., the one that removes salt faster, can be considered more kinetically efficient and thus "better". Similarly, if two operations are of the same *ASAR*, the one with a higher SEC^{-1} is considered to be "better" because it is more energy efficient. If the"SEC^{-1} vs. *ASAR*" tradeoff curve of one charging mode is completely above that of the other charging mode throughout the range of *ASAR* they overlap, we can conclude the charging mode with a higher tradeoff curve to be more efficient in general.

5.3. Dynamic Ion Transport Model

We employed a dynamic ion transport model to extract parameters for our MCDI system by fitting experimental data and using such a model to conduct more comprehensive theoretical analysis comparing CC and CV charging over a larger range of operating conditions. This model considers ion transport across ion exchange membranes (IEMs) and within the macropores of the carbon electrodes, as well as the equilibrium ion distribution at the interfaces between the spacer and IEMs, between IEMs and macropores of the carbon electrode, and between micropores and macropores of the carbon electrodes.[10, 71] The porous carbon electrodes are assumed to be inherently charge-free, and are charged only when a nonzero external voltage is applied.[37, 82]

With an applied external voltage, a Donnan potential is established between the micropores and macropores according to the modified Donnan (mD) model.[10] Similarly, Donnan potentials also exist at the IEMs/spacer and IEMs/electrode interfaces.[138] Additional potential drops across an MCDI half-cell include the Stern potential between the electronic and ionic charges, potential drops due to ion transport resistance in the IEMs and spacer, electronic resistance in the carbon electrodes, and contact resistances at various interfaces (primarily at the electrode/current collector interfaces[69]). These parasitic potential drops, together with the Donnan and Stern potentials, comprise the cell voltage. The ion transport kinetics in the stack is described by the Nernst-Planck equation. In the direction of the water flow along the spacer, the MCDI cell is modeled as a continuous stirred-tank reactor (CSTR), i.e., we do not consider the concentration gradient in the

flow direction.[140] This dynamic MCDI ion transport model was numerically solved to predict the time-dependent effluent salinity and the cell current (in CV charging) or cell voltage (in CC charging), which were then compared with experimental results and to generate performance parameters such as *ASAR* and SEC^{-1}. The details of the model derivation and the parameter selection are provided in Supporting Information.

5.4. Results and Discussion

5.4.1. Experimental results and model validation

In the first series, five pairs of MCDI experiments were conducted for performance comparison between CV and CC charging. Each pair comprises one MCDI experiment with CV charging and the other with CC charging, respectively. All five pairs of MCDI experiments achieved a very similar target adsorption, characterized by a c_0 of 20 mM, a $\bar{c}_D$ of 14.4 mM, and a v_D of 100 ml. Figure 5.1 presents the experimental and modeling results for one pair of experiments in which the applied voltage in CV operation was 1.2V and the electrical current in CC operation was 92 mA. The flow rate for both operations was 10 mL min^{-1}. For both CV (Figure 5.1A and 5.1B) and CC (Figure 5.1C and 5.1D) charging, a dynamic MCDI model with an identical set of parameters (Table S5.3) fits the experimental results remarkably well. The same set of parameters, which are theoretically dependent only on the properties of the MCDI system but not on the operating conditions, will be applied for MCDI modeling in the rest of this work.

In addition to the excellent agreement between experimental and modeling results, the time dependent profiles of effluent salinity, electrical current (in CV charging), and cell voltage (in CC charging) are highly consistent with the state-of-the-art experimental results reported in literature.[7, 11] Results from Figure 5.1 also demonstrate the ability to control the operating conditions in CV and CC charging to achieve the same target adsorption at the same *ASAR*, which is the foundation for fair comparison of system performance between the two operation modes.

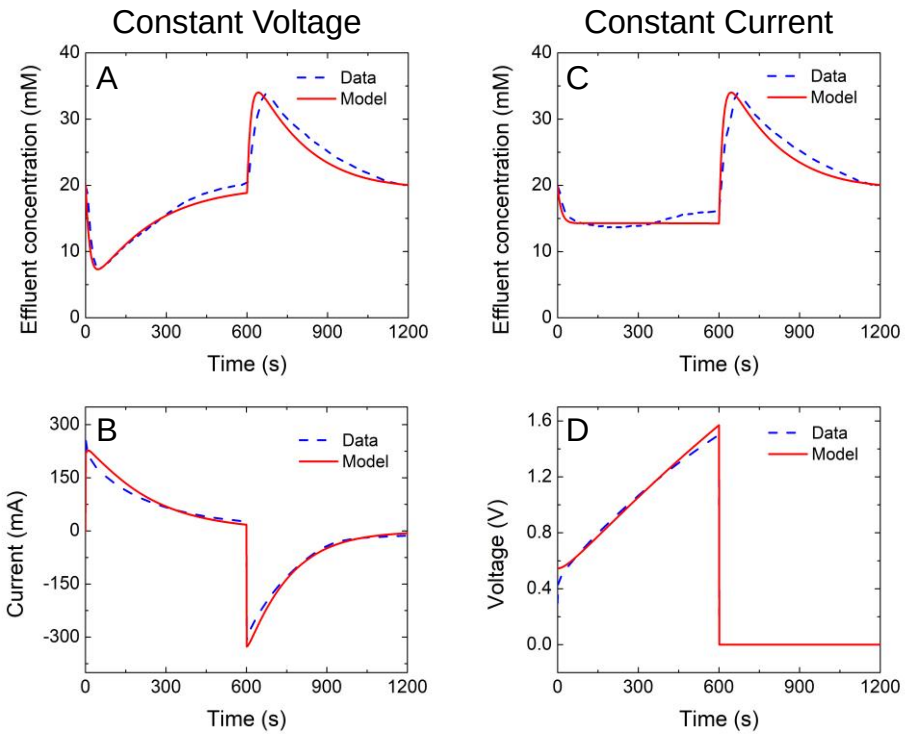

Figure 5.1 (A) effluent concentration and (B) electrical current in an MCDI process with CV charging; (C) effluent concentration and (D) cell voltage in an MCDI process with CC charging. The charging and discharge voltages for the CV operation were 1.2 V and 0 V, respectively. The electrical current in the CC operation was 92 mA. In both cases, the discharge was carried out using zero voltage.

Additional MCDI experiments similar to those shown in Figure 5.1 were performed by varying the cell voltage in CV charging, the cell current in CC charging and thus the flowrate and charging/discharging duration, all controlled to yield the same target adsorption. Their energy efficiency, quantified by SEC^{-1}, and kinetic efficiency, quantified by *ASAR*, varied as a function of the driving force, quantified by either the cell voltage or cell current (Figure 5.2). The ranges of cell voltage in CV operation (1.16V to 1.30V) and cell current in CC operation (74 mA to 135 mA) were chosen such that both operation modes yield a similar range of *ASAR*.

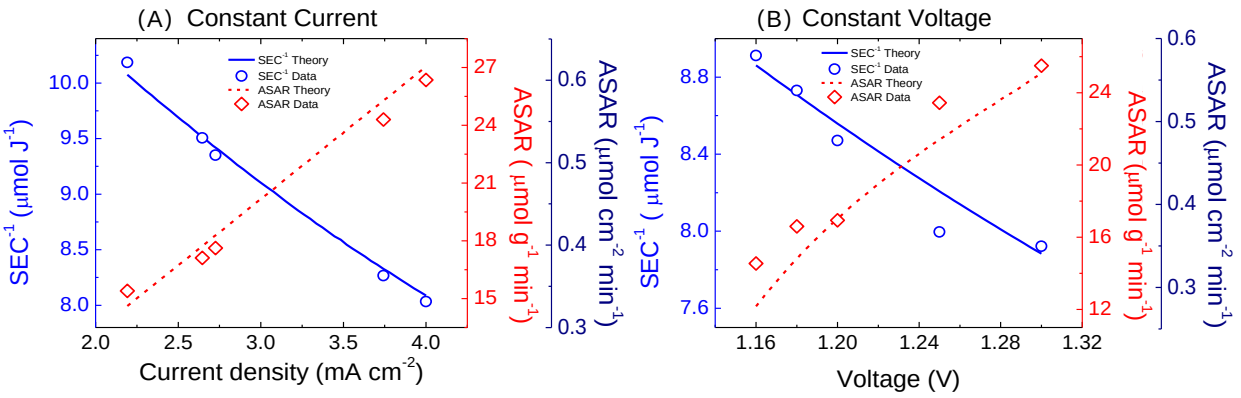

Figure 5.2 *SEC*$^{-1}$ (blue, left y-axis) and *ASAR* (right y-axis) for charging stage as functions of cell voltage in CV mode (A) and in CC mode (B). The open circles are experimental data, whereas the dash and solid curves (lines) are results simulated from the dynamic ion transport model with a single set of parameters listed in Table S5.3.

The simulated results from the dynamic ion transport model, given in Figure 5.2 as solid and dash curves, fit the experimental data reasonably well for both CV and CC chagrining. The very good fitting, demonstrated by the high coefficients of determination (Table C4), suggests a remarkable predicting power of the MCDI ion transport model, especially given that these solid curves are not established by fitting the experimental data but rather completely simulated from the dynamic ion transport model using one single set of system parameters. For both charging modes, *SEC*$^{-1}$ negatively correlates with the cell voltage or current, whereas the *ASAR* positively correlates with the cell voltage or current.

5.4.2. Comparing CC and CV charging

The results in Figure 2 are used to construct the *SEC*$^{-1}$ vs. *ASAR* tradeoff curves to reflect the intrinsic tradeoff between energetic and kinetic efficiencies in MCDI (Figure 5.3). These tradeoff curves indicate that one can tune MCDI operation by increasing either the charging voltage in CV or the electrical current in CC charging to achieve a higher kinetic efficiency (*ASAR*) but at the cost of lower energy efficiency (*SEC*$^{-1}$), or in other words, higher energy consumption

(*SEC*). We want to reemphasize that all experimental and simulated data points in Figure 5.3 result in the same target adsorption, which is critically important for comparison within and between the tradeoff curves to be fully meaningful.

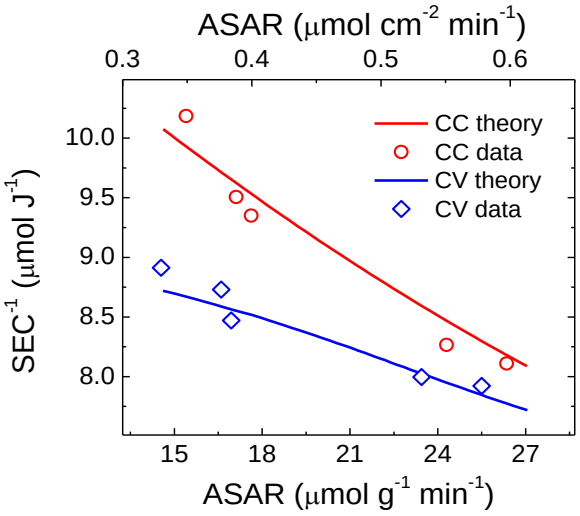

Figure 5.3 SEC^{-1} vs. *ASAR* for the charging stage in MCDI with CC (red) and CV (blue) charging. These tradeoff curves are constructed using the data shown on Figure 5.2. The open circles are experimental data, whereas the solid curves (lines) are results simulated from the dynamic ion transport model. Each data point on a CV tradeoff curve is obtained with a unique cell voltage, as each point on a CC tradeoff curve is obtained with a unique electrical current.

Comparing the two SEC^{-1} vs. *ASAR* curves in Figure 5.3 suggests that CC charging is superior to CV charging—at least for this specific target adsorption and within this range of kinetic rate. Such superiority can be interpreted from two different angles. First, if both CC and CV MCDI processes are operated at the same *ASAR*, CC charging is more energy efficient than CV charging as it removes more salt with the same amount of energy. Alternatively, if the MCDI process with the two charging modes are controlled to achieve equal energy efficiency, or SEC^{-1}, then CC charging removes salts appreciably faster than CV charging. Because the two tradeoff curves do not intersect, we can conclude that CC charging is more efficient than CV charging, for this target adsorption and within this *ASAR* range.

5.4.3. Excess voltage and excess energy

To elucidate why CC charging outperforms CV charging in the above example, here we introduce two important concepts: excess voltage and excess energy. Excess voltage, V_{ex}, is the difference between the actual cell voltage, V_{cell}, and the equilibrium cell voltage, V_{eq}:

$$V_{ex} = V_{cell} - V_{eq} \tag{5.4}$$

The equilibrium cell voltage is the imaginary cell voltage at which the system, with the ion distribution between the bulk solution and electrode micropores at a given moment, *t*, is in a thermodynamic equilibrium. In other words, if at any given point of a CDI/MCDI process, V_{cell} is adjusted to be equal to V_{eq}, the ion distribution at that point will be indefinitely maintained and no net ion transport into or out of the double layer in the micropores will occur. With a modified Donnan model,[82] V_{eq} is simply the sum of Donnan potentials, ΔV_D, Stern potentials, ΔV_{St}, and the Donan potentials across the two interfaces of IEMs (i.e. membrane/spacer and membrane/electrode interfaces). The equilibrium voltage is independent of any ion or electronic transport resistance, because these resistances are irrelevant without charge transport at a finite rate. Therefore, V_{ex} can be interpreted as the degree of deviation of the system from equilibrium, or as the driving force for ion transport. On the other hand, $V_{ex}(t)$ also equals the product of the electrical current, $I(t)$, and the total cell resistance, $R(t)$, at time, t. Therefore, the transient total system resistance $R(t)$ can be conveniently probed by evaluating $V_{ex}(t)$. However, resolving the different contributions to the total system resistance has to be achieved using more complicated equivalent circuit models.[137]

The distribution of V_{ex} as a function of charging time in a CV operation differs drastically from that in a CC operation (Figure 5.4). In CC charging, V_{ex} is more evenly distributed throughout the charging stage, both temporally (Figure 5.4B) and per unit amount of charge transferred (Figure 5.4D). By contrast, V_{ex} in CV charging decreases over time from V_{cell} to approach zero, both temporally (Figure 5.4A) and per unit amount of charge transferred (Figure 5.4C). In CV charging, the "V_{ex} vs. charge transferred" curve deviates significantly from the "V_{ex} vs. time" because the current was much higher at the beginning of charging. These two curves are of very similar shape in CC charging because the current is constant.

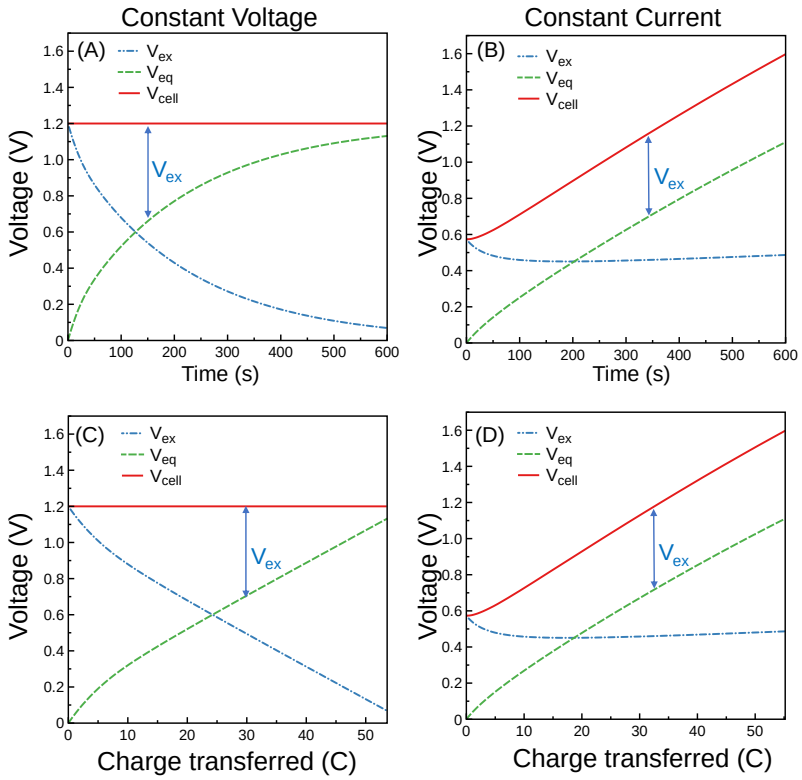

Figure 5.4 Distribution of cell voltage, V_{cell} (red solid curve), equilibrium voltage, V_{eq} (green dash curve), and excess voltage, V_{ex} (blue dash-dotted curve) over the charging stage. Figures 5.4A and 5.4B present the temporal distributions of these voltages in CV charging and CC charging, respectively. Figures 5.4C and 5.4D present the distribution of these voltages with respect to cumulative charge transferred in CV and CC charging, respectively. The excess voltage, V_{ex}, being the difference V_{cell} and V_{eq}, is also equal to the height of the shaded area. These figures are constructed using data presented in Figure 1 which were obtained from experiments in which the flowrate was 10 mL min^{-1}, charging time was 600 s and the corresponding *ASAR* was about 1 mg g^{-1} min^{-1}. Note that the total shaded area in Figures 5.4C and 5.4D quantify the excess energy, i.e., the total energy lost in the charging stage due to entropy generation.

Another concept building on V_{ex} and more directly relevant to quantifying energy loss in a CDI or MCDI process is excess energy, E_{ex}, defined as

$$E_{ex} = \int_0^{t_C} V_{ex}(t) I(t) dt = \int_0^{\sigma(t_C)} V_{ex}(\sigma) d\sigma \qquad (5.5)$$

where σ is the cumulative charge transferred and is a function of time, and $\sigma(t_C)$ is the total charge transferred in the charging stage. It can be readily shown that E_{ex} is the area of the shaded region in Figure 5.4C and 5.4D. The excess energy stands for the additional energy spent in driving the ion adsorption process to occur in a finite rate. If the process is thermodynamically reversible and thus infinitely slow, the charging process would have consumed a minimum amount of energy, namely the equilibrium adsorption energy, E_{eq}, for the charging stage:

$$E_{eq} = \int_0^{t_C} V_{eq}(t)I(t)dt = \int_0^{\sigma(t_C)} V_{eq}(\sigma)d\sigma \tag{5.6}$$

The sum of E_{ex} and E_{eq} is the actual energy spent, E_{tot}, which can be readily shown by combining equations 5.4 to 5.6:

$$E_{tot} = \int_0^{t_C} V_{cell}(t)I(t)dt = \int_0^{t_C} \left[V_{eq}(t) + V_{ex}(t)\right]I(t)dt = E_{eq} + E_{ex} \tag{5.7}$$

We can further define two ratios, one being E_{ex}/E_{eq} and the other being E_{ex}/E_{tot}, to quantify the relative amount of excess energy consumption compared to two different references. Specifically, the reference in E_{ex}/E_{eq} is the minimum amount of energy required to achieve the target adsorption but in a thermodynamically reversible manner, whereas the reference in E_{ex}/E_{tot} is the total amount of energy consumed to achieve the same target adsorption in a practical process. Graphically, E_{ex}/E_{eq} is the ratio between the shaded area and the area under the green dash curve in Figures 5.4C and 5.4D, whereas E_{ex}/E_{tot} is the ratio between the shaded area and the area under the red solid curve in the same figures.

Comparing CC and CV charging using either ratio for data in Figure 5.3 suggests that CV consumes more relative E_{ex} than CC when both operations are controlled to achieve the same target adsorption at the same ASARs (Figure 5.5E). The thermodynamic interpretation is that more entropy is generated with CV charging than with CC charging even though the kinetic rate is maintained the same. From an equivalent circuit perspective, the comparison also implies the overall resistance in CV charging is higher than that in CC charging.

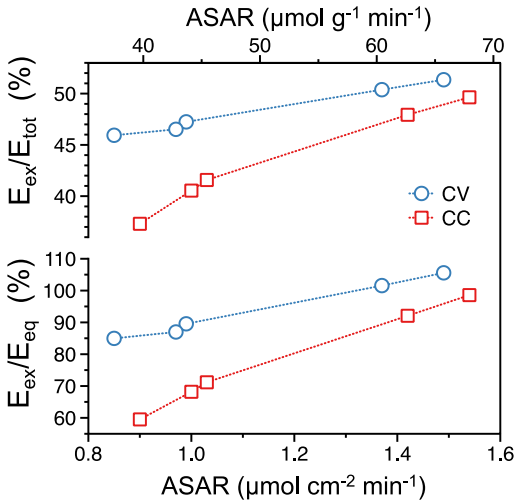

Figure 5.5 Comparison of E_{ex}/E_{eq} (top) and E_{ex}/E_{tot} (bottom) ratios between CC (red squares) and CV (blue circles) operations at different *ASAR*. This figure is constructed using the same sets of raw data used to construct Figure 5.3. The dotted lines are just for guiding the eyes.

5.4.4. Can CV mode outperforman CC mode?

In all experimentally tested and numerically simulated scenarios in the above discussion, CC charging always outperforms CV charging, as reflected by the relative positions of their "*SEC*$^{-1}$ vs. *ASAR*" tradeoff curves in Figure 5.3. This conclusion, however, is not universally true. We have conducted another series of experiments using both charging modes to achieve a different target adsorption characterized by the same feed and dilute solution concentrations (i.e. c_0=20 mM and $\bar{c}_D$=14.4 mM) but a different volume of dilute solution. Specifically, v_D in this new series of experiments was 50 mL, as compared to a v_D=100 mL as in Figures 5.2 and 5.3. The results from this series of experiments suggest that CV charging is systematically more efficient than CC charging, as evidenced by an "*SEC*$^{-1}$ vs *ASAR*" tradeoff curve for CV charging that is consistently above that for CC charging (Figure S5.2).

In addition to changing v_D, we also conducted an additional experiment to achieve a lower $\bar{c}_D$ of 10.4 mM for v_D=50 mL. To achieve such an adsorption, the cell voltage in CV was set to 1.4V and the charging process was terminated prematurely before the salt adsorption capacity of the electrodes was fully exhausted, as otherwise the high *ASAR* required was unattainable due to

prolonged CV charging without adsorbing proportionally more salt. In this set of experiments (Figure S5.3), the *ASAR* for both charging modes was 1.85 mg g^{-1} min^{-1}, whereas the SEC^{-1} for CV and CC charging were 0.46 and 0.42 mg J^{-1}, respectively, suggesting that CV charging is 9.5% more efficient than CC charging at the same kinetic rate. In addition, the E_{ex}/E_{eq} ratios for CV and CC charging were 128.8% and 145.9%, respectively, indicating that relatively less energy is spent as the driving force in a CV charging than in a CC charging to achieve the same *ASAR*.

5.4.5. Relative energetic-kinetic advantage primarily depends on the target adsorption

Up to this point, we have observed that CC and CV can both be the more efficient charging mode, and that their relative advantage in kinetic and energetic efficiencies is dependent on the target adsorption. For a more holistic comparison between CC and CV charging, we conduct additional simulations for more scenarios using parameters in Table S5.3. The dynamic ion transport model can be considered reasonably reliable, as it has been shown, in Figures 5.2 and 5.3, to be able to generate simulation results that are highly consistent with experimental measurements. In all simulations, the feed salinity was c_0=20 mM. Two different dilute solution volumes, v_D= 100 mL and v_D= 50 mL, were evaluated. With each v_D, we tried to simulate the *ASAR* vs. SEC^{-1} curves for CC and CV charging with $\bar{c}_D$ being 18 mM, 14.4 mM, and 10.4 mM, respectively.

Each tradeoff curve for CC or CV charging has an upper limit of *ASAR* due to the maximum charging voltage chosen. The maximum *ASAR* in CC charging corresponds to an operation in which V_{cell} reaches a cutoff voltage of 1.8V, whereas the maximum *ASAR* in CV charging corresponds to a maximum V_{cell} of 1.5V. These operating voltage limits are set in our simulation because practical long-term operations beyond these limits will likely cause undesirable electrode oxidation.[141] The cutoff voltage for CC charging is chosen to be higher than the maximum applied voltage in CV charging, because electrodes are exposed to high voltage in CC charging for only a relatively small fraction of the charging duration, whereas in CV charging the electrodes constantly experience the same voltage. In addition to these upper limits, there also exist lower limits of *ASAR* in CV charging. To achieve an *ASAR* below these limits, the MCDI cell has to operate at a voltage

that is too low to adsorb enough salt for achieving the specified target adsorption (detailed explanation in Supporting Information).

For v_D=100 mM (Figure 6A), CC charging consistently is consistently more efficient than CV charging for target adsorptions that reduce $\bar{c}_D$ to 18 and 14.4 mM, which is reflected by the higher "*SEC*$^{-1}$ vs. *ASAR*" tradeoff curves for CC charging than that for CV charging. When $\bar{c}_D$ is 14.4 mM, which is the target adsorption shown in Figures 5.1 and 5.2, the advantage of CC charging over CV charging diminishes with increasing *ASAR* as shown in Figure 5.3, but the two tradeoff curves do not intersect within the chosen voltage limits for both charging modes. Neither CV nor CC charging can reduce $\bar{c}_D$ to 10.4 mM within their respective chosen voltage limits, because the salt adsorption capacity of the electrodes at those voltage limits is still smaller than the required amount of salt to be removed to reach a $\bar{c}_D$ of 10.4 mM.

For target adsorptions with v_D=50 mL (Figure 5.6B), whether one charging mode is more efficient over the other is highly dependent on $\bar{c}_D$. Specifically, CC charging has is more efficient than CV charging throughout the range of possible *ASAR* when $\bar{c}_D$ is 18 mM. However, when $\bar{c}_D$ is 14.4 mM or 10.4 mM, CV charging becomes consistently better than CC charging, even though the advantage dwindles as ASAR decreases.

The direct comparison between CC and CV charging is made only when both charging modes are able to attain the same target adsorptions at the same *ASAR*. There are, however, ranges of *ASAR* in which only one of the two charging modes can achieve the target adsorptions. Regardless of v_D, CC charging can operate at a wider range of *ASAR*s than CV charging to achieve target adsorptions with a $\bar{c}_D$ of 18 mM. As a result, the ranges of *ASAR* at which CV charging can achieve the target adsorptions are subsets of the ranges of *ASAR* at which CC can achieve the same target adsorptions, as shown in Figure 6A and 6B. For target adsorptions with lower $\bar{c}_D$, CV charging can operate in a high *ASAR* range that CC charging cannot operate, because CC charging in that *ASAR* range requires the cell voltage to increase beyond the chosen cutoff voltage of 1.8V. On the other hand, CC charging can operate in a low *ASAR* range in which CV charging fails to operate, as CV charging in that *ASAR* range requires an applied voltage that is too low to achieve the target adsorption.

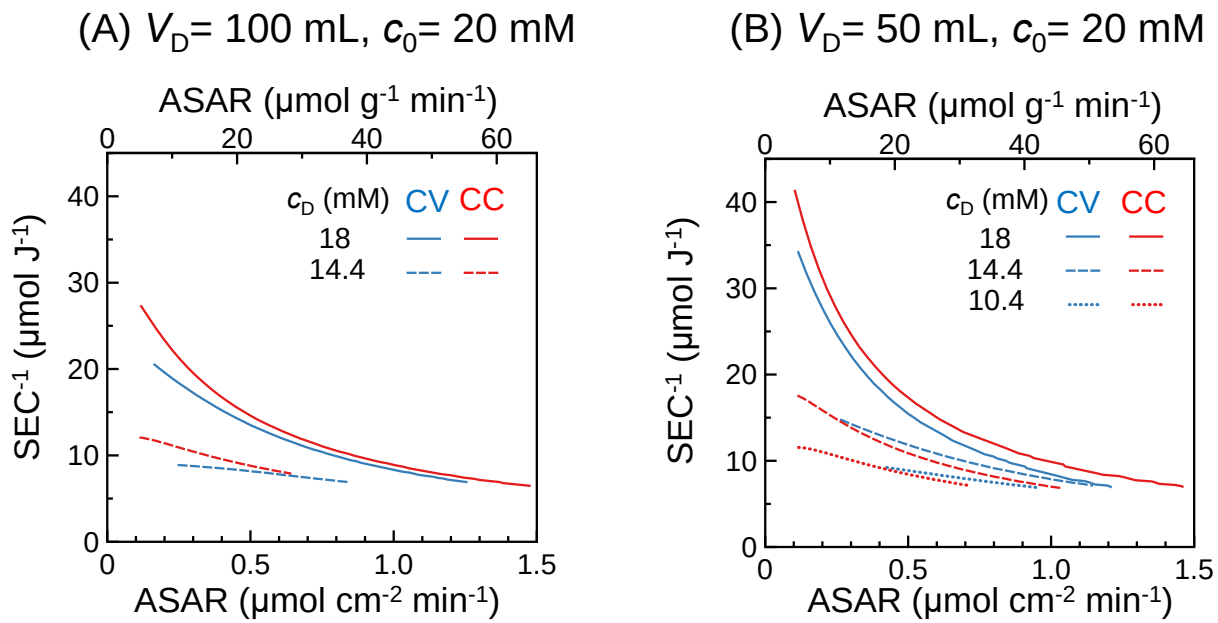

Figure 5.6 Simulated *SEC*$^{-1}$ vs. *ASAR* curves for CC (red) and CV (blue) operations with different "adsorptions" defined by different combinations of V_D, c_0, and $\bar{c}_D$. These results are simulated using the dynamic ion transport model described in Supporting Information with parameters listed in Table S3. In all simulations, the feed salinity, c_0, is 20 mM. The dilute solution volumes, i.e., the volumes of water passing through the MCDI stack in the adsorption stage, are 100 mL and 50 mL in (A) and (B), respectively. The dilute solution salinity, c_D, varies within each sub-figure. Each pair of CC and CV curves corresponds to one specific "adsorption". When simulating these data, we choose not to exceed 1.8V for CC charging and 1.5V for CV charging. These imposed constraints set the upper bounds of the *ASAR*s for CV and CC charging. The lower bounds of the *ASAR*s for CV charging result from the fact that CV charging with sufficiently low voltage to achieve *ASAR*s below these lower bounds cannot provide enough saturation adsorption capacity to achieve the target adsorption. Note that neither CV nor CC charging within the imposed voltage limits can possibly reduce the salinity of 100 mL feed solution from 20 mM to 10.4 mM, which is why no curve is shown for such a target adsorption in (A). The yellow region in (A) represents the data set presented in Figure 3, whereas the green circle in (B) represents range of data sets reported in Supporting Information.

5.5. Conclusions

The performance of CC and CV charging in an MCDI process was compared systematically using the SEC^{-1} vs. *ASAR* curves that quantify the intrinsic tradeoff between energetic and kinetic efficiencies—the two most significant technical performance indicators in any desalination process. These tradeoff curves are carefully established to ensure that all charging operations that a tradeoff curve represents achieve the same target adsorption. This framework of performance evaluation can be extended to different types of comparisons. For example, we can compare two MCDI processes using different electrodes, or spacers, or ion exchange membranes; we can also compare CDI processes with flow-by and flow-through configurations, or even compare MCDI and CDI processes, as long as we can construct the SEC^{-1} vs. ASAR curves for the two processes being compared, making sure they both achieve the same target adsorption.

Our analysis suggests that whether CC or CV charging is more efficient is largely dependent on the target adsorption to be achieved. There seems to be no simple rule for facile prediction of the more favorable charging mode with a given target adsorption. Moreover, our analysis uncovers an additional aspect beyond "which is better" when comparing the CC and CV charging: there exist operating regimes, defined by the target adsorption and *ASAR*, in which only one of the two charging mode can achieve. All these observations suggest that there is no definitive performance advantage of one charging mode over the other. Therefore, the selection of charging mode in practice has to be guided by experimental evaluation or numerical simulation to identify the more efficient charging mode for achieving a specific target adsorption. Lastly, it should be noted that energetic and kinetic efficiencies should not be the only aspects for deciding the charging mode in MCDI. The widely recognized superior controllability of effluent salinity may also be an important advantage of CC operation in engineering practice.

CHAPTER 6

ENHANCING ENERGY EFFICIENCY WITH IMPEDANCE-REDUCED ELECTRODES

6.1. Overview

Capacitive deionization (CDI) has experienced a drastic growth over the past decades due to its promising prospects in desalination of brackish water. In CDI, ions are adsorbed in the electrical double layer (EDL) forming at the interface between the electrode matrix and the aqueous solution upon a small voltage bias is applied across two porous electrodes, while simultaneously electric charges are stored at the interface.[1, 76] The energy spent in the adsorbing/charging step could be partially recovered in the desorbing/discharge step.[74, 83, 152] As a low-pressure separation process without the involvement of sophisticated equipment, and flexibility in salt rejection, CDI is considered to a competitive alternative to some state-of-art desalination technologies that require bulky auxiliary systems.

The electrode materials are critically important to the performance of CDI.[1] Numerous efforts have been devoted to designing and fabricating high performance CDI electrodes, which mainly focus on increasing the surface area to improve electrode adsorption capacity[20, 51, 153, 154], enabling long-term stability[65, 89, 155], modifying the surface chemistry to introduce selectivity[156-161], and utilizing Faradaic reactions to enhance charge efficiency and salt adsorption capacity Regardless of the different approaches, the ultimate goal of developing novel material for CDI electrodes is to achieve a process that is energetically efficient and kinetically favorable. Based on an energy breakdown analysis, it has been demonstrated that the energy losses not only occur in the electrode matrix, but other components including the electrode macropores and the spacer.[100-102, 162] This energy losses in the macropore and the spacer could be significant when the salinity, thus the conductivity, gets low during the charging step. Because of the purpose of desalination, the conductivity in the spacer has to be low. Therefore, it is only viable to improve the conductivity of the macropores. However, few studies have been carried out in this regard.

One way to reduce the macropore resistance is to incorporate ion exchange membranes (IEMs), i.e., MCDI, which block the repulsion of co-ions (i.e. ions have the same charge sign as the electrode) and therefore increase the charge efficiency and the macropore concentration.[11, 127] Nevertheless, the IEMs can only amplify the macropore concentration several times relative to the spacer concentration, and thus the improvement of the macropore conductivity is very limited. In addition, the presence of IEMs introduces extra resistance of the IEM.

Here, we report a new method by infiltrating ion-conductive polyelectrolyte to the macropores of the carbon electrodes to improve the kinetic and energy efficiency. We use Nafion[163, 164] to infiltrate the cathode, and quaternized poly(2,6-dimethyl-1,4-phenylene oxide)(QPPO) to the anode. Lately, studies on incorporating polyelectrolyte in carbon electrodes have been reported. *Fritz et al.* mixed the charged polymer with activated carbon powder to fabricate the inverted CDI electrodes that adsorbs the salt without charging while releasing the salt with charging.[165] Another study carved the activated carbon electrode with patterned grooves that were coated with conductive polyelectrolyte in order to improve the electrode conductivity.[166] Though we took the similar advantage of ion-conductive polyelectrolyte in the presented study, the rationale behind is quite different. We offer a convenient method to fill the electrode macropores with polyelectrolyte for the purpose of increasing the ion conductivity of the macropores and introducing the ion selectivity, and the infiltrated electrode behaves like an electrode without macropores but an ion-selective layer and micropores. The ions migrated from the spacer through the ion-selective layer to the micropores and thus the process eliminated the energy losses due to the macropores. We employ activated carbon cloth (ACC) as the platform that provides large voids for the infiltration while maintaining the electrical conductive skeleton.[167] The shape flexibility and economic accessibility also makes ACC a good candidate for CDI electrodes.

The manuscript is organized as follows. First, we present a transport model for CDI with polyelectrolyte-infiltrated electrodes (pie-CDI, or πCDI), and compare with the model for MCDI. Following this modeling approach, we show that πCDI can be seen as a limiting case of MCDI with zero macropore volume, which explains a better performance of our new method. Then, we describe the experimental setups for both MCDI and πCDI. Comparison between the model and the experiment gives good agreement via fitting the model with feasible parameters reported in the literature. Furthermore, we analyze the tradeoff curve between energy efficiency and desalination

rate, and the breakdown of energy consumption based on transport models for both setups. Results show that the πCDI systematically outperforms MCDI in both energy and kinetic aspects.

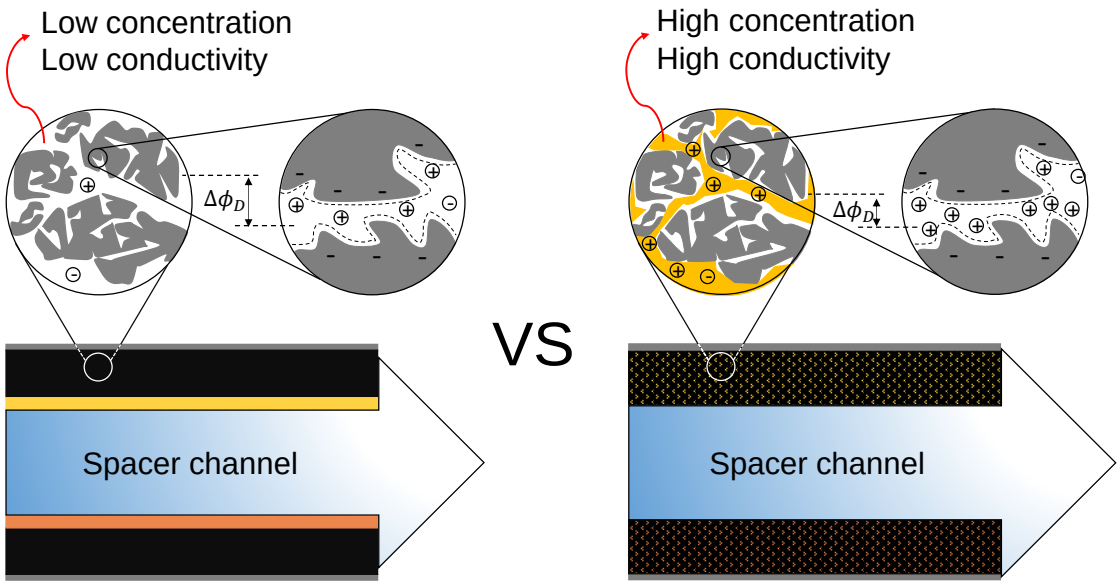

Figure 6.1 Schematics of MCDI (left) and CDI with polyelectrolyte-infiltrate electrodes, pie-CDI (right).

6.2. Model Derivation

To model the charging/discharging process in CDI, we treat the electrode as a dual-porosity materials consisting of micropores and macropores. Dynamic ion transport in the macropore and spacer is described by the Nernst-Planck equation, and local equilibrium is assumed between macropore and micropore. Then, the charging model in the micropore is specified. In this work, we employ the amphoteric Donnan (amph-D) model that considers the effects of charged groups in the micropores.[37, 68] For MCDI, the ion transport in IEM is considered and the macropore is assumed to be electroneutral, while for πCDI, the macropore is modelled as a charged media due to the infiltration of polyelectrolyte.

6.2.1. Dynamic transport modeling

We consider the ion transport in the spacer channel and the porous electrodes including both micropores and macropores. In MCDI, the macropore is electroneutral with an IEM separating the spacer from the electrode, while in πCDI, the macropore is charged due to the filling of polyelectrolyte. We further assume that the aqueous solution in the porous electrodes and the spacer channel are completely mixed, and thus neither concentration nor electrical potential gradients exist in either the electrode or the spacer. Besides, the system is assumed to be symmetric so the difference in diffusion rates between cation and anion has been ignored and the charge densities of the polyelectrolyte in πCDI are same but different signed in the paired electrodes. In this way, we can model half of the system, i.e. one electrode. A general description and comparison of the models for MCDI and pieCDI is shown in Fig 2. In the following, we specify the details of the model.

When charging or discharging the electrodes, conservation of electronic charge in the conducting matrix of one electrode gives

$$\frac{\partial}{\partial t}(p_{mi}\sigma_{elec}) = \frac{I}{L_{elec}F} \tag{6.1}$$

where σ_{elec} is the electric charge density averaged over the micropore volume, p_{mi} is the microporosity of the electrode, I is the electric current density, and L_{elec} is the thickness of one electrode. The ionic charge accumulates in the micropore to balance the electric charge in the electrode. Besides, there is chemical charge formed by functional groups at the electrode-solution interface. Conservation of the total charge in one electrode requires that[156, 168]

$$\sigma_{elec} + \sigma_{ionic} + \sigma_{chem} = 0 \tag{6.2}$$

where σ_{ionic} and σ_{chem} are the ionic and chemical charge density averaged over the micropore volume, respectively.

The ionic charge is formed by the transport of salt ions from the spacer to the porous electrode. Conservation of the total ion concentration in the porous region of one electrode gives

$$\frac{\partial}{\partial t}\left(\sum_k p_{mA}c_{mA}^k + p_{mi}c_{mi}^k\right) = \frac{J_{ions}}{L_{elec}} \tag{6.3}$$

where, J_{ions} is the total ionic flux, c_{mA}^k and c_{mi}^k are the kth ion concentration in the macropore and micropore, respectively (for single salt, $k = 1$ for cation, $k = 2$ for anion).

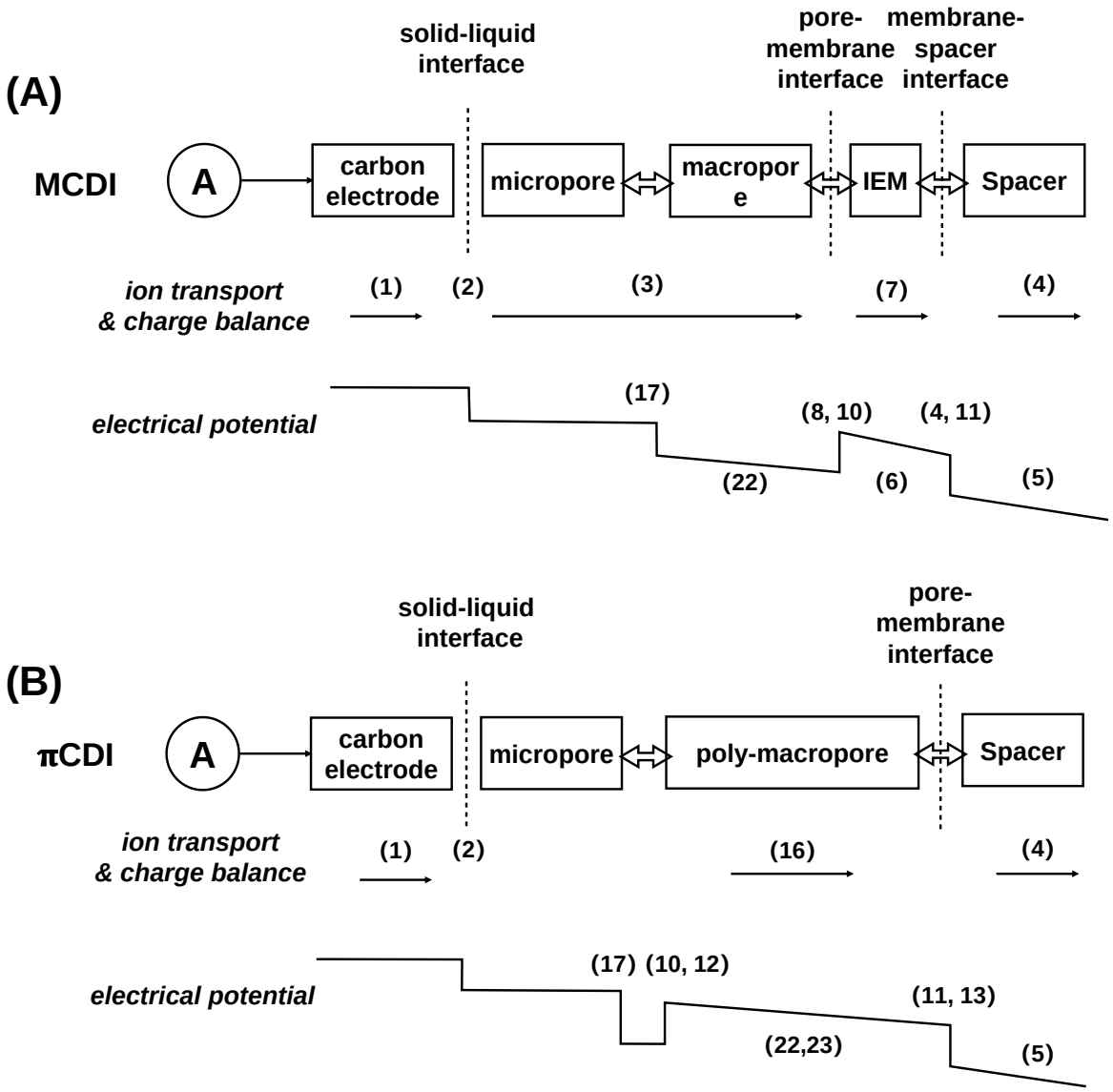

Figure 6.2 Description of models for half-cell of MCDI (A) and π-CDI (B) and profile of electrical potentials. Thin arrows indicate flow of current, double thick arrows indicate equilibrium condition, and the numbers indicate the equations used.

The ion flux to the electrode results in desalination of the feed solution in the spacer channel. The change of salt concentration in the spacer can be written as

$$p_{sp}\frac{\partial c_{sp}}{\partial t} = -\frac{J_{ions}}{L_{sp}} + \frac{c_{sp,0} - c_{sp}}{\tau} \tag{6.4}$$

where p_{sp} is the spacer porosity, c_{sp} is the salt concentration in the spacer, $c_{sp,0}$ is the feed influent concentration, L_{sp} is the spacer thickness, and τ is the hydraulic retention time in the spacer channel. Because the spacer volume is considered well mixed, c_{sp} is also the effluent concentration to be measured experimentally. According to the Nernst-Planck equation, the current density, I, depends on the electric potential difference across the spacer channel and the spacer salt concentration. Without considering concentration polarization in the spacer channel, I can be expressed as

$$I = -4Dc_{sp}\frac{\Delta\phi_{sp,half}}{L_{sp}}F \tag{6.5}$$

where D is an average bulk diffusion coefficient of the salt ions, and $\Delta\phi_{sp,half}$ is the potential drop across half of the spacer. In MCDI, this current density also equals that across the ion-exchange membrane (IEM), which can be expressed as

$$I = -D_{mem}\bar{c}_{mem}\frac{\Delta\phi_{mem}}{L_{mem}}F \tag{6.6}$$

where D_{mem} is the averaged diffusion coefficient of the salt ions in the membrane, $\bar{c}_{mem}$ is the average total ion concentration in the membrane, and L_{mem} is the membrane thickness. For simplicity, $\bar{c}_{mem}$ is approximated as the average of the ion concentrations at the two interfaces of the IEM (i.e. membrane/spacer and membrane/electrode). Because the charge density of IEM is large, it renders the preferential transport of counter-ions through. The ion flux in the IEM, J_{ions}, relates to the concentration and potential differences across the IEM:

$$J_{ions} = -\frac{D_{mem}}{L_{mem}}(\Delta c_{mem} - \omega X\Delta\phi_{mem}) \tag{6.7}$$

where Δc_{mem} is the difference between the ion concentrations at the two membrane interfaces (i.e. $c_{mem/elec}$ and $c_{mem/sp}$), ω is the sign of the membrane charge (+1 for anion exchange membranes, and -1 for cation exchange membranes), and X is the membrane charge density. Note that Eqs 6 and 7 are not necessary for πCDI due to the absence of IEMs.

Next, we assume that Donnan equilibrium is satisfied between the IEM and the macropore, the IEM and the spacer channel in MCDI, and between the spacer channel and the polyeletrolyte-filled macropore, the macropore and the spacer in πCDI (thick double arrows in Fig 2).[169, 170] In addition, both the IEMs and the polyelectrolyte-filled macropores are treated as charged porous media in a similar way so that the ion-conductive macropores filled with polyelectrolyte in πCDI

behave similarly as IEMs. Note that the macropore volume of MCDI is absent in πCDI, which accounts for the high energy efficiency of πCDI, and will be discussed in the results part.

At the membrane-electrode and the membrane-spacer interfaces in MCDI, according to the Donnan equilibrium, the total ion concentration within the membrane at each interfaces are

$$c_{mem/elec} = 2c_{mA}\cosh(\Delta\phi_{m/elec}) \tag{6.8}$$

$$c_{mem/sp} = 2c_{sp}\cosh(\Delta\phi_{m/sp}) \tag{6.9}$$

And the corresponding Donnan potential drops $\Delta\phi_{m/sp}$ and $\Delta\phi_{m/e}$ are given by

$$\Delta\phi_{m/elec} = sinh^{-1}\frac{\omega X}{c_{mA}} \tag{6.8}$$

$$\Delta\phi_{m/sp} = sinh^{-1}\frac{\omega X}{c_{sp}} \tag{6.11}$$

Eqs. 8~11 can be applied to the polyelectrolyte-infused macropores similarly, leading to

$$c_{mA,pie/mi} = 2c_v\cosh(\Delta\phi_{mA,pie/mi}) \tag{6.12}$$

$$c_{mA,pie/sp} = 2c_{sp}\cosh(\Delta\phi_{mA,pie/sp}) \tag{6.13}$$

$$\Delta\phi_{mA,pie/mi} = sinh^{-1}\frac{\omega X_{poly}}{c_v} \tag{6.14}$$

$$\Delta\phi_{mA,pie/sp} = sinh^{-1}\frac{\omega X_{poly}}{c_{sp}} \tag{6.15}$$

where c_v can be seen as the virtual concentration connecting the micropore and the macropore in pie-CDI. It is also can be understood as the concentration of a thin electroneutral liquid film inside the macropores but just outside the entrance of the micropores. Also, X_{poly} is the charge density of the polyelectrolyte.

Following Eq 7, the ion flux in the polyelectrolyte-infused macropores is

$$J_{ions} = -p_{mA}\frac{D_{mA,pie}}{L_{elec}}(\Delta c_{mA,pie} - \omega X_{poly}\Delta\phi_{mA,pie}) \tag{6.16}$$

where $D_{mA,pie}$ is the diffusion coefficient in the polyelectrolyte-filling macropores, $\Delta c_{mA,pie}$ is the difference between the ion concentrations at the two ends of the polyelectrolyte-filling macropores. and $\Delta\phi_{mA,pie}$ is the potential drop across such macropores.

6.2.2. Micropore charging model

In the micropore, we employ the amphoteric Donnan (amph-D) model that considers the effects of charged groups in the micropores of the electrodes.[37] These surface-immobilized charged functional groups (σ_{chem}), together with the mobile ionic charges (σ_{ionic}), balance the electronic charges (σ_{elec}) in the carbon electrode.[37, 68, 156, 168] The amph-D model assumes two types of micropore regions: the acidic region named as A-region, and the basic ration as B-region. The A-region may contain groups such as carboxyl, lactone or phenol and is thus negatively charged, while the B-region has protonated groups that are positively charged.[171, 172]

The concentration of ions in the electrode micropores is related to the macropore ion concentration via the Donnan potential across the interface between the micro- and macro-pores:

$$c_{mi,j}^{\pm} = c_{mA}\exp(-z^{\pm}\Delta\phi_{D,j}) \tag{6.17}$$

where $c_{mi,j}^{\pm}$ is the ion concentration in the *j*-region of the micropores, c_{mA} is the macropore salt concentration, $z^{\pm}$ is the ion charge valence (e.g., +1 for monovalent cation and -1 for monovalent anion), and $\Delta\phi_{D,j}$ is the dimensionless Donnan potential difference between the *j*-region of the micropores and the macropores. The *j*-region could be either acidic or basic, i.e. A- or B-region. For pie-CDI, c_{mA} should be replaced by c_v.

The volumetric ionic micropore charge density ($\sigma_{ion,j}$) is determined by the cation and anion concentrations in the micropores

$$\sigma_{ionic,j} = c_{mi,j}^{+} - c_{mi,j}^{-} = -2c_{mA}\sinh\left(\Delta\phi_{D,j}\right) \tag{6.18}$$

In addition, $\sigma_{elec,j}$ is related to the Stern layer potential difference ($\Delta\phi_S$) and Stern layer capacitance (C_S):

$$\sigma_{elec,j}F = -C_S\Delta\phi_S V_T \tag{6.19}$$

where F is the Farady constant (96485 C·mol^{-1}), and V_T is the thermal voltage that convert the unit to volt (@ room tempeterature, $V_T = 25.6\,mV$).

The average electronic charge density is given by:

$$\sigma_{elec} = \sum \alpha_j\,\sigma_{elec,j} \tag{6.20}$$

where σ_{elec} is the average electronic charge density in the micropores of the electrodes, and α_j is the fraction of *j*-region relative to the total micropore volume. In this study, both α_A and α_B are assigned as 0.5, as they has been treated in previous studies, and their chemical charges are same

magnitude but different in sign, i.e. negative and positive for A- and B- regions respectively. In other words, the paired electrodes are symmetric.

There is a constraint of the A- and B- regions, that is the potential drops over the EDL, $\Delta\phi_{EDL}$ for each are equal

$$\Delta\phi_{EDL,A} = \Delta\phi_{EDL,B} \tag{6.21}$$

6.2.3. Potential drops

The potential drop in the porous carbon electrode ($\Delta\phi_{elec}$) is determined by the salt concentration in the macropores and the current density:

$$\Delta\phi_{elec}V_T = IR_{elec}/\bar{c}_{mA} \tag{6.22}$$

where R_{elec} is the specific electrode resistance and $\bar{c}_{mA}$ is the average concentration in the electrode macropore, which both are treated differently for the two kinds of cells. In MCDI, R_{elec} is a fitting parameter that is tuned to match the experimental and modelled results for cell voltage, and we do not consider the concentration gradient along the macropore. With respect to πCDI, $\bar{c}_{mA}$ is the average concentration of $c_{mA,pie/mi}$ and $c_{mA,pie/sp}$, and its R_{elec} is calculated following the equation:

$$R_{elec} = \frac{V_T L_{elec}}{D_{mA,pie} F p_{mA}} \tag{6.23}$$

Finally, the CDI cell voltage is simply the twice of sum of all potential drops from the carbon phase to the spacer channel (assuming symmetric potential distribution between two half-cells):

$$V_{cell} = 2(\Delta\phi_{EDL} + \Delta\phi_{elec} + \Delta\phi_{m/sp} + \Delta\phi_{mem} - \Delta\phi_{m/elec} + \Delta\phi_{sp,half})V_T + IR_{ext} \tag{6.24}$$

where R_{ext} ($\Omega\cdot cm^2$) represents all resistances in the external circuit, the current collectors, and the contact resistances between the current collectors and the electrodes. For πCDI, the membrane potential drop is eliminated. The potential drops at the membrane edges, i.e. $\Delta\phi_{m/sp}$ and $\Delta\phi_{m/e}$ shall be replaced by $\Delta\phi_{mA,pie/sp}$ and $\Delta\phi_{mA,pie/mi}$, respectively.

6.3. Methods and Experiments

6.3.1. Electrode preparation

Electrodes were prepared by infiltrating conductive polyelectrolyte into the activated carbon cloth (ACC, FM 50K, Zorfklex, Pittsburg, PA). Two kinds of polyelectrolyte were used, negatively charged Nafion and positively charged quaternized poly(2,6-dimethyl-1,4-phenylene oxide)(QPPO). Nafion and QPPO were used to modify the cathode and anode, respectively. The infiltration of Nafion was conducted by soaking ACC in a 15% wt LOQUION solution (Ion Power Inc., Delaware, USA) for 1 hr followed by 1 hr drying at 60 ℃ and 1 hr annealing at 140 ℃ in a vacuum oven. The anion selective QPPO polyelectrolyte was obtained by bromination of poly(2,6-dimethyl-1,4-phenylene oxide)(Sigma Aldrich) following a protocol that described in previous studies. The QPPO solution was prepared by mixing QPPO, methanol and dimethylformanide of which the content was specified in Ref x.[173] The as-prepared solution was used to infiltrate ACC, following the similar approach as the infiltration Nafion, but the annealing temperature was changed to 90 ℃. The infiltrated electrodes were then tailored to squares with a dimension of 6×6 cm^2, at the center of which a 1.6×1.6 cm^2 square hole was cutout. In the control experiment where ACC was used as received without further treatment other than washing with Milli-Q water, and it was tailored to the identical shape as the infiltrated counterparts.

6.3.2. Experimental setup and methods

MCDI stack consisted of two cells in parallel, each of which had two ACC electrodes, a glass fiber spacer, and an IEM at each side of the spacer (Figure 1). Similarly, two pairs of infiltrated ACC electrodes with spacers made up the πCDI stack. The tacks were firmly compressed into the corresponding acrylic housing. The feed solution enters from the periphery of the stack and exits through the center hole. Right after the exit, an in-line conductivity meter (Edaq Isopod, Australia) was placed to continuously monitor the effluent conductivity, which is connected to a desktop for data acquisition. The raw data was converted to salt concentration based on a calibration curve. The feed solution was a 20 mM NaCl solution, and it was continuously purged with nitrogen to remove dissolved oxygen. The feed solution was pumped through the cell

housing, and the effluent was sent back to the feed reservoir. A potentiostat (SP 150, Bio-Logic, France) was employed to apply constant current in the charging step and zero voltage in the discharge step.

To evaluate the performance of πCDI in comparison with MCDI, the kinetic-energetic tradeoff curves were constructed for both cells achieving the same diluted volume with the same concentration. The details of the experimental protocol have been described in previous studies.[72, 117, 174] The charging and discharge cycles were repeated at least three times to ensure dynamic steady states. The targeted average diluted concentration was 16.5 mM and the diluted volume was 18 mL.

6.3.3. Data Analysis

To check the target adsorption is achieved, the average diluted concentration, $\bar{c}_D$, is calculated via the following equation:

$$\bar{c}_D = \frac{\int_0^{t_c} c_D(t)dt}{t_c} \tag{6.25}$$

Where $c_D(t)$ is the effluent concentration in the charging step that changes with respect to time, and t_c is the charging step duration.

Two performance metrics, specific energy consumption (*SEC*) and average salt adsorption rate (*ASAR*) are evaluated for both cells. *SEC* is defined as the energy consumed to remove a unit mole of NaCl:

$$SEC = \frac{\int_0^{t_c} IV(t)dt}{Q\int_0^{t_c}\big(c_0 - c_D(t)\big)dt} \tag{6.26}$$

where I is the applied current during the charging stage, $V(t)$ is the corresponding cell voltage that measured with the potentiostat, Q is the flowrate to the cell stack, and c_0 is the initial feed concentration. Alternatively, SEC^{-1}, the mass of salt removed when consuming a unit energy, is utilized to construct the tradeoff curves.

The deionizaion kinetics, *ASAR*, defined as the amount of salt removed during the charging step normalized by the product of electrode mass (W) and charging time.

$$ASAR = \frac{Q \int_0^{t_c} \left(c_0 - c_D(t)\right) dt}{W t_c} \tag{6.27}$$

6.4. Results and Discussion

6.4.1. Experimental results and model validation

In order to evaluate the performance of the πCDI in comparison with conventional MCDI, a series of experiments achieving the same target desalination were conducted for both cells. The target separation is specified by a c_0 of 20 mM, a $\bar{c}_D$ of 16.5 mM and a diluted volume (V_D) of 18 mL. A typical cycle of πCDI and MCDI with constant current charging and zero charge discharge is presented in Figure 3. The effluent concentrations and cell voltages agree with the model results. Upon charging the cell with constant current, the effluent concentration reaches a plateau after the initial decrease. At the same time, the cell voltage keeps increasing until the charging step is terminated. To achieve the same V_D with the identical $\bar{c}_D$, a higher current density is needed for πCDI in comparison with MCDI, i.e. 1.50 vs 1.76 mA cm^{-2}. However, the cell voltage in the pie-CDI is smaller than that in the MCDI, indicating smaller electrode resistances.

Additional experimental results fitting with model are presented in the Supporting Information, with a summary of the model parameter settings.

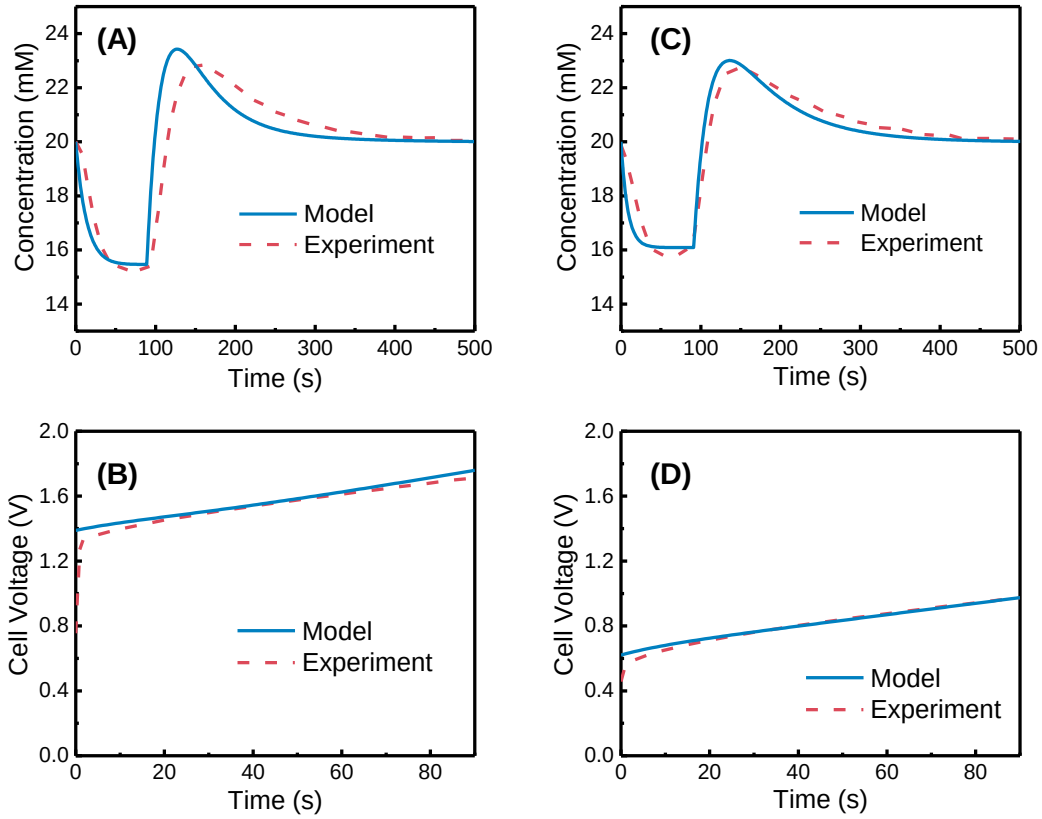

Figure 6.3 Effluent concentration and cell voltage as function of time: MCDI (A&B) and π-CDI (C&D). The flowrate to the cell was 12 mL min^{-1} and the corresponding HRT was 17 s for both systems. The current densities were 1.50 and 1.76 mA cm^{-2}, respectively, for MCDI and pie-CDI. The volume and the concentration of the diluted streams were 18 mL and ~16.5 mM respectively, and the consequential *ASAR*s were around 22 μmole g^{-1} min^{-1}. The dashed curves were experimental data, while the solid curves were simulated from the developed models that were numerically solved

6.4.2. Performance analysis

A series of experiments with various flowrates (i.e. HRT) and current densities but diluted concentration and volume were conducted for both MCDI and πCDI cells. Figure 4 presents the operating conditions and the experimental results from these experiments. To achieve the same $\bar{c}_D$, the flowrate increases nearly linearly with current density in both cells. In addition, the flowrate for MCDI is generally higher than that for πCDI when charging at the same current density (Figure

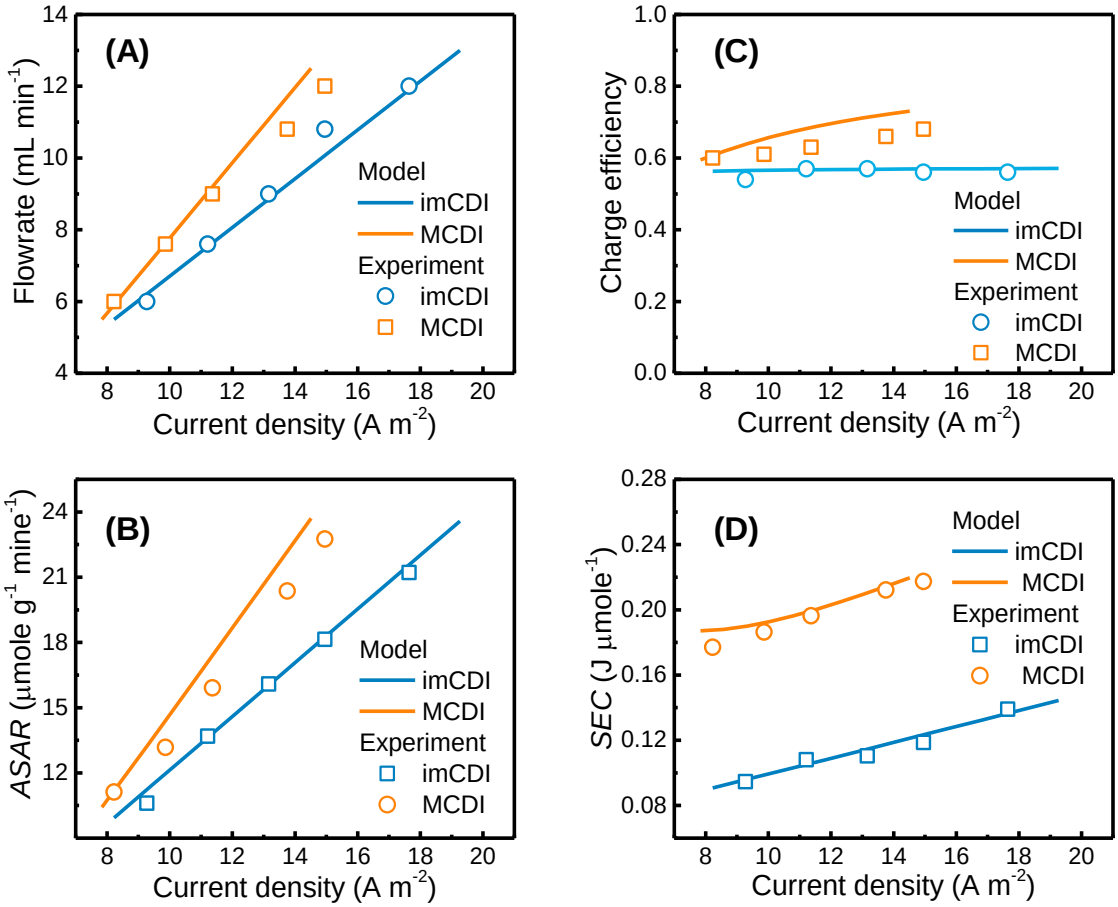

Figure 6.4 Operating flowrate changes as function of charging current density achieving the diluted concentration of 16.5 mM from 20 mM feed and the corresponding charge efficiency (A). The average salt adsorption rate, i.e. *ASAR*, increase linearly with respect to charging current density (B). And the specific energy consumption, i.e. *SEC*, increase when increasing the charging current density (C). All the solid curves are simulated with the models, while the open squares and circles are obtained from experiments of MCDI and imCDI, respectively.

4A). In other words, a larger current density has to be applied for πCDI relative to MCDI when the flowrate to the spacer is same. These phenomenon indicate that a higher charge efficiency is attained in MCDI (Figure 4B), but the superiority becomes more notable at large current densities. The charge efficiency for πCDI is barely dependent on current density or flowrate, while that for MCDI increases with current density or flowrate. The increasing charge efficiency in MCDI is mainly due to the increasing flowrate that diminishes the initial phase reaching the plateau

concentration from the feed.[122] When charging with the same current density, a smaller kinetics, quantified by *ASAR*, is found in πCDI, with an enlarging difference at high current densities (Figure 4C). Nevertheless, the specific energy consumption (*SEC*) in πCDI is only about half of that in MCDI (Figure 4D) due to the less impedance in the electrodes.

In general, the model successfully predicts the data very well for all the experiments, which demonstrates the credibility of the model for further analysis.

6.4.3. Evaluate πCDI vs. MCDI

In this section, we evaluate the performance of πCDI in comparison with MCDI following the framework introduced in previous studies. Briefly, tradeoff curves were constructed for both processes achieving the same separation. Along each curve, it represents *ASAR* and corresponding SEC^{-1} for that specific separation, and *ASAR* increases with decreasing SEC^{-1}, and vice versa. When comparing different processes and each of them has a tradeoff curve, any curve that sits above demonstrates a better energetic-kinetic performance than the other if these curves do not intersect. In the case that intersection occurs, we have to specify that the ranges that one is better whereas the other is better in other ranges.

When comparing the curves of MCDI with πCDI, as shown in Figure 5, SEC^{-1} of πCDI is higher than that of MCDI in the range of being studied, spanning from 10 to 24 μmole g^{-1} min^{-1}. The difference between the SEC^{-1}s for the two cells is more prominent in the lower end of *ASAR*. For instance, when achieving an *ASAR* of 10 μmole g^{-1} min^{-1}, SEC^{-1} of πCDI is 11 μmole J^{-1}, which doubles that of MCDI. Across the *ASAR* range, πCDI demonstrates a higher dependence of SEC^{-1} on *ASAR* in contrast to MCDI.

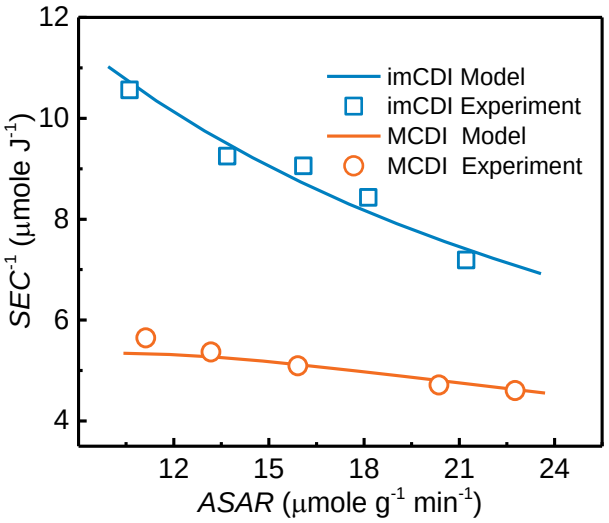

Figure 6.5 SEC^{-1} vs *ASAR* for the charging stage of imCDI (blue) and MCDI (orange). The solid curves are simulated data that are numerically solved while the open symbols are calculated from experimental results. All the experiments and the simulation achieve the same separation that is defined as a diluted concentration of 16.5 mM from a feed of 20 mM and the diluted volume is 18 mL.

6.4.4. Comparison of energy breakdown

Because there are multiple layers in the cells, it is of significant meaning to quantify the energy loss in each component and to compare such breakdowns of two systems so as to identify the improvement of energy efficiency. In this section, we present the comparison of the breakdowns at two *ASAR*s that are close to the lower bound and higher bound of the range studied. Since the energy consumption is a function of the charging time, here we only look at the *SEC* at the end of the charging step.

Referring to the breakdowns, the largest decrease from MCDI to πCDI occurs in the electrode macropores, which is attributed to the reduced impedance as highly charged polyelectrolyte fills the macropores and attracts a large amount of counter ions. It reduces nearly 7 times from 69.8 to 9.7 J $mole^{-1}$ from MCDI to πCDI, which accounts for 70% of the total saved energy in πCDI from MCDI when operating at an *ASAR* of 11.3 μmole g^{-1} min^{-1}. Moreover, this

reduction becomes more significant when achieving a higher *ASAR*. Other than the improvement in the macropores, the absence of IEMs in πCDI eliminates the potential drops and thus the energy consumption in the IEMs.

The resistance in the spacer is identical as both processes achieve the same diluted concentration in the spacer, assuming that there is no concentration profiles forming in the spacer channel, namely it is seen as a continuously stirred reactor. The potential drop in the spacer channel is then only dependent on charge density. Because the slightly lower charge efficiency is with πCDI, a higher current density has to be applied and therefore a higher energy consumption is found in the spacer, and this becomes more noticeable when achieving higher *ASAR* which intrinsically requires a larger current density.

Another component that consumes more energy in πCDI than in MCDI is the Donnan potentials at the two edges of the IEMs or the polyelectrolyte. In the πCDI of which the macropores are filled with the highly charged polyelectrolyte, the counter ion concentration in the macropores is quite high, rendering high Donnan potentials at the two ends of the polyelectrolyte-filled macropores. In contrast to the spacer, the energy consumption due to this Donnan potentials seem to be seldom dependent on the *ASAR*. When increasing the *ASAR* doubles from 11.3 to 22.7 μmole g^{-1} min^{-1}, the Donnan potential *SEC* stays around 20 and 10 J $mole^{-1}$ for πCDI and MCDI, respectively.

Both microporous Donnan and Stern potentials build up, as the ions are stored in the micropores and charges transferred to the electrode matrix. The Stern potential is directly related to the Stern capacitance and the micropore charge density.[10] Following the assumption that the polyelectrolyte does not penetrate into the electrode micropores, the property, e.g. Stern capacitance, is considered as identical in the model. Therefore, the potential drops and the energy consumption are different resulting from the different micropore charge densities, which in return are due to the different micropore concentrations. By comparing the consumption by Stern potential (as shown as pink in Figure 6), πCDI spends less energy indicating that the micropore densities in the πCDI is smaller, though it adsorbs the same amount of salt ions as the MCDI. The microporous Donnan potential is determined by the ion concentration ratios between the micropore and the macropore. The macropores of πCDI are filled with charged polyelectrolyte which renders high concentration of counter ions in the macropoes, and therefore the Donnan potential as well its energy consumption are smaller in πCDI in comparison with MCDI.

With respect to the equivalent circuit resistance (ESR) that includes the contact resistance between the electrode and the current collector and the external resistances in the electrical circuit, it is same for both processes and its contribution to the total SEC is only proportional to the current density. As discussed before, the current density for πCDI is higher than that for MCDI to a small extent, the ESR SEC is about the same for both cells.

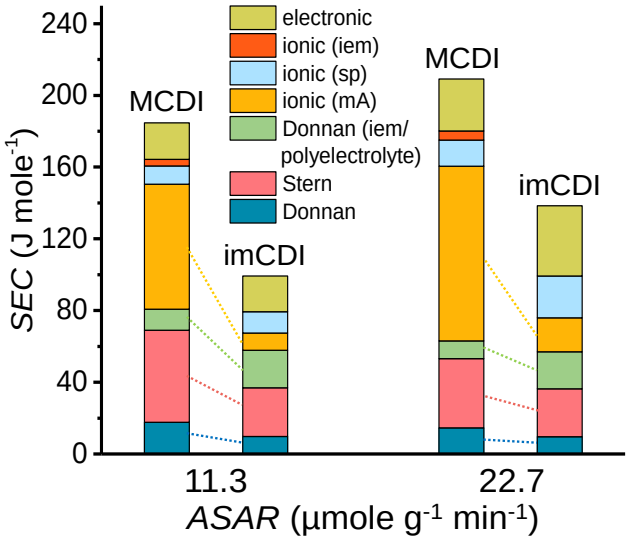

Figure 6.6 Comparison of the breakdown of *SEC* for MCDI and imCDI. The data were calculated from the developed models achieving the aforementioned separation. The model simulated the breakdowns for two *ASAR*s, i.e. 11.3 and 22.7 µmole g^{-1} min^{-1}.

6.5. Conclusions

The macropores of electrode contributed largely to the total energy consumption in CDI process. The infiltration of ion-conductive polyelectrolyte reduced the impedance of macropores, which lead to less energy losses in the macropores. Compare the polyelectrolyte-infiltrating CDI (pie-CDI) with the classic MCDI, it consumed much less energy when achieving the identical target adsorption (same diluted concentration with same volume). Employing the kinetic energetic tradeoff curves, pie-CDI outperformanced MCDI in the range of interest, while the advantage dwindles as *ASAR* increased. Theoretical models considering the chemical charges on the electrode

carbon surface were developed, and they fit the experimental data extremely well for the corresponding data. The validated models were further employed to analysis the energy breakdowns for both pie-CDI and MCDI, which revealed that the energy consumption in the macropores were significantly reduced in pie-CDI along with the elimination of energy losses due to IEMs.

CHAPTER 7

MODELING FLOW-ELECTRODE CAPACITIVE DEIONIZATION

This chapter is a part of the following manuscript: Wang L., Zhang, C., Waite, T.D., Lin S., Equivalent film-electrode model for flow-electrode capacitive deionization, which has been submitted to a peer-reviewed journal *Environmental Science & Technology* for possible publication.

7.1. Overview

Capacitive deionization (CDI), also referred to as electrosorption, is an emerging electrochemical desalination technology of particular current interest in view of its potential to become a competitive technology in certain desalination applications.[1, 76] With carbonaceous electrodes, CDI involves the removal of ions from the feed stream and storage of these ions in the electrode micropores when a voltage is applied with subsequent release of the stored ions into the brine stream when the electrodes are short-circuited or a reverse voltage is applied.[20, 22, 35] There are a variety of CDI cell configurations and operational modes,[11, 16, 23, 72] among which flow electrode CDI (FCDI) has received extensive and growing interest.[24, 66, 175, 176] Three major advantages of FCDI over other CDI configurations include (i) the ability of continuous operation[152, 177, 178] compared to cyclic operation in conventional CDI that is more difficult to control and optimize; (ii) the possibility of achieving a high degree of salinity reduction;[64, 177, 179] and (iii) extremely high flow efficiency (~100%) as the desalinated and brine streams are generated in separate chambers.[122, 152, 180]

In FCDI, flow electrodes comprising a slurry mixture of activated materials (i.e., activated carbon, AC), conductive additives (e.g., carbon black particles, carbon nanotubes and redox couples) and aqueous electrolyte are pumped through two electrode channels while the salty feed water flows through the spacer channel.[181, 182] Typically, ion exchange membranes are employed to separate the electrode channels from the spacer channel. There are two general modes in which FCDI may be operated, namely, the short-circuited closed-cycle (SCC) operation and the isolated

closed-cycle (ICC) operation.[177, 183] In ICC mode, the positively and negatively charged flow electrodes are isolated and recirculated between their respective electrode channels and electrode reservoirs. Similar to conventional CDI, ICC-FCDI is an intermittent process as it requires that the flow electrodes be regenerated by applying a reverse voltage. In contrast, continuous, steady-state FCDI operation can be achieved using SCC operation. In SCC operation, the flow electrodes are regenerated when the positively and negatively charged AC slurries exiting the FCDI cell are mixed together in a single reservoir (Figure 7.1A). The contact between these oppositely charged AC particles results in neutralization of the AC and release of the adsorbed ions to the electrolyte solution that becomes the brine.

Recent advances in film-electrode based CDI, i.e. CDI systems utilizing porous solid phase film electrodes, can be attributed, in part, to the enhanced fundamental understanding that has accrued from the development of dynamic CDI models. The ability to model the behavior of CDI systems is critical to understanding the impacts of system parameters and operating conditions on CDI performance and for optimizing CDI system design and operation.[72, 82, 117, 174] Models with different levels of fidelity have been developed for film-electrode CDI[10, 70, 73, 184] however very limited effort has been devoted to the modeling of FCDI. The major challenge in modeling FCDI is the treatment of the dynamic percolation between AC particles in the flow-channels, which is dependent on AC loading and flow characteristics.[185]

The only FCDI model that has been reported is that by Rommerskirchen et al. where they discretized the FCDI cell in the flow direction and coupled ion transport with the modified Donnan (mD) model for description of the electrical double layer (EDL).[186] However, the use of the Stern layer capacitance as a fitting parameter that varies in different operations is not only physically ungrounded but also undermines the predictive power of the model (i.e., while this model can be used for fitting experimental data, it cannot be used for predicting performance). For example, increasing AC loading in the flow electrode promotes more frequent collision of AC particles and thus enhances the conductivity of the flow electrode. However, this effect of increasing AC loading is incorrectly accounted for by changing the Stern layer capacitance. In contrast, previous studies on fixed electrode CDI with AC film electrodes have revealed that the Stern layer capacitance is dependent on the micropore charge density via the mechanism of electrostatic compression but not directly dependent on other operating conditions.[39, 187]

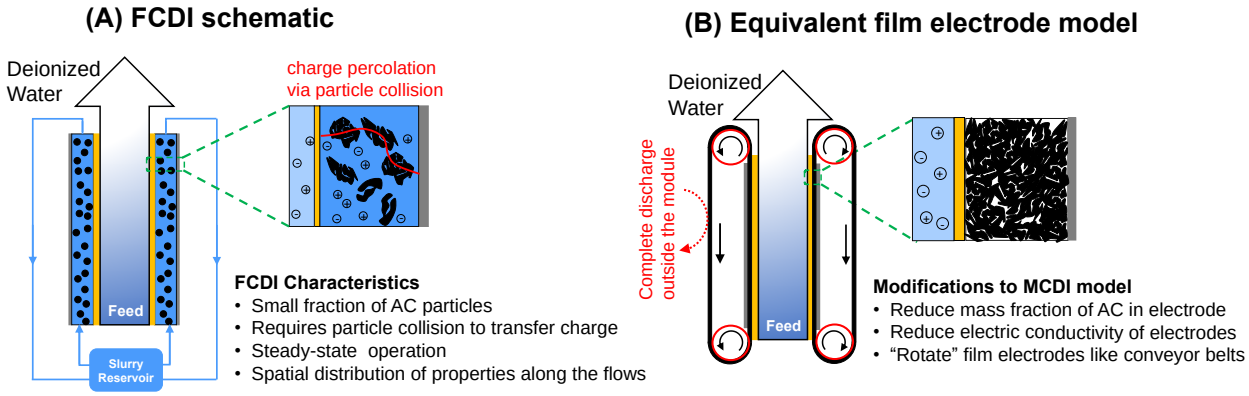

Figure 7.1 (A) Schematic of the FCDI system operating in short-circuited closed-cycle (SSC) mode. (B) the equivalent film-electrode model in which the film electrodes behave as conveyor belts that rotate through the FCDI module. The major characteristics of the FCDI system are listed in (A) and the corresponding measures for modifying the MCDI model to account for such characteristics are lised in (B).

We demonstrate in this study that the system-level behavior of FCDI can be approximately modeled by an equivalent CDI model of moving film electrodes without the need for considering the mechanistic details of inter-particulate mass and charge transfer (Figure 6.1B). Specifically, a flow electrode stream can be approximated as a film electrode with much larger macro-pore volume and significantly reduced electrical conductivity. Such an equivalent film electrode (EFE) moves in the direction of the flow in a manner similar to a "conveyer belt". Following this approximation, we develop a pseudo-1D model that describes the ion transport and the EDL formation in the FCDI processes using a framework similar to that implemented by Rommerskirchen et al. but with more appropriate treatment of the Stern layer capacitance and the effect of AC loading. This pseudo-1D equivalent film electrode (EFE) model is validated using FCDI experiments in SCC mode and is then employed to evaluate the FCDI performance over a wide range of operating conditions. In addition, the EFE-FCDI model developed here is used to describe the spatial distribution of the important properties in the FCDI cell and the breakdown of the energy losses in the system.

7.2. Model Development

7.2.1. System Description

In this section, we present the governing equations of a pseudo-1D EFE model that describes ion transport in the spacer channel and ion retention in the electrode channel. Both the spacer and the electrode channels are divided into *N* subcells connected in series, each of which is assumed to be a continuously stirred-tank reactor (CSTR). In this study, *N*=8, which makes the channels approach plug flow reactors.[188] The electrode channel consists of AC particles with intra-particulate macropores and micropores. The volume occupied by the electrolyte solution outside the AC particles is considered as a large extra-particulate macropore. In the EFE model, intra-particulate and extra-particulate macropores are not distinguished and have the same ion concentration. Based on existing film-electrode CDI models, micropores contribute to the majority of ion storage capacity while macropores serve as pathways for rapid ion transport.

7.2.2. Ion Transport in a Unit Cell

As the spacer channel is discretized into *N* sub-cells in series, the mass balance of salt in each CSTR-like subcell can be expressed as:

$$p_{sp} V \frac{\partial c_{sp,k}}{\partial t} = -J_{salt,k} A + Q_{sp}(c_{sp,k-1} - c_{sp,k}) \tag{7.1}$$

where p_{sp} is the spacer porosity, V is the volume of the subcell, $c_{sp,k}$ is the spacer channel concentration in subcell k, $J_{salt,k}$ is the salt flux from the spacer channel toward the electrode channel in sub-cell k (same as the ion fluxes $J_{ions,k}$), A is the effective contact area between the spacer and the electrode channels and Q_{sp} is the stream flowrate in the spacer channel. The transport of ions across the respective IEM is driven by gradients of both electrical potential and concentration. The flux of ion species i, $J^i_{ions,k}$, in sub-cell k can be described by the Nernst-Planck equation:

$$J^i_{ions,k} = -D_m\left(\frac{\partial c^i_{m,k}}{\partial x} + z^i c^i_{m,k} \cdot \frac{\partial \phi_{m,k}}{\partial x}\right) \tag{7.2}$$

where D_m is the diffusion coefficient in the IEM (D_m is ion-specific in principle but, in this model, we use the mean diffusion coefficient of the salt), $c_{m,k}^{i}$ is the concentration of *i* in the IEM of subcell *k*, and $\phi_{m,k}$ is the dimensionless electrical potential in the membrane subcell *k*. Due to the requirement for local electro-neutrality in the membrane, the following equation applies:

$$c_{m,k}^{+} - c_{m,k}^{-} + \omega X = 0 \tag{7.3}$$

where $c_{m,k}^{+}$ and $c_{m,k}^{-}$ are concentrations of cation and anion in the IEM of subcell *k*, respectively, X is the intrinsic charge density of IEM and ω is the sign of the charge (i.e., -1 for cation exchange membrane, CEM, and +1 for anion exchange membrane, AEM).

Considering both cation and anion fluxes by adding equations (6.2) and (6.3) with the simplifying assumption of linear gradients for concentration and electrical potential across the IEM, we arrive at the following equation:

$$J_{ions,k} = -\frac{D_m}{L_m}(\Delta c_{m,k} - \omega X \Delta\phi_{m,k}) \tag{7.4}$$

where L_m is the thickness of the membrane and $\Delta c_{m,k}$ is the difference in total ion concentrations (i.e., $c_{m,k} = c_{m,k}^{+} + c_{m,k}^{-}$) between the two edges of the IEM. Here, the edge refers to the IEM phase that is next to the interface. In other words, $\Delta c_{m,k} = c_{m/elec,k} - c_{m/sp,k}$ with $c_{m/elec,k}$ being the IEM-phase salt concentration next to the interfaces between the IEM and the electrode channel of subcell *k*, and $c_{m/sp,k}$ being the IEM-phase salt concentration at the interfaces between the IEM and the spacer channel of subcell *k*. The IEM-phase concentrations near the interface are related to the solution concentrations near the interface in a manner reasonably described by the following expressions:

$$c_{m/elec,k} = 2c_{mA,j}\cosh(\Delta\phi_{m/e,k}) \tag{7.5}$$

$$c_{m/sp,k} = 2c_{sp,j}\cosh(\Delta\phi_{m/sp,k}) \tag{7.6}$$

where $c_{mA,k}$ and $c_{sp,k}$ are macropore and spacer concentrations in subcell k and $\Delta\phi_{m/e,k}$ and $\Delta\phi_{m/sp,k}$ are the Donnan potentials across the electrode/IEM and spacer/IEM interfaces in sub-cell *k*, respectively.

The current density of subcell *k*, I_k, depends on the electrical potential difference across the spacer channel and the spacer salt concentration:

$$I_k = -2Dc_{sp,k}\frac{\Delta\phi_{hf-sp,k}}{L_{sp}/2}F \tag{7.7}$$

where D is the bulk diffusion coefficient of the charged ions (we use the mean diffusion coefficient of the salt here), $\Delta\phi_{hf-sp,k}$ is the dimensionless potential drop of half of the spacer channel of subcell *k*, $L_{sp}/2$ is half of the spacer thickness and F is the Faraday constant. Eq 6.7 assumes that the suspension in the spacer volume in subcell *k* is completely mixed and thus has no concentration gradient. Because the current density in the spacer equals that in the IEM, it can be quantified as shown in Eq 7.8:

$$I_k = -D_m \bar{c}_{m,k} \frac{\Delta\phi_{m,j}}{L_m} F \tag{7.8}$$

where $\bar{c}_{m,k}$ is the average ion concentration in the IEM in subcell *k*.

7.2.3. Ion Partitioning between Micropores and Macropores

Upon charging, electrical double layers (EDLs) overlap substantially inside the micropores of the AC which renders the modified Donnan (mD) approximation applicable for describing the ion distribution between micropores and macropores in each subcell. The mD model assumes a constant potential inside the micropore and thus a single potential difference between the micro- and macro-pores (i.e., the dimensionless Donnan potential in subcell k, $\Delta\phi_{D,k}$). The ratio of the concentration of a specific ion *i* in the micropore, $c^i_{mi,k}$, and the concentration of the same ion in the macropore, $c_{mA,k}$, is governed by $\Delta\phi_{D,k}$ via the Boltzmann distribution:

$$c^i_{mi,k} = c_{mA,k} \exp\left(-z^i \Delta\phi_{D,k}\right) \tag{7.9}$$

where z^i is the valence of ion *i*. In the subcell *k* of the electrode, the volumetric charge density in the micropores ($\sigma_{mi,k}$, unit: mole per volume) rises as a result of the concentration difference between counter-ions and co-ions:

$$\sigma_{mi,k} = \sum_{i=1}^{n} z^i c^i_{mi,k} \tag{7.10}$$

For simplicity, in this study, we only consider a single solute of 1:1 electrolyte (e.g., NaCl), in which case eq. 10 becomes

$$\sigma_{mi,k} = -2c_{mA,k} \sinh\left(\Delta\phi_{D,k}\right) \tag{7.11}$$

At the same time, $\sigma_{mi,k}$ is also related to the dimensionless Stern layer potential difference ($\Delta\phi_{St,k}$) and the volumetric Stern layer capacitance in the micropore ($C_{St-vol,k}$):

$$\sigma_{mi,k}F = -C_{St-vol,k}\Delta\phi_{St,k}V_T \tag{7.12}$$

where V_T is the thermal voltage that converts the dimensionless voltage to the unit of volt (25.6 mV at 298K). It has been shown that the volumetric Stern layer capacitance increases with charge density due to electrostatic compression. This relationship be can approximated using the following empirical expression:

$$C_{St-vol,k} = C_{St-vol,0} + \alpha\sigma_{mi,k}^2 \tag{7.13}$$

where α is an empirical coefficient and $C_{St-vol,0}$ is the volumetric Stern layer capacitance when the micropore charge density is zero.

7.2.4. Electrode channel modelling

The flow electrode consists of AC particles, CB particles and the electrolyte. Compared with film electrodes, the flow electrode has a much smaller volume fraction of micropores and thus a much smaller microporosity, due to the low weight-to-volume fraction of AC particles. In addition, as opposed to a film electrode, the electrical conductivity of the flow electrode channel results from the conductivity of both AC particles and the electrolyte with the contribution of the electrolyte dependent on the electrolyte salinity. We propose an empirical expression to estimate the overall conductivity of the flow electrode in a subcell with this expression accounting for the conductivity of pure AC, ρ_{AC}, and the mass fraction of carbon, wt (dimensionless). The overall conductivity (ρ_{elec}) of the electrode channel is expressed as:

$$\rho_{elec} = \lambda_s c_{mA}(1 - wt) + \rho_{AC} wt^{\gamma} \tag{7.14}$$

where λ_s is the molar conductivity of the solution and γ is an empirical coefficient that is independent of operating conditions. Because the flowrate of the flow electrode slurry is large in this study, we ignore the influence of the slurry flowrate in the present model. With lower slurry flowrates, however, less frequent collisions between AC particles may also lead to lower overall conductivity. Combining the potential drop across the Stern layer and the Donnan potential, we can rewrite the overall potential drop in the electrode channel as follows:

$$V_{elec,k} = 2V_T\left(\Delta\phi_{D,k} + \Delta\phi_{St,k}\right) + 2I_k A/\rho_{elec,k} \tag{7.15}$$

The total voltage across the unit cell is the summation of all the voltage drops. Assuming the cell is symmetric, the total voltage can be represented as:

$$V_{total,k} = 2V_T(\Delta\phi_{hf-sp,k} + \Delta\phi_{m/sp,k} + \Delta\phi_{m,k} - \Delta\phi_{m/e,k}) + 2V_{elec,k} + I_k R_{esr} A \tag{7.16}$$

where R_{esr} is the specific equivalent series resistance including the resistances that occur in between the current collector and the flow electrode and that in the electrical circuit. Note that in simulating the FCDI process under steady state, the cell voltage in every unit cell is the same and equal to the overall cell voltage.

For each subcell k of the flow electrode channel, $c_{mA,k}$ and $c_{mi,k}$ are related to the ion flux $J_{ions,k}$ by the following equation (similar to eq. 1):

$$\frac{\partial}{\partial t}\left(2p_{mA}\mathrm{c}_{mA,k} + p_{mi}\mathrm{c}_{mi,k}\right) = \frac{J_{ions,k}}{L_{elec}} + \frac{2p_{mA}\left(\mathrm{c}_{mA,k} - \mathrm{c}_{mA,k-1}\right) + p_{mi}(\mathrm{c}_{mi,k} - \mathrm{c}_{mi,k-1})}{\tau_{elec}/N} \tag{7.17}$$

where τ_{elec} is the total HRT of carbon slurry in the electrode channel, which is divided by N to give the HRT in each subcell.

7.3. Experimental Methods

7.3.1. Experimental setup

The FCDI module used in this study has been described previously.[13] Briefly, the module consists of two electrode-channels separated from the central spacer channel by an AEM and a CEM (AEM-Type II/CEM-Type II, FUJIFILM Europe), respectively. The positively and negatively charged electrode slurries exiting the FCDI module are mixed in a stirred tank where oppositely charged AC particles contact each other to become neutral, and the ions adsorbed inside the FCDI module are released. The electrode slurries are pumped through the serpentine channels carved in an acrylic plate. The channels have dimensions of 2 mm × 2 mm × 570 mm (depth × width × length). The effective contact area between the serpentine channels and the IEM is 11.9

cm^2 while the contact area between the current collector and the IEM is equal to 22.0 cm^2. The feedwater is pumped through the spacer-channel for ion removal with the effluent salinity measured continuously using an inline conductivity meter.

7.3.2. Experimental conditions

The flow electrode was prepared by mixing Milli-Q water (18.2 MΩ cm) with different weight percentages of activated carbon powder (2, 5 and 10 wt %). The flow electrode was charged by a DC power supply with different current densities (8.4, 16.8, 25.2 and 33.6 A m^{-2}). The influence of HRT (0.47, 0.69, 0.91 and 1.40 min) on the FCDI performance was investigated by changing the flowrate of feed water running through the spacer channel.

7.3.3. Performance evaluation

The cell voltage, current and conductivity were recorded using corresponding probes (Vernier Software & Technology, Beaverton, OR, USA) connected to a SensorDAQ. The specific energy consumption, SEC, was calculated according to the following equation:

$$SEC = \frac{IAV}{Q(c_0 - c_D)} \tag{7.16}$$

where V is the cell voltage, I is the current density, A is the effective area, Q is the feed flowrate in the spacer-channel and c_0 and c_D are the concentrations of the feed (i.e., the influent) and deionized water (i.e., the effluent) stream, respectively.

Because electro-sorption and electrodialysis both occur in an FCDI process, the quantification of desalination rate is based on average salt removal rate ($ASRR$) instead of the average salt adsorption rate (*ASAR*) as used in a CDI system based on film electrodes.[188, 189] The definition of *ASRR* is the amount of salt removed per area of IEM in a unit time:

$$ASRR = \frac{Q(c_0 - c_D)}{A} \tag{7.17}$$

SEC and *ASRR* values for both experimental data and simulation results were obtained using eqs 16 and 17 with comparison of these values used to evaluate the FCDI performance over a range of experimental conditions.

7.4. Results and Discussion

7.4.1. Experimental results and model validation

A series of FCDI experiments with various operational conditions were conducted to validate the proposed model by fitting the data for effluent concentration and cell voltage/current as a function of time. A value of $N = 8$ is used in this study with a larger number of subcells found to provide no improvement in model fit to the experimental data. The only fitting parameters used were the coefficient γ in eq. 7.14 and the specific equivalent series resistance R_{esr} in eq. 16, which were adjusted to obtain a good fit of the experimentally measured effluent concentration and average current density. The values of the AC properties, such as $C_{St-vol,0}$ and α in eq. 7.13, are reported in the literature.[15, 100, 117, 190] We note that γ and R_{esr} are the only two properties of the FCDI system and these parameters do not depend on operating conditions. Therefore, the same γ and R_{esr} apply to all sceniaros with different operating conditions. Consequently, the FCDI model that is developed here with the fitted γ and R_{esr} can be used for predicting performance at different operating conditions.

Experimentally, the effect of changes in three operating parameters including current density, hydraulic retention time (HRT) and carbon content were examined. In total, four values of current density, four values of spacer channel HRT and three values of carbon loading were studied. The effluent concentrations and cell voltages at various current densities are presented in Figure 7.2. Although SCC FCDI is usually considered a steady-state process, the start-up of an FCDI system is still dynamic. The presence of the IEMs, however, enables an FCDI system to reach a steady-state effluent concentration in a relatively short time with the effluent concentration similar to that achieved in membrane CDI (MCDI).

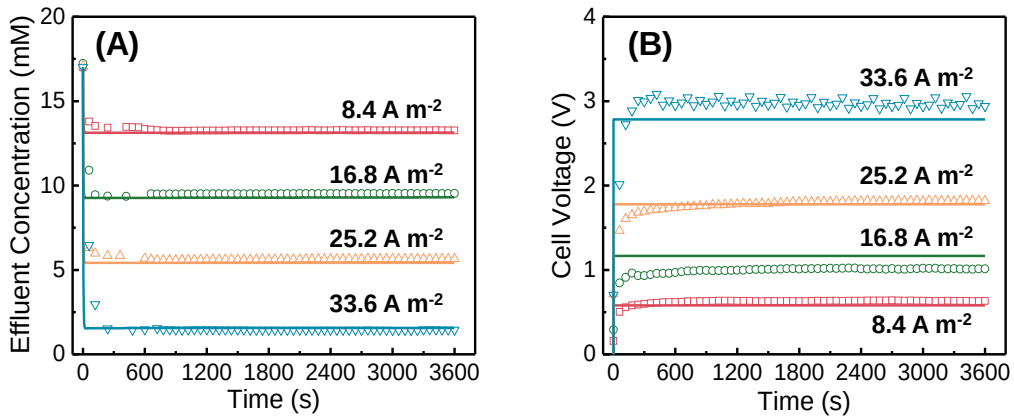

Figure 7.2 Experimental results and model validation for (A) effluent concentration, and (B) cell voltage for continuous FCDI operations over 1 hr. The open symbols in (A) represent concentrations converted from a pre-calibrated in-line conductivity meter. The open symbols in (B) represent the real-time cell voltages. The solid lines in both panels are results simulated with the EFE-FCDI model. This set of experiments was obtained with a FCDI containing 5% (wt/v) of AC and a spacer channel HRT of 0.69 min.

Increasing the current density for the same HRT results in a decrease in the effluent concentration (Figure 7.2A). At relatively high current density (33.6 A m^{-2}), salt rejection as high as 92% was achieved. During the start-up stage, the cell voltage rose sharply to a stable level. Unlike the case of film-electrode CDI in which cell voltage continuously rises over time when the cell is charged at constant current, the cell voltage in SCC FCDI remains stable (Figure 7.2B) because the exhausted AC particles continue to be regenerated outside the FCDI cell. Overall, the results from the EFE-FCDI model are in excellent agreement with the experimental data with this agreement demonstrating the capability of the EFE-FCDI model in predicting the performance of FCDI over a range of operating conditions. Additional fittings of experimental data with the EDF-FCDI model are provided in the Supporting Information (Figure S7.1).

CDI processes based on film electrodes are dynamic, i.e., there are always certain key system parameters that vary temporally. For example, when charging a CDI process at constant voltage (CV), the current density and effluent salinity both change over time due to the temporal variation in the driving force for ion transport. Alternatively, when charging a CDI process at constant current (CC), the cell voltage has to rise over time to offset the build-up of Stern and

Donnan potentials in the EDL, so that a constant driving force for ion transport can be maintained. In contrast, there is no temporal variation of parameters in a FCDI process except for the short start-up stage, even though the same build-up of Stern and Donnan potentials in the EDL of the AC still occur as AC particles flow along the electrode channel and accumulate additional ions in their micropores. In essence, the constant movement of the electrodes converts the temporal variations of the system to spatial variations. The spatial variations of various system properties are illustrated in Figure 7.3. These properties include the volumetric micropore charge density, σ_{mi} (Figure 7.3A), the current density (Figure 7.3B), the salt concentration in the spacer channel and the solution phase of the flow electrode channel (Figure 7.3C) and the Stern and Donnan potentials (Figure 7.3D).

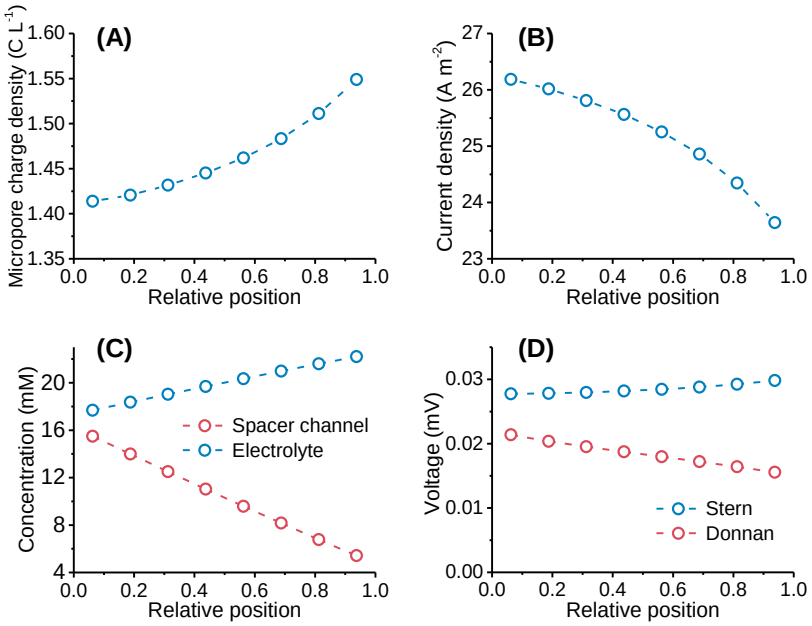

Figure 7.3 Spatial variation of important properties in an FCDI cell obtained from simulation with an overall charging current density of 25.2 A m^{-2} (the corresponding overall voltage is 1.78 V). The spatially-variant properties presented here include (A) micropore charge density, (B) local current density, (C) local salt concentrations in the spacer channel (red) and flow electrode channel (blue, excluding micropores), and (D) local Stern and Donnan potential drops. In this simulation, the AC loading is 5% (w/v) and the HRT of the spacer stream is 0.69 min. The x-axis represents the relative position along the flow direction of the feed water and flow electrode streams.

CDI systems with film electrodes are typically charged using CC or CV mode. The reason for specifying what should be constant is precisely because not all properties can remain temporally constant. Specifically, as charging proceeds, the current diminishes in CV mode while the cell voltage rises in CC mode. For FCDI with a single pair of current collectors, however, everything is temporally constant, and there is only one cell voltage for the FCDI system as a whole. On the other hand, the current density varies spatially along the water flow direction as the water is desalinated (Figure 7.3B). Therefore, referring to an FCDI operation as CC or CV is not meaningful as FCDI always possesses both characteristics. However, if we follow a thin slab of AC slurry in the flow electrode channel, that flowing portion of the electrode has the characteristic of CV charging, as the corresponding current density decreases over time (temporally) and along the electrode channel (spatially) (Figure 7.3B).

To futher illustrate that an FCDI cell has both CC and CV characteristics, we simulate the distribution of potential drops in different components at different positions of the FCDI module (Fig 7.4). In a typical EFE-FCDI model, these potential drops should include seven components including the Stern potential in the micropores, the Donnan potential between the micropores and macropores, the potential drop in the flow electrode chamber (electrode), the potential drop across the IEMs (membrane), the sum of the Donnan potential drops across the two interfaces of the IEMs (mem_Donnan), the potential drop across the spactial channel (spacer) and the potential drop due to the series resistance. However, the results from our simulation suggest that the Stern potential in the micropores and the Donnan potential between the micropores and macropores are both negligible compared to other contributions (Fig 7.3D). As such, these potentials are not included in Fig 7.4.

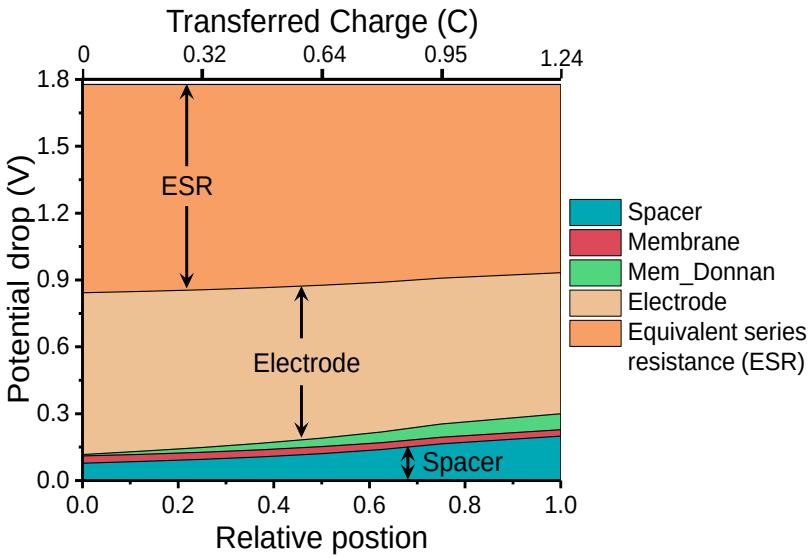

Figure 7.4 Spatial distribution of contributions to potential drop in an FCDI module determined using the EFE-FCDI model. In this simulation, the feed salinity is reduced from 17 mM to 5.4 mM with a spacer-channel HRT of 0.69 min. The cell voltage is 1.78 V and the overall current density is 25.2 A cm^{-2}. The overall cell voltage is divided into seven components as described in the text. However, only five components are presented in this figure because the Stern potential in the micropores and the Donnan potential between the micropores and macropores are comparatively negligible (see figure 3D). The equivalent series resistance (ESR) is a fitting parameter that enables the modelled current density and effluent concentration to match the experimental results at different cell voltages, which are invariant with operational conditions.

Because there can only be one potential for a current collector, the cell voltage is also spatially independent. Therefore, the sum of the all potential drops across the two current collectors is also spatially constant (1.8 V in this case). However, the individual contributions to the overall potential drop vary along the module as more charge is transferred (top axis in Figure 7.4) and more salts are removed from the feed stream. Specifically, the potential drop across the IEMs and the potential drop due to series resistance both decrease as the local current density decreases along the feed stream flow. In addition, the decrease in salt concentration in the spacer channel and increase in the flow electrode channel results in changes in the electrical resistance and thus the potential drop in the respective channels (Figure 7.4).

7.4.2. Performance Evaluation of FCDI

The effects of operating conditions on the FCDI performance metrics were investigated over a wide range of operating conditions using both experimental and modeling approaches. We first investigated the impact of current density on the average salt removal rate, *ASRR*, and specifc energy consumption, *SEC*. As the current density increases from 8.4 to 33.6 A cm^{-2}, *ASRR* increases linearly from 5.0 to 20.9 mmole cm^{-2} min^{-1} (Figure 7.5A). Notably, the *ASRR* of FCDI is higher than the average salt adsorption rate in most MCDI processes (usually lower than 10 mmole cm^{-2} min^{-1}). Increasing current density also results in greater energy consumption. Specifically, *SEC* increases linearly from 0.06 to 0.28 J $\mu mole^{-1}$ when the current density quadrupled from 8.4 to 33.6 A cm^{-2} (Figure 7.5A). These results reflect the intrinsic tradeoff between desalination rate and energy efficiency as discussed in several recent papers[75, 77, 117, 162, 174]. We also note that results from the numerical simulation are in remarkably good agreement with the experimental results.

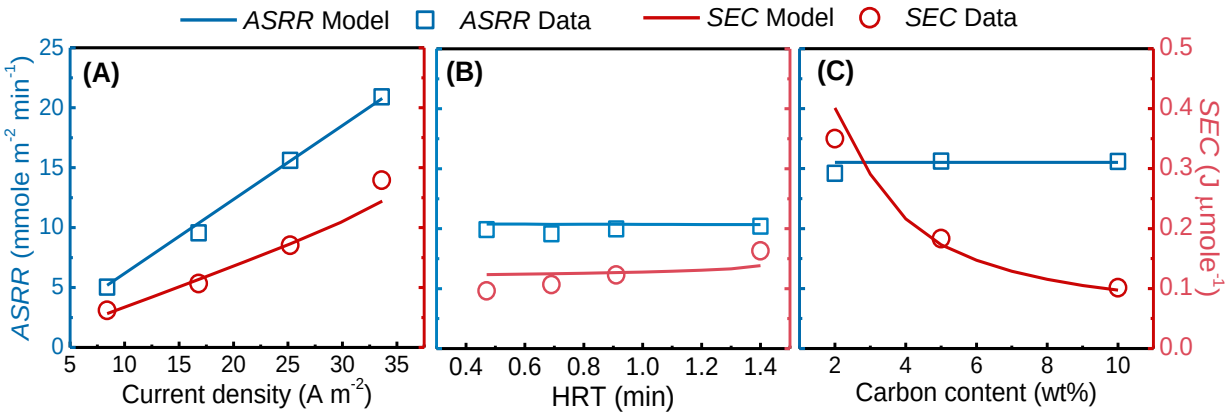

Figure 7.5 Experimental and modelling results of FCDI performance for different operating conditions. The influence of current density (A) was examined when the HRT was set at 0.69 min and the carbon content was 5 wt%. When studying the effects of HRT (B), a current density of 16.8 A m^{-2} was applied to an FCDI cell with carbon content of 5 wt%. Three levels of carbon loading were investigated (C) using a cell voltage of 1.78 V, consequential current density of 25.2 A m^{-2} and HRT of the spacer stream of 0.69 min.

With a fixed current density, increasing HRT results in a reduction in effluent salinity and an increase in salt rejection. However, HRT has a negligible impact on the desalination rate (Figure 7.5B), which is unsurprising because *ASRR* is roughly proportional to current density as long as charge efficiency remains similar. In comparison, the energy consumption is slightly more sensitive to HRT, with *SEC* increasing from 0.10 to 0.16 J $\mu mole^{-1}$ when HRT increases from 0.47 to 1.4 min (Figure 7.5B). The increase in SEC mainly occurs because a longer HRT results in greater reduction of the feed salinity and thus a lower average feed salinity which, in turn, leads to a higher average feed channel resistance and a higher overall cell resistance.

A distinct characteristic of FCDI, as opposed to conventional CDI with film electrodes, is that the carbon content of the electrode is adjustable. Increasing the AC loading from 2 to 10 % results in a significant reduction in *SEC* from 0.35 to 0.10 J $\mu mole^{-1}$ (Figure 7.5C). This improvement in energy efficiency is attributable to the increase of overall conductivity of the flow electrode channel, as the charge transfer is enhanced as more frequent collisions between AC particles occur at higher AC loading. However, the increase of AC loading also comes with the practical disadvantage that circulating the AC slurry in the electrode channel becomes more challenging (i.e., larger pressure drop and more prone to clogging) as the viscosity increases with AC loading. While this practical challenge is not specifically investigated in the current study, the caveats of increasing the carbon content of the flow electrode should not be overlooked in practical system design. On the other hand, increasing the carbon content does not affect the *ASRR* if the current density is maintained the same. From all three series of experiments, it is clear that while *SEC* may depend on operational and system parameters in different ways, the desalination rate is only a function of current density.

7.4.3. The Impact of Carbon Content on System Performacne

To more systematically investigate the impact of carbon content in the flow electrode on the overall system performance, we compare simulated performance tradeoff curves for FCDI systems with different carbon contents in the flow electrode using the experimentally validated model. In all cases, the FCDI system is simulated to reduce the feed concentration of 17 mM to the same effluent concentration of 1.6 mM. The FCDI performance is quantified by performance

tradeoff curves that relate *ASRR* and the inverse of SEC_w (i.e., SEC_w^{-1} vs. *ASRR*) which quantify the kinetic and energetic efficiencies, respectively. The simulated performance tradeoff curves were established by simultaneously varying the applied voltage and the flow rate of the feed stream so that a target effluent concentration of 1.6 mM was always achieved. As a rule-of-thumb, a performance tradeoff curve that is in the upper-right position of a SEC_w^{-1} vs. *ASRR* plot is preferred.

In general, increasing the carbon content leads to kinetically and energetically more favorable FCDI operation (Figure 7.6), mainly due to increased electrical conductivity. The positive impact of increasing the carbon content is particularly salient when the carbon conent is low. For instance, increasing the carbon content from 5% to 10% dramatically enhances the energy efficiency, SEC_w^{-1}, especially in the high *ASRR* range. However, further increasing the carbon content from 10% to 15%, by the same increment of 5%, has a considerably smaller effect in further enhancing the energetic and kinetic efficiencies. The dwindling impact of increasing carbon content when the carbon content is releatively high can be explained by the inverse relationship between electrical resistance and electrical conductivity; i.e., increasing the electrical conductivity has a much stronger effect in reducing the electrical resistance when the electrical conductivity is low compared to the effect when it is high. A flow electrode with high carbon content becomes more viscous and prone to clogging the electrode channel, which increases the pumping energy for circulation (not considered in this analysis) and renders practical FCDI operation considerably more challenging. Considering the significant detrimental impacts on operation and diminishing return on reducing flow channel resistanceof increasing carbon content, the carbon content in the flow electrode should be limited to a certain level. While the accurate optimization of carbon content is beyond the scope of this study, it must incorporate the key elements of the analysis presented here as well as accounting for the circulation energy cost as a function of carbon content.

7.5. Conclusions

While the microscopic behavior of the flow electrodes in FCDI is very complex and requires multi-phase hydrodynamic modeling for full elucidation, we have demonstrated in this work that the system level behavior of FCDI can be satisfactorily described using an equivalent film electrode (EFE) model where the flow electrode is simply treated as a moving film electrode.

Not only does the EFE model yield a very good description of the experimental data, it can also be employed for performance prediction because the model does not have any operation-specific fitting parameters. As such, the EFE-FCDI model can be employed for designing and optimizing FCDI systems. It can also be used for theoretical investigation to enhance our fundamental understanding of FCDI because it enables the analysis of the spatial distribution of the important properties in the FCDI cell and the breakdown of energy loss in different parts of the system. Last but not least, we show that increasing the carbon content in the flow electrode has a strong positive impact only when the carbon content is low - an important insight for design of cost-effective FCDI systems.

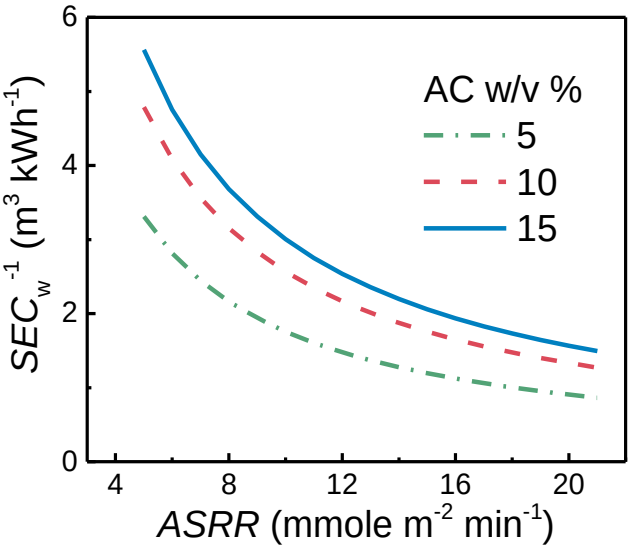

Figure 7.6 Model simulation of SEC_w^{-1} and *ASRR* tradeoff curves for achieving the same effluent concentration with different carbon loading in the flow electrode channel. The feed concentration is reduced from 17 mM to 1.62 mM. On each tradeoff curve, the current density/cell voltage, charging duration and feed channel flow rate are all adjusted simultaneously to achieve the same target effluent concentration.

CHAPTER 8

CONCLUSIONS

In this study, we investigated the CDI energy efficiency, evaluated the performance and modelled the processes at different scales. Based on modified Donnan model, a thermodynamic reversible processes was proposed for CDI, which demonstrated that such processes consumed the Gibbs free energy of separation (*Chapter 2*). By employing the thermodynamic reversible processes as a caliber as it stipulated the minimum energy that was required to realize the corresponding separation, we surveyed the published data on CDI and evaluated their efficiency by comparing the actual energy consumption to the Gibbs free energy of separation (*Chapter 3*). In addition, we analyzed the energy breakdowns for the charging and discharge steps of the CDI operation, to identify the major energy losses. We also elucidated that the energy efficiency is also related to the kinetics of the processes. Inspired by this finding, we quantified the tradeoff between the energy efficiency and kinetic efficiency for CDI, which presented a fair and valuable tool to evaluate the performances of various processes and to compare different CDI cells achieving the same separation (*Chapter 4*). With the tool of the tradeoff, we demonstrated the application of the tradeoff in comparing the two common charging methods of CDI (i.e. constant current and constant voltage charging), and found that there was no general conclusion about the superiority of one method over the other, but depended on the target separation (*Chapter 5*). Based on the energy breakdowns generated in Chapter 3, we revealed that the resistance of macropores of the carbon electrodes contributed significantly to the overall energy consumption, which lead us to infiltrate the activated carbon cloth with ion-conductive polyelectrolyte (*Chapter 6*). In this respective study, we demonstrated that the polyelectrolyte-infiltrated CDI (πCDI) behaved much more energetically efficient than the conventional membrane CDI (MCDI). The conventional CDI process was operated intermittently and the salt rejection was limited. The flow electrode CDI (FCDI) was recently developed to address such challenges. An equivalent-film electrode model was developed to study the performances of FCDI (*Chapter 7*). We found out that the developed model was able to predict the FCDI process. It also enabled analysis of the spatial distribution of

the properties of FCDI system as well as the energy breakdowns. Simply put, we advanced the understandings of the CDI processes from the energetic and kinetic perspectives, and introduced approaches to enhance the performances of CDI for possible scale-up.

REFERENCES

1. Porada, S.; Zhao, R.; van der Wal, A.; Presser, V.; Biesheuvel, P. M., Review on the science and technology of water desalination by capacitive deionization. *Prog Mater Sci* **2013,** *58*, (8), 1388-1442.

2. Biesheuvel, P. M.; van Limpt, B.; van der Wal, A., Dynamic Adsorption/Desorption Process Model for Capacitive Deionization. *J Phys Chem C* **2009,** *113*, (14), 5636-5640.

3. Seleym, A.; Elshafei, M., A New Energy-Efficient Topology for Solar-Powered Capacitive Deionization Systems. *Ieee Electr Pow Ener* **2017**, 7-12.

4. Mossad, M.; Zhang, W.; Zou, L., Using capacitive deionisation for inland brackish groundwater desalination in a remote location. *Desalination* **2013,** *308*, 154-160.

5. Seo, S.-J.; Jeon, H.; Lee, J. K.; Kim, G.-Y.; Park, D.; Nojima, H.; Lee, J.; Moon, S.-H., Investigation on removal of hardness ions by capacitive deionization (CDI) for water softening applications. *Water Res* **2010,** *44*, (7), 2267-2275.

6. Zuo, K.; Kim, J.; Jain, A.; Wang, T.; Verduzco, R.; Long, M.; Li, Q., Novel Composite Electrodes for Selective Removal of Sulfate by the Capacitive Deionization Process. *Environ Sci Technol* **2018,** *52*, (16), 9486.

7. Tang, W. W.; Kovalsky, P.; Cao, B. C.; He, D.; Waite, T. D., Fluoride Removal from Brackish Groundwaters by Constant Current Capacitive Deionization (CDI). *Environ Sci Technol* **2016,** *50*, (19), 10570-10579.

8. Anderson, M. A.; Cudero, A. L.; Palma, J., Capacitive deionization as an electrochemical means of saving energy and delivering clean water. Comparison to present desalination practices: Will it compete? *Electrochim Acta* **2010,** *55*, (12), 3845-3856.

9. Zhao, R.; Porada, S.; Biesheuvel, P. M.; Van der Wal, A., Energy consumption in membrane capacitive deionization for different water recoveries and flow rates, and comparison with reverse osmosis. *Desalination* **2013,** *330*, 35-41.

10. Biesheuvel, P. M.; Zhao, R.; Porada, S.; van der Wal, A., Theory of membrane capacitive deionization including the effect of the electrode pore space. *Journal of colloid and interface science* **2011,** *360*, (1), 239-248.

11. Zhao, R.; Biesheuvel, P. M.; van der Wal, A., Energy consumption and constant current operation in membrane capacitive deionization. *Energ Environ Sci* **2012,** *5*, (11), 9520-9527.

12. Tang, W. W.; He, D.; Zhang, C. Y.; Kovalsky, P.; Waite, T. D., Comparison of Faradaic reactions in capacitive deionization (CDI) and membrane capacitive deionization (MCDI) water treatment processes. *Water Res* **2017,** *120*, 229-237.

13. Zhao, R.; Biesheuvel, P. M.; Miedema, H.; Bruning, H.; van der Wal, A., Charge Efficiency: A Functional Tool to Probe the Double-Layer Structure Inside of Porous Electrodes

and Application in the Modeling of Capacitive Deionization. *J Phys Chem Lett* **2010,** *1*, (1), 205-210.

14. Biesheuvel, P. M.; Bazant, M. Z., Nonlinear dynamics of capacitive charging and desalination by porous electrodes. *Phys Rev E* **2010,** *81*, (3).

15. Qu, Y. T.; Campbell, P. G.; Hemmatifar, A.; Knipe, J. M.; Loeb, C. K.; Reidy, J. J.; Hubert, M. A.; Stadermann, M.; Santiago, J. G., Charging and Transport Dynamics of a Flow-Through Electrode Capacitive Deionization System. *J Phys Chem B* **2018,** *122*, (1), 240-249.

16. Suss, M. E.; Baumann, T. F.; Bourcier, W. L.; Spadaccini, C. M.; Rose, K. A.; Santiago, J. G.; Stadermann, M., Capacitive desalination with flow-through electrodes. *Energ Environ Sci* **2012,** *5*, (11), 9511-9519.

17. Porada, S.; Sales, B. B.; Hamelers, H. V. M.; Biesheuvel, P. M., Water Desalination with Wires. *J Phys Chem Lett* **2012,** *3*, (12), 1613-1618.

18. Ramachandran, A.; Oyarzun, D. I.; Hawks, S. A.; Stadermann, M.; Santiago, J. G., High water recovery and improved thermodynamic efficiency for capacitive deionization using variable flowrate operation. *Water Res* **2019,** *155*, 76-85.

19. Lee, J.; Kim, S.; Kim, C.; Yoon, J., Hybrid capacitive deionization to enhance the desalination performance of capacitive techniques. *Energ Environ Sci* **2014,** *7*, (11), 3683-3689.

20. Ji, F.; Wang, L.; Yang, J. S.; Wu, X.; Li, M. Q.; Jiang, S. L.; Lin, S. H.; Chen, Z., Highly compact, free- standing porous electrodes from polymer- derived nanoporous carbons for efficient electrochemical capacitive deionization. *J Mater Chem A* **2019,** *7*, (4), 1768-1778.

21. Oren, Y., Capacitive delonization (CDI) for desalination and water treatment - past, present and future (a review). *Desalination* **2008,** *228*, (1-3), 10-29.

22. Farmer, J. C.; Fix, D. V.; Mack, G. V.; Pekala, R. W.; Poco, J. F., Capacitive deionization of NaCl and NaNO3 solutions with carbon aerogel electrodes. *J Electrochem Soc* **1996,** *143*, (1), 159-169.

23. Porada, S.; Weingarth, D.; Hamelers, H. V. M.; Bryjak, M.; Presser, V.; Biesheuvel, P. M., Carbon flow electrodes for continuous operation of capacitive deionization and capacitive mixing energy generation. *J Mater Chem A* **2014,** *2*, (24), 9313-9321.

24. Jeon, S. I.; Park, H. R.; Yeo, J. G.; Yang, S.; Cho, C. H.; Han, M. H.; Kim, D. K., Desalination via a new membrane capacitive deionization process utilizing flow-electrodes. *Energ Environ Sci* **2013,** *6*, (5), 1471-1475.

25. Bejan, A., *Advanced Engineering Thermodynamics*. 2nd ed.; Wiley: 1997; p 850.

26. Spiegler, K. S.; El-Sayed, Y. M., The energetics of desalination processes. *Desalination* **2001,** *134*, (1-3), 109-128.

27. Elimelech, M.; Phillip, W. A., The Future of Seawater Desalination: Energy, Technology, and the Environment. *Science* **2011,** *333*, (6043), 712-717.

28. Zhu, A. Z.; Christofides, P. D.; Cohen, Y., Effect of Thermodynamic Restriction on Energy Cost Optimization of RO Membrane Water Desalination. *Ind Eng Chem Res* **2009,** *48*, (13), 6010-6021.

29. Biesheuvel, P. M., Thermodynamic cycle analysis for capacitive deionization. *Journal of colloid and interface science* **2009,** *332*, (1), 258-264.

30. Verwey, E. J.; Overbeek, J. T. G., *Theory of the stability of Lyophobic Colloids*. Dover Publications: 1999.

31. Hunter, R. J., *Foundations of Colloid Science*. 2nd Edition ed.; Oxford University Press: 2001; p 816.

32. Lin, C.; Ritter, J. A.; Popov, B. N., Correlation of double-layer capacitance with the pore structure of sol-gel derived carbon xerogels. *J Electrochem Soc* **1999,** *146*, (10), 3639-3643.

33. Porada, S.; Weinstein, L.; Dash, R.; van der Wal, A.; Bryjak, M.; Gogotsi, Y.; Biesheuvel, P. M., Water Desalination Using Capacitive Deionization with Microporous Carbon Electrodes. *Acs Appl Mater Inter* **2012,** *4*, (3), 1194-1199.

34. Sandler, S. I., *Chemical, Biochemical and Engineering Thermodynamics*. 4 th ed.; Wiley: 2006.

35. Porada, S.; Borchardt, L.; Oschatz, M.; Bryjak, M.; Atchison, J. S.; Keesman, K. J.; Kaskel, S.; Biesheuvel, P. M.; Presser, V., Direct prediction of the desalination performance of porous carbon electrodes for capacitive deionization. *Energ Environ Sci* **2013,** *6*, (12), 3700-3712.

36. Biesheuvel, P. M.; Porada, S.; Levi, M.; Bazant, M. Z., Attractive forces in microporous carbon electrodes for capacitive deionization. *J Solid State Electr* **2014,** *18*, (5), 1365-1376.

37. Biesheuvel, P. M.; Hamelers, H. V. M.; Suss, M. E., Theory of Water Desalination by Porous Electrodes with Immobile Chemical Charge. *Colloid Interfac Sci* **2015,** *9*, 1-5.

38. Bonthuis, D. J.; Gekle, S.; Netz, R. R., Dielectric Profile of Interfacial Water and its Effect on Double-Layer Capacitance. *Phys Rev Lett* **2011,** *107*, (16).

39. Bazant, M. Z.; Chu, K. T.; Bayly, B. J., Current-voltage relations for electrochemical thin films. *Siam J Appl Math* **2005,** *65*, (5), 1463-1484.

40. Smith, K. C., Theoretical evaluation of electrochemical cell architectures using cation intercalation electrodes for desalination. *Electrochim Acta* **2017,** *230*, 333-341.

41. Pasta, M.; Wessells, C. D.; Cui, Y.; La Mantia, F., A Desalination Battery. *Nano Lett* **2012,** *12*, (2), 839-843.

42. J, H.; R, Q.; G, F.; BG, S.; V, M., *Modern Theories of Carbon-Based Electrochemical Capacitors*. Wiley: New York, 2013.

43. Kim, T.; Dykstra, J. E.; Porada, S.; van der Wal, A.; Yoon, J.; Biesheuvel, P. M., Enhanced charge efficiency and reduced energy use in capacitive deionization by increasing the discharge voltage. *Journal of colloid and interface science* **2015,** *446*, 317-326.

44. Li, M. H., Reducing specific energy consumption in Reverse Osmosis (RO) water desalination: An analysis from first principles. *Desalination* **2011,** *276*, (1-3), 128-135.

45. Lin, S. H.; Elimelech, M., Kinetics and energetics trade-off in reverse osmosis desalination with different configurations. *Desalination* **2017,** *401*, 42-52.

46. Yip, N. Y.; Elimelech, M., Thermodynamic and Energy Efficiency Analysis of Power Generation from Natural Salinity Gradients by Pressure Retarded Osmosis. *Environ Sci Technol* **2012,** *46*, (9), 5230-5239.

47. Arnold, B. B.; Murphy, G. W., Studies on Electrochemistry of Carbon and Chemically Modified Carbon Surfaces. *J Phys Chem-Us* **1961,** *65*, (1), 135-&.

48. Murphy, G. W.; Caudle, D. D., Mathematical Theory of Electrochemical Demineralization in Flowing Systems. *Electrochim Acta* **1967,** *12*, (12), 1655-&.

49. Ma, J. X.; He, D.; Tang, W. W.; Kovalsky, P.; He, C.; Zhang, C. Y.; Waite, T. D., Development of Redox-Active Flow Electrodes for High-Performance Capacitive Deionization. *Environ Sci Technol* **2016,** *50*, (24), 13495-13501.

50. Peng, Z.; Zhang, D. S.; Shi, L. Y.; Yan, T. T., High performance ordered mesoporous carbon/carbon nanotube composite electrodes for capacitive deionization. *J Mater Chem* **2012,** *22*, (14), 6603-6612.

51. Wang, H.; Zhang, D. S.; Yan, T. T.; Wen, X. R.; Zhang, J. P.; Shi, L. Y.; Zhong, Q. D., Three-dimensional macroporous graphene architectures as high performance electrodes for capacitive deionization. *J Mater Chem A* **2013,** *1*, (38), 11778-11789.

52. Zhang, D. S.; Yan, T. T.; Shi, L. Y.; Peng, Z.; Wen, X. R.; Zhang, J. P., Enhanced capacitive deionization performance of graphene/carbon nanotube composites. *J Mater Chem* **2012,** *22*, (29), 14696-14704.

53. Kruner, B.; Srimuk, P.; Fleischmann, S.; Zeiger, M.; Schreiber, A.; Asian, M.; Quade, A.; Presser, V., Hydrogen-treated, sub-micrometer carbon beads for fast capacitive deionization with high performance stability. *Carbon* **2017,** *117*, 46-54.

54. Srimuk, P.; Lee, J.; Fleischmann, S.; Choudhury, S.; Jackel, N.; Zeiger, M.; Kim, C.; Aslan, M.; Presser, V., Faradaic deionization of brackish and sea water via pseudocapacitive cation and anion intercalation into few-layered molybdenum disulfide. *J Mater Chem A* **2017,** *5*, (30), 15640-15649.

55. Jain, A.; Kim, J.; Owoseni, O. M.; Weathers, C.; Cana, D.; Zuo, K. C.; Walker, W. S.; Li, Q. L.; Verduzco, R., Aqueous-Processed, High-Capacity Electrodes for Membrane Capacitive Deionization. *Environ Sci Technol* **2018,** *52*, (10), 5859-5867.

56. Tsouris, C.; Mayes, R.; Kiggans, J.; Sharma, K.; Yiacoumi, S.; DePaoli, D.; Dai, S., Mesoporous Carbon for Capacitive Deionization of Saline Water. *Environ Sci Technol* **2011,** *45*, (23), 10243-10249.

57. Li, H. B.; Zou, L. D.; Pan, L. K.; Sun, Z., Novel Graphene-Like Electrodes for Capacitive Deionization. *Environ Sci Technol* **2010,** *44*, (22), 8692-8697.

58. Ahualli, S.; Iglesias, G. R.; Fernandez, M. M.; Jimenez, M. L.; Delgado, A. V., Use of Soft Electrodes in Capacitive Deionization of Solutions. *Environ Sci Technol* **2017,** *51*, (9), 5326-5333.

59. Omosebi, A.; Gao, X.; Landon, J.; Liu, K. L., Asymmetric Electrode Configuration for Enhanced Membrane Capacitive Deionization. *Acs Appl Mater Inter* **2014,** *6*, (15), 12640-12649.

60. Hatzell, K. B.; Fan, L.; Beidaghi, M.; Boota, M.; Pomerantseva, E.; Kumbur, E. C.; Gogotsi, Y., Composite Manganese Oxide Percolating Networks As a Suspension Electrode for an Asymmetric Flow Capacitor. *Acs Appl Mater Inter* **2014,** *6*, (11), 8886-8893.

61. Garcia-Quismondo, E.; Santos, C.; Soria, J.; Palma, J.; Anderson, M. A., New Operational Modes to Increase Energy Efficiency in Capacitive Deionization Systems. *Environ Sci Technol* **2016,** *50*, (11), 6053-6060.

62. Kim, C.; Srimuk, P.; Lee, J.; Aslan, M.; Presser, V., Semi-continuous capacitive deionization using multi-channel flow stream and ion exchange membranes. *Desalination* **2018,** *425*, 104-110.

63. Cho, Y.; Lee, K. S.; Yang, S.; Choi, J.; Park, H. R.; Kim, D. K., A novel three-dimensional desalination system utilizing honeycomb-shaped lattice structures for flow-electrode capacitive deionization. *Energ Environ Sci* **2017,** *10*, (8), 1746-1750.

64. Yang, S.; Choi, J.; Yeo, J. G.; Jeon, S. I.; Park, H. R.; Kim, D. K., Flow-Electrode Capacitive Deionization Using an Aqueous Electrolyte with a High Salt Concentration. *Environ Sci Technol* **2016,** *50*, (11), 5892-5899.

65. Gao, X.; Omosebi, A.; Landon, J.; Liu, K. L., Enhanced Salt Removal in an Inverted Capacitive Deionization Cell Using Amine Modified Microporous Carbon Cathodes. *Environ Sci Technol* **2015,** *49*, (18), 10920-10926.

66. He, C.; Ma, J.; Zhang, C.; Song, J.; Waite, T. D., Short-Circuited Closed-Cycle Operation of Flow-Electrode CDI for Brackish Water Softening. *Environ Sci Technol* **2018,** *52*, (16), 9350-9360.

67. Hatzell, K. B.; Hatzell, M. C.; Cook, K. M.; Boota, M.; Housel, G. M.; McBride, A.; Kumbur, E. C.; Gogotsi, Y., Effect of Oxidation of Carbon Material on Suspension Electrodes for Flow Electrode Capacitive Deionization. *Environ Sci Technol* **2015,** *49*, (5), 3040-3047.

68. Gao, X.; Porada, S.; Omosebi, A.; Liu, K. L.; Biesheuvel, P. M.; Landon, J., Complementary surface charge for enhanced capacitive deionization. *Water Res* **2016,** *92*, 275-282.

69. Qu, Y. T.; Baumann, T. F.; Santiago, J. G.; Stadermann, M., Characterization of Resistances of a Capacitive Deionization System. *Environ Sci Technol* **2015,** *49*, (16), 9699-9706.

70. Suss, M. E.; Biesheuvel, P. M.; Baumann, T. F.; Stadermann, M.; Santiago, J. G., In Situ Spatially and Temporally Resolved Measurements of Salt Concentration between Charging Porous

Electrodes for Desalination by Capacitive Deionization. *Environ Sci Technol* **2014,** *48*, (3), 2008-2015.

71. Zhao, R.; Satpradit, O.; Rijnaarts, H. H. M.; Biesheuvel, P. M.; van der Wal, A., Optimization of salt adsorption rate in membrane capacitive deionization. *Water Res* **2013,** *47*, (5), 1941-1952.

72. Wang, L.; Lin, S. H., Membrane Capacitive Deionization with Constant Current vs Constant Voltage Charging: Which Is Better? *Environ Sci Technol* **2018,** *52*, (7), 4051-4060.

73. Hemmatifar, A.; Stadermann, M.; Santiago, J. G., Two-Dimensional Porous Electrode Model for Capacitive Deionization. *J Phys Chem C* **2015,** *119*, (44), 24681-24694.

74. Dlugolecki, P.; van der Wal, A., Energy Recovery in Membrane Capacitive Deionization. *Environ Sci Technol* **2013,** *47*, (9), 4904-4910.

75. Hemmatifar, A.; Ramachandran, A.; Liu, K.; Oyarzun, D. I.; Bazant, M. Z.; Santiago, J. G., Thermodynamics of Ion Separation by Electrosorption. *Environ Sci Technol* **2018**.

76. Suss, M. E.; Porada, S.; Sun, X.; Biesheuvel, P. M.; Yoon, J.; Presser, V., Water desalination via capacitive deionization: what is it and what can we expect from it? *Energ Environ Sci* **2015,** *8*, (8), 2296-2319.

77. Hawks, S. A.; Ramachandran, A.; Porada, S.; Campbell, P. G.; Suss, M. E.; Biesheuvel, P. M.; Santiago, J. G.; Stadermann, M., Performance Metrics for the Objective Assessment of Capacitive Deionization Systems. *Water Res* **2018**.

78. Fritzmann, C.; Lowenberg, J.; Wintgens, T.; Melin, T., State-of-the-art of reverse osmosis desalination. *Desalination* **2007,** *216*, (1-3), 1-76.

79. Zhao, D. F.; Xue, J. L.; Li, S.; Sun, H.; Zhang, Q. D., Theoretical analyses of thermal and economical aspects of multi-effect distillation desalination dealing with high-salinity wastewater. *Desalination* **2011,** *273*, (2-3), 292-298.

80. Smith, J. M.; Van Ness, H. C.; Abbott, M. M., *Introduction to Chemical Engineering Thermodynamics*. 7th ed.; McGraw-Hil: Boston, MA, 2005.

81. Lee, J.; Kim, S.; Yoon, J., Rocking Chair Desalination Battery Based on Prussian Blue Electrodes. *Acs Omega* **2017,** *2*, (4), 1653-1659.

82. Wang, L.; Biesheuvel, P. M.; Lin, S., Reversible Thermodynamic Cycle Analysis for Capacitive Deionization with Modified Donnan Model. *Journal of colloid and interface science* **2017**.

83. Kang, J.; Kim, T.; Shin, H.; Lee, J.; Ha, J. I.; Yoon, J., Direct energy recovery system for membrane capacitive deionization. *Desalination* **2016,** *398*, 144-150.

84. Kim, Y. J.; Choi, J. H., Enhanced desalination efficiency in capacitive deionization with an ion-selective membrane. *Sep Purif Technol* **2010,** *71*, (1), 70-75.

85. Lee, J. H.; Bae, W. S.; Choi, J. H., Electrode reactions and adsorption/desorption performance related to the applied potential in a capacitive deionization process. *Desalination* **2010,** *258*, (1-3), 159-163.

86. Kang, J.; Kim, T.; Jo, K.; Yoon, J., Comparison of salt adsorption capacity and energy consumption between constant current and constant voltage operation in capacitive deionization. *Desalination* **2014,** *352*, 52-57.

87. Kim, S.; Lee, J.; Kim, C.; Yoon, J., Na2FeP2O7 as a Novel Material for Hybrid Capacitive Deionization. *Electrochim Acta* **2016,** *203*, 265-271.

88. Liu, Y. H.; Hsi, H. C.; Li, K. C.; Hou, C. H., Electrodeposited Manganese Dioxide/Activated Carbon Composite As a High-Performance Electrode Material for Capacitive Deionization. *Acs Sustain Chem Eng* **2016,** *4*, (9), 4762-4770.

89. Gao, X.; Omosebi, A.; Landon, J.; Liu, K. L., Surface charge enhanced carbon electrodes for stable and efficient capacitive deionization using inverted adsorption-desorption behavior. *Energ Environ Sci* **2015,** *8*, (3), 897-909.

90. Kim, T.; Gorski, C. A.; Logan, B. E., Low Energy Desalination Using Battery Electrode Deionization. *Environ Sci Tech Let* **2017,** *4*, (10), 444-449.

91. Choi, S.; Chang, B.; Kim, S.; Lee, J.; Yoon, J.; Choi, J. W., Battery Electrode Materials with Omnivalent Cation Storage for Fast and Charge-Efficient Ion Removal of Asymmetric Capacitive Deionization. *Adv Funct Mater* **2018,** *28*, (35).

92. Shi, W.; Zhou, X.; Li, J.; Meshot, E. R.; Taylor, A. D.; Hu, S.; Kim, J.-H.; Elimelech, M.; Plata, D. L., High-Performance Capacitive Deionization via Manganese Oxide-Coated, Vertically Aligned Carbon Nanotubes. *Environ Sci Tech Let* **2018,** *5*, (11), 692-700.

93. Wu, T. T.; Wang, G.; Wang, S. Y.; Zhan, F.; Fu, Y.; Qiao, H. Y.; Qiu, J. S., Highly Stable Hybrid Capacitive Deionization with a MnO2 Anode and a Positively Charged Cathode. *Environ Sci Tech Let* **2018,** *5*, (2), 98-102.

94. Hand, S.; Cusick, R. D., Characterizing the Impacts of Deposition Techniques on the Performance of MnO2 Cathodes for Sodium Electrosorption in Hybrid Capacitive Deionization. *Environ Sci Technol* **2017,** *51*, (20), 12027-12034.

95. Chen, F. M.; Huang, Y. X.; Guo, L.; Sun, L. F.; Wang, Y.; Yang, H. Y., Dual-ions electrochemical deionization: a desalination generator. *Energ Environ Sci* **2017,** *10*, (10), 2081-2089.

96. Porada, S.; Shrivastava, A.; Bukowska, P.; Biesheuvel, P. M.; Smith, K. C., Nickel Hexacyanoferrate Electrodes for Continuous Cation Intercalation Desalination of Brackish Water. *Electrochim Acta* **2017,** *255*, 369-378.

97. Qin, M.; Deshmukh, A.; Epsztein, R.; Patel, S. K.; Owoseni, O. M.; Walker, W. S.; Elimelech, M., Comparison of energy consumption in desalination by capacitive deionization and reverse osmosis. *Desalination* **2019,** *455*, 100-114.

98. Han, L. C.; Karthikeyan, K. G.; Gregory, K. B., Energy Consumption and Recovery in Capacitive Deionization Using Nanoporous Activated Carbon Electrodes. *J Electrochem Soc* **2015,** *162*, (12), E282-E288.

99. Alkuran, M.; Orabi, M., Utilization of a buck boost converter and the method of segmented capacitors in a CDI water purification system. *2008 12th International Middle East Power System Conference, Vols 1 and 2* **2008**, 89-+.

100. Dykstra, J. E.; Zhao, R.; Biesheuvel, P. M.; van der Wal, A., Resistance identification and rational process design in Capacitive Deionization. *Water Res* **2016,** *88*, 358-370.

101. Hemmatifar, A.; Palko, J. W.; Stadermann, M.; Santiago, J. G., Energy breakdown in capacitive deionization. *Water Res* **2016,** *104*, 303-311.

102. Dykstra, J. E.; Porada, S.; van der Wal, A.; Biesheuvel, P. M., Energy consumption in capacitive deionization - Constant current versus constant voltage operation. *Water Res* **2018,** *143*, 367-375.

103. Dykstra, J. E. Desalination with porous electrodes : mechanisms of ion transport and adsorption. Wageningen University, Wageningen, the Netherlands, 2018.

104. Garcia-Quismondo, E.; Gomez, R.; Vaquero, F.; Cudero, A. L.; Palma, J.; Anderson, M., New testing procedures of a capacitive deionization reactor. *Phys Chem Chem Phys* **2013,** *15*, (20), 7648-7656.

105. Shanbhag, S.; Whitacre, J. F.; Mauter, M. S., The Origins of Low Efficiency in Electrochemical De-Ionization Systems. *J Electrochem Soc* **2016,** *163*, (14), E363-E371.

106. Zhang, C. Y.; He, D.; Ma, J. X.; Tang, W. W.; Waite, T. D., Faradaic reactions in capacitive deionization (CDI) - problems and possibilities: A review. *Water Res* **2018,** *128*, 314-330.

107. Suss, M. E.; Presser, V., Water Desalination with Energy Storage Electrode Materials. *Joule* **2018,** *2*, (1), 10-15.

108. Hwang, J. Y.; Myung, S. T.; Sun, Y. K., Sodium-ion batteries: present and future. *Chem Soc Rev* **2017,** *46*, (12), 3529-3614.

109. Smith, K. C.; Dmello, R., Na-Ion Desalination (NID) Enabled by Na-Blocking Membranes and Symmetric Na-Intercalation: Porous-Electrode Modeling. *J Electrochem Soc* **2016,** *163*, (3), A530-A539.

110. Singh, K.; Porada, S.; de Gier, H. D.; Biesheuvel, P. M.; de Smet, L. C. P. M., Timeline on the application of intercalation materials in Capacitive Deionization. *Desalination* **2018**, 21.

111. Singh, K.; Bouwmeester, H. J. M.; de Smet, L. C. P. M.; Bazant, M. Z.; Biesheuvel, P. M., Theory of Water Desalination with Intercalation Materials. *Phys Rev Appl* **2018,** *9*, (6).

112. Wei, W. F.; Cui, X. W.; Chen, W. X.; Ivey, D. G., Manganese oxide-based materials as electrochemical supercapacitor electrodes. *Chem Soc Rev* **2011,** *40*, (3), 1697-1721.

113. Li, Q.; Wang, Z. L.; Li, G. R.; Guo, R.; Ding, L. X.; Tong, Y. X., Design and Synthesis of MnO2/Mn/MnO2 Sandwich-Structured Nanotube Arrays with High Supercapacitive Performance for Electrochemical Energy Storage. *Nano Lett* **2012,** *12*, (7), 3803-3807.

114. West, K.; Jacobsen, T.; Atlung, S., Modeling of Porous Insertion Electrodes with Liquid Electrolyte. *J Electrochem Soc* **1982,** *129*, (7), 1480-1485.

115. Conway, B. E.; Gileadi, E., Kinetic Theory of Pseudo-Capacitance and Electrode Reactions at Appreciable Surface Coverage. *T Faraday Soc* **1962,** *58*, (Dec), 2493-&.

116. Zhu, A. H.; Christofides, P. D.; Cohen, Y., Energy Consumption Optimization of Reverse Osmosis Membrane Water Desalination Subject to Feed Salinity Fluctuation. *Ind Eng Chem Res* **2009,** *48*, (21), 9581-9589.

117. Wang, L.; Lin, S. H., Intrinsic tradeoff between kinetic and energetic efficiencies in membrane capacitive deionization. *Water Res* **2018,** *129*, 394-401.

118. Cohen, I.; Avraham, E.; Noked, M.; Soffer, A.; Aurbach, D., Enhanced Charge Efficiency in Capacitive Deionization Achieved by Surface-Treated Electrodes and by Means of a Third Electrode. *J Phys Chem C* **2011,** *115*, (40), 19856-19863.

119. Avraham, E.; Noked, M.; Bouhadana, Y.; Soffer, A.; Aurbach, D., Limitations of charge efficiency in capacitive deionization processes III: The behavior of surface oxidized activated carbon electrodes. *Electrochim Acta* **2010,** *56*, (1), 441-447.

120. Avraham, E.; Noked, M.; Bouhadana, Y.; Soffer, A.; Aurbach, D., Limitations of Charge Efficiency in Capacitive Deionization II. On the Behavior of CDI Cells Comprising Two Activated Carbon Electrodes. *J Electrochem Soc* **2009,** *156*, (10), P157-P162.

121. Gao, X.; Omosebi, A.; Landon, J.; Liu, K. L., Enhancement of charge efficiency for a capacitive deionization cell using carbon xerogel with Modified potential of zero charge. *Electrochem Commun* **2014,** *39*, 22-25.

122. Hawks, S. A.; Knipe, J. M.; Campbell, P. G.; Loeb, C. K.; Hubert, M. A.; Santiago, J. G.; Stadermann, M., Quantifying the flow efficiency in constant-current capacitive deionization. *Water Res* **2018,** *129*, 327-336.

123. Johnson, A. M.; Newman, J., Desalting by Means of Porous Carbon Electrodes. *J Electrochem Soc* **1971,** *118*, (3), 510-&.

124. Biesheuvel, P. M.; Bazant, M. Z.; Cusick, R. D.; Hatton, T. A.; Hatzell, M. C.; Hatzell, K. B.; Liang, P.; Lin, S.; Porada, S.; Santiago, J. G.; Smith, K. C.; Stadermann, M.; Su, X.; Sun, X.; Waite, T. D.; van der Wal, A.; Yoon, J.; Zhao, R.; Zou, L.; Suss, M. E., Capacitive Deionization -- defining a class of desalination technologies. *arXiv Applied Physics* **2017**.

125. Welgemoed, T. J.; Schutte, C. F., Capacitive Deionization Technology™: An alternative desalination solution. *Desalination* **2005,** *183*, (1-3), 327-340.

126. Forrestal, C.; Xu, P.; Ren, Z. Y., Sustainable desalination using a microbial capacitive desalination cell. *Energ Environ Sci* **2012,** *5*, (5), 7161-7167.

127. Biesheuvel, P. M.; van der Wal, A., Membrane capacitive deionization. *J Membrane Sci* **2010,** *346*, (2), 256-262.

128. Kim, Y. J.; Choi, J. H., Improvement of desalination efficiency in capacitive deionization using a carbon electrode coated with an ion-exchange polymer. *Water Res* **2010,** *44*, (3), 990-996.

129. Gao, X.; Omosebi, A.; Landon, J.; Liu, K. L., Dependence of the Capacitive Deionization Performance on Potential of Zero Charge Shifting of Carbon Xerogel Electrodes during Long-Term Operation. *J Electrochem Soc* **2014,** *161*, (12), E159-E166.

130. Lee, J. B.; Park, K. K.; Eum, H. M.; Lee, C. W., Desalination of a thermal power plant wastewater by membrane capacitive deionization. *Desalination* **2006,** *196*, (1-3), 125-134.

131. Nadakatti, S.; Tendulkar, M.; Kadam, M., Use of mesoporous conductive carbon black to enhance performance of activated carbon electrodes in capacitive deionization technology. *Desalination* **2011,** *268*, (1-3), 182-188.

132. Liu, P. Y.; Yan, T. T.; Shi, L. Y.; Park, H. S.; Chen, X. C.; Zhao, Z. G.; Zhang, D. S., Graphene-based materials for capacitive deionization. *J Mater Chem A* **2017,** *5*, (27), 13907-13943.

133. Duan, H. Y.; Yan, T. T.; Chen, G. R.; Zhang, J. P.; Shi, L. Y.; Zhang, D. S., A facile strategy for the fast construction of porous graphene frameworks and their enhanced electrosorption performance. *Chem Commun* **2017,** *53*, (54), 7465-7468.

134. Wang, Z.; Yan, T. T.; Shi, L. Y.; Zhang, D. S., In Situ Expanding Pores of Dodecahedron-like Carbon Frameworks Derived from MOFs for Enhanced Capacitive Deionization. *Acs Appl Mater Inter* **2017,** *9*, (17), 15068-15078.

135. Zhao, S. S.; Yan, T. T.; Wang, H.; Zhang, J. P.; Shi, L. Y.; Zhang, D. S., Creating 3D Hierarchical Carbon Architectures with Micro-, Meso-, and Macropores via a Simple Self-Blowing Strategy for a Flow-through Deionization Capacitor. *Acs Appl Mater Inter* **2016,** *8*, (28), 18027-18035.

136. Yasin, A. S.; Mohamed, H. O.; Mohamed, I. M. A.; Mousa, H. M.; Barakat, N. A. M., Enhanced desalination performance of capacitive deionization using zirconium oxide nanoparticles-doped graphene oxide as a novel and effective electrode. *Sep Purif Technol* **2016,** *171*, 34-43.

137. Qu, Y. T.; Campbell, P. G.; Gu, L.; Knipe, J. M.; Dzenitis, E.; Santiago, J. G.; Stadermann, M., Energy consumption analysis of constant voltage and constant current operations in capacitive deionization. *Desalination* **2016,** *400*, 18-24.

138. Tedesco, M.; Hamelers, H. V. M.; Biesheuvel, P. M., Nernst-Planck transport theory for (reverse) electrodialysis: II. Effect of water transport through ion-exchange membranes. *J Membrane Sci* **2017,** *531*, 172-182.

139. Kim, T.; Yoon, J., CDI ragone plot as a functional tool to evaluate desalination performance in capacitive deionization. *RSC Adv.* **2015,** *5*, (2), 1456-1461.

140. Dykstra, J. E.; Keesman, K. J.; Biesheuvel, P. M.; van der Wal, A., Theory of pH changes in water desalination by capacitive deionization. *Water Res* **2017,** *119*, 178-186.

141. He, D.; Wong, C. E.; Tang, W. W.; Kovalsky, P.; Waite, T. D., Faradaic Reactions in Water Desalination by Batch-Mode Capacitive Deionization. *Environ Sci Tech Let* **2016,** *3*, (5), 222-226.

142. Porada, S.; Bryjak, M.; van der Wal, A.; Biesheuvel, P. M., Effect of electrode thickness variation on operation of capacitive deionization. *Electrochim Acta* **2012,** *75*, 148-156.

143. Tang, W. W.; He, D.; Zhang, C. Y.; Waite, T. D., Optimization of sulfate removal from brackish water by membrane capacitive deionization (MCDI). *Water Res* **2017,** *121*, 302-310.

144. Mistry, K. H.; McGovern, R. K.; Thiel, G. P.; Summers, E. K.; Zubair, S. M.; Lienhard, J. H., Entropy Generation Analysis of Desalination Technologies. *Entropy-Switz* **2011,** *13*, (10), 1829-1864.

145. Yang, Z. Y.; Jin, L. J.; Lu, G. Q.; Xiao, Q. Q.; Zhang, Y. X.; Jing, L.; Zhang, X. X.; Yan, Y. M.; Sun, K. N., Sponge-Templated Preparation of High Surface Area Graphene with Ultrahigh Capacitive Deionization Performance. *Adv Funct Mater* **2014,** *24*, (25), 3917-3925.

146. Wang, Y.; Zhang, L. W.; Wu, Y. F.; Xu, S. C.; Wang, J. X., Polypyrrole/carbon nanotube composites as cathode material for performance enhancing of capacitive deionization technology. *Desalination* **2014,** *354*, 62-67.

147. Rica, R. A.; Ziano, R.; Salerno, D.; Mantegazza, F.; Bazant, M. Z.; Brogioli, D., Electro-diffusion of ions in porous electrodes for capacitive extraction of renewable energy from salinity differences. *Electrochim Acta* **2013,** *92*, 304-314.

148. Hassanvand, A.; Chen, G. Q.; Webley, P. A.; Kentish, S. E., Improvement of MCDI operation and design through experiment and modelling: Regeneration with brine and optimum residence time. *Desalination* **2017,** *417*, 36-51.

149. Zhang, Y. M.; Zou, L. D.; Wimalasiri, Y.; Lee, J. Y.; Chun, Y., Reduced graphene oxide/polyaniline conductive anion exchange membranes in capacitive deionisation process. *Electrochim Acta* **2015,** *182*, 383-390.

150. Choi, J. H., Comparison of constant voltage (CV) and constant current (CC) operation in the membrane capacitive deionisation process. *Desalin Water Treat* **2015,** *56*, (4), 921-928.

151. Wang, L.; Lin, S., Intrinsic tradeoff between kinetic and energetic efficiencies in membrane capacitive deionization. *Water Res* **2017**.

152. Rommerskirchen, A.; Linnartz, C. J.; Muller, D.; Willenberg, L. K.; Wessling, M., Energy Recovery and Process Design in Continuous Flow Electrode Capacitive Deionization Processes. *Acs Sustain Chem Eng* **2018,** *6*, (10), 13007-13015.

153. Yin, H. J.; Zhao, S. L.; Wan, J. W.; Tang, H. J.; Chang, L.; He, L. C.; Zhao, H. J.; Gao, Y.; Tang, Z. Y., Three-Dimensional Graphene/Metal Oxide Nanoparticle Hybrids for High-Performance Capacitive Deionization of Saline Water. *Adv Mater* **2013,** *25*, (43), 6270-6276.

154. Wang, H.; Shi, L. Y.; Yan, T. T.; Zhang, J. P.; Zhong, Q. D.; Zhang, D. S., Design of graphene-coated hollow mesoporous carbon spheres as high performance electrodes for capacitive deionization. *J Mater Chem A* **2014,** *2*, (13), 4739-4750.

155. Gao, X.; Omosebi, A.; Holubowitch, N.; Liu, A.; Ruh, K.; Landon, J.; Liu, K., Polymer-coated composite anodes for efficient and stable capacitive deionization. *Desalination* **2016,** *399*, 16-20.

156. Arulrajan, A. C.; Ramasamy, D. L.; Sillanpaa, M.; van der Wal, A.; Biesheuvel, P. M.; Porada, S.; Dykstra, J. E., Exceptional Water Desalination Performance with Anion-Selective Electrodes. *Adv Mater* **2019,** *31*, (10).

157. Kim, S.; Yoon, H.; Shin, D.; Lee, J.; Yoon, J., Electrochemical selective ion separation in capacitive deionization with sodium manganese oxide. *Journal of colloid and interface science* **2017,** *506*, 644-648.

158. Yang, J.; Zou, L. D.; Choudhury, N. R., Ion-selective carbon nanotube electrodes in capacitive deionisation. *Electrochim Acta* **2013,** *91*, 11-19.

159. Liu, Y. H.; Ma, W.; Cheng, Z. H.; Xu, J.; Wang, R.; Gang, X., Preparing CNTs/Ca-Selective zeolite composite electrode to remove calcium ions by capacitive deionization. *Desalination* **2013,** *326*, 109-114.

160. Hawks, S. A.; Cerón, M. R.; Oyarzun, D. I.; Pham, T. A.; Zhan, C.; Loeb, C. K.; Mew, D.; Deinhart, A.; Wood, B. C.; Santiago, J. G.; Stadermann, M.; Campbell, P. G., Using Ultramicroporous Carbon for the Selective Removal of Nitrate with Capacitive Deionization. *Environ Sci Technol* **2019,** *53*, (18), 10863-10870.

161. Mubita, T. M.; Dykstra, J. E.; Biesheuvel, P. M.; van der Wal, A.; Porada, S., Selective adsorption of nitrate over chloride in microporous carbons. *Water Res* **2019,** *164*.

162. Wang, L.; Dykstra, J. E.; Lin, S. H., Energy Efficiency of Capacitive Deionization. *Environ Sci Technol* **2019,** *53*, (7), 3366-3378.

163. Tandon, R.; Pintauro, P. N., Divalent/monovalent cation uptake selectivity in a Nafion cation-exchange membrane: Experimental and modeling studies. *J Membrane Sci* **1997,** *136*, (1-2), 207-219.

164. Pintauro, P. N.; Tandon, R.; Chao, L.; Xu, W.; Evilia, R., Equilibrium Partitioning of Monovalent Divalent Cation-Salt Mixtures in Nafion Cation-Exchange Membranes. *J Phys Chem-Us* **1995,** *99*, (34), 12915-12924.

165. Fritz, P. A.; Boom, R. M.; Schroen, K., Polyelectrolyte-activated carbon composite electrodes for inverted membrane capacitive deionization (iMCDI). *Sep Purif Technol* **2019,** *220*, 145-151.

166. Bhat, A. P.; Reale, E. R.; del Cerro, M.; Smith, K. C.; Cusick, R. D., Reducing impedance to ionic flux in capacitive deionization with Bi-tortuous activated carbon electrodes coated with asymmetrically charged polyelectrolytes. *Water Res X* **2019,** *3*.

167. Ryoo, M. W.; Seo, G., Improvement in capacitive deionization function of activated carbon cloth by titania modification. *Water Res* **2003,** *37*, (7), 1527-1534.

168. Mubita, T. M.; Porada, S.; Biesheuvel, P. M.; van der Wal, A.; Dykstra, J. E., Capacitive deionization with wire-shaped electrodes. *Electrochim Acta* **2018,** *270*, 165-173.

169. Biesheuvel, P. M., Two-fluid model for the simultaneous flow of colloids and fluids in porous media. *Journal of colloid and interface science* **2011,** *355*, (2), 389-395.

170. Tedesco, M.; Hamelers, H. V. M.; Biesheuvel, P. M., Nernst-Planck transport theory for (reverse) electrodialysis: I. Effect of co-ion transport through the membranes. *J Membrane Sci* **2016,** *510*, 370-381.

171. Lopez-Ramon, M. V.; Stoeckli, F.; Moreno-Castilla, C.; Carrasco-Marin, F., On the characterization of acidic and basic surface sites on carbons by various techniques. *Carbon* **1999,** *37*, (8), 1215-1221.

172. Boehm, H. P., Some Aspects of the Surface-Chemistry of Carbon-Blacks and Other Carbons. *Carbon* **1994,** *32*, (5), 759-769.

173. Huang, C. C.; Yang, M. S.; Liang, M., Synthesis of new thermosetting poly(2,6-dimethyl-1, 4-phenylene oxide)s containing epoxide pendant groups. *J Polym Sci Pol Chem* **2006,** *44*, (20), 5875-5886.

174. Wang, L.; Lin, S. H., Theoretical framework for designing a desalination plant based on membrane capacitive deionization. *Water Res* **2019,** *158*, 359-369.

175. Zhang, C. Y.; Ma, J. X.; Song, J. K.; He, C.; Waite, T. D., Continuous Ammonia Recovery from Wastewaters Using an Integrated Capacitive Flow Electrode Membrane Stripping System. *Environ Sci Technol* **2018,** *52*, (24), 14275-14285.

176. Zhang, C. Y.; Ma, J. X.; Waite, T. D., Ammonia-Rich Solution Production from Wastewaters Using Chemical-Free Flow-Electrode Capacitive Deionization. *Acs Sustain Chem Eng* **2019,** *7*, (7), 6480-6485.

177. Jeon, S. I.; Yeo, J. G.; Yang, S.; Choi, J.; Kim, D. K., Ion storage and energy recovery of a flow-electrode capacitive deionization process. *J Mater Chem A* **2014,** *2*, (18), 6378-6383.

178. Gendel, Y.; Rommerskirchen, A. K. E.; David, O.; Wessling, M., Batch mode and continuous desalination of water using flowing carbon deionization (FCDI) technology. *Electrochem Commun* **2014,** *46*, 152-156.

179. Moreno, D.; Hatzell, M. C., Influence of Feed-Electrode Concentration Differences in Flow-Electrode Systems for Capacitive Deionization. *Ind Eng Chem Res* **2018,** *57*, (26), 8802-8809.

180. Rommerskirchen, A.; Gendel, Y.; Wessling, M., Single module flow-electrode capacitive deionization for continuous water desalination. *Electrochem Commun* **2015,** *60*, 34-37.

181. Liang, P.; Sun, X. L.; Bian, Y. H.; Zhang, H. L.; Yang, X. F.; Jiang, Y.; Liu, P. P.; Huang, X., Optimized desalination performance of high voltage flow-electrode capacitive deionization by adding carbon black in flow-electrode. *Desalination* **2017,** *420*, 63-69.

182. Hatzell, K. B.; Boota, M.; Gogotsi, Y., Materials for suspension (semi-solid) electrodes for energy and water technologies. *Chem Soc Rev* **2015,** *44*, (23), 8664-8687.

183. Yang, S.; Kim, H.; Jeon, S. I.; Choi, J.; Yeo, J. G.; Park, H. R.; Jin, J.; Kim, D. K., Analysis of the desalting performance of flow-electrode capacitive deionization under short-circuited closed cycle operation. *Desalination* **2017,** *424*, 110-121.

184. He, F.; Biesheuvel, P. M.; Bazant, M. Z.; Hatton, T. A., Theory of water treatment by capacitive deionization with redox active porous electrodes. *Water Res* **2018,** *132*, 282-291.

185. Dennison, C. R.; Beidaghi, M.; Hatzell, K. B.; Campos, J. W.; Gogotsi, Y.; Kumbur, E. C., Effects of flow cell design on charge percolation and storage in the carbon slurry electrodes of electrochemical flow capacitors. *J Power Sources* **2014,** *247*, 489-496.

186. Rommerskirchen, A.; Ohs, B.; Hepp, K. A.; Femmer, R.; Wessling, M., Modeling continuous flow-electrode capacitive deionization processes with ion-exchange membranes. *J Membrane Sci* **2018,** *546*, 188-196.

187. Grahame, D. C., The Electrical Double Layer and the Theory of Electrocapillarity. *Chem Rev* **1947,** *41*, (3), 441-501.

188. Maghanua B. S., Bowers A. R., Effect of recycle and axial mixing on microbial selection in activated sludge. *J Environ Eng* **1998,** *124*, (10), 970-978.

189. Nativ, P.; Badash, Y.; Gendel, Y., New insights into the mechanism of flow-electrode capacitive deionization. *Electrochem Commun* **2017,** *76*, 24-28.

190. Ma, J. X.; He, C.; He, D.; Zhang, C. Y.; Waite, T. D., Analysis of capacitive and electrodialytic contributions to water desalination by flow-electrode CDI. *Water Res* **2018,** *144*, 296-303.

191. Zhang, W. L.; Lin, H. B.; Lu, H. Y.; Liu, D. C.; Yin, J.; Lin, Z. Q., On the electrochemical origin of the enhanced charge acceptance of the lead-carbon electrode. *J Mater Chem A* **2015,** *3*, (8), 4399-4404.

APPENDIX A

SUPPLEMENTARY MATERIAL FOR CHAPTER 3

A.1 Interpretation of separation line

The separation line contains two fragments divided by the initial feed concentration (c_0), with two ends representing brine (c_B) and deionized (c_D) concentrations. Water recovery (γ) is illustrated on the separation line as shown in Fig 1A.

According to mass balance of salt:

$$c_0 = c_B(1-\gamma) + c_D\gamma$$

Rearrange the above equation yields

$$c_B = \frac{c_0 - c_D\gamma}{1-\gamma}$$

Further rearrange the above equation yields

$$\frac{c_B - c_0}{c_0 - c_D} = \frac{\frac{c_0 - c_D\gamma}{1-\gamma} - c_0}{c_0 - c_D} = \frac{\gamma}{1-\gamma}$$

Table A1. Summary of the literature data used in constructing Figure 3.2

Fig. 2 Symbol	c_0 (mM)	c_D (mM)	γ (%)	Δg (Wh/m^3)	*SEC* (Wh/m^3)	*TEE* (%)	Type/Operation Mode	Ref.[§]
a	20	9.1	50	8.65	350~207	2.47~4.17	MCDI/CCRC	14
b	20	9.8	50	7.52	320	2.35	MCDI/CCZV	14
c	20	12.9	50	3.57	69.3	5.15	MCDI/CVZV	14
e	3.42	0.9	60	3.18	193	1.65	MCDI/CVZV	54
d	40	22.3	50	11.2	745~535	1.50~2.09	MCDI/CCRC	37
f	3.4	0.4	60	4.88	135	3.60	MCDI/CVZV	55
g	10	6.2	50	2.00	177	1.13	im-CDI/CVZV	55
h	3.2	1.7	67	1.41	208	0.675	CDI/CVZV	56
i	3	1.8	67	0.88	107	0.825	CDI/CVZV	56
j	3.5	2.4	67	0.73	74.2	0.982	CDI/CVZV	56
k	2.9	2.6	67	0.074	48.8	0.152	CDI/CVZV	55
l	8.7	6.8	50	0.61	50.0	1.23	CDI/CVZV	5
m	8.7	4.4	50	0.31	2.35E+00	0.131	CDI/CVZV	57
n	8.6	2.7	50	0.62	34.3~25.7	1.80~2.40	MCDI/CCRC	39*
o	8.6	3.3	50	0.48	28.1~17.7	1.70~2.70	MCDI/CCRC	39*
p	8.6	3.9	50	0.37	30.8~16.1	1.20~2.30	MCDI/CCRC	39*
q	8.6	4.4	50	0.29	22.7~10.9	1.30~2.70	MCDI/CCRC	39*
r	8.6	5.3	50	0.18	25.8~6.95	0.7~2.60	MCDI/CCRC	39*
s	8.6	6.1	50	0.10	20.4~4.35	0.49~2.30	MCDI/CCRC	39*
t	10	8.6	69	0.39	11.2~6.98	3.50~5.62	CDI/CCRC	58
u	10	8.8	50	0.22	16.8	1.29	CDI/CVZV	58
v	20	18.4	50	0.18	8.34~8.17	2.12~2.16	CDI/CV non-ZV	27
w	5	3.5	50	0.66	61.1	1.07	CDI/CVZV	5
x	5	3.8	50	0.41	47.2	0.863	CDI/CVZV	5

y	10	8.6	50	0.28	29.5/22.1	0.931/1.24	MCDI/ Energy Recovery[#]	53
z	10	8.5	50	0.32	67.6	0.473	im-CDI/CVRV	59
aa	4.3	3.5	50	0.20	47.8	0.421	i-CDI	23
ab	4.3	3.9	50	0.057	45.7	1.24	i-CDI	23
ac	5	4.2	50	0.177	52.8	0.335	im-CDI/CVZV	60
ad	5	4.3	50	0.151	24.4	0.62	CDI/CVZV	61
ae	5	4.74	50	0.0186	8.58	0.217	CDI/CVZV	61
af	5	4.9	50	1.76E-03	0.783	0.225	CDI/CVZV	61
ag	10	9.3	50	0.0619	26.2	0.236	CDI/CVZV	62
ah	5	4.7	50	0.0248	10.1	0.246	MCDI/CVZV	15
ai	20	19.3	50	0.0319	35.7~21.2	0.089~0.15	CDI/CCRC	13
aj	20	19.6	50	0.011	24.7	0.0446	CDI/CCZV	13
ak	20	19.8	50	3.64E-03	8.90	0.0409	CDI/CVZV	13
al	4.3	4.2	50	3.20E-03	6.77	0.0474	Inverted CDI	63
am	597	388	50	103.05	340	30.3	im-CDI/CCRC	68
an	521	391	50	45.34	241.2	18.8	im-CDI/CCRC	49
ao	25	17.3	50	3.31	51.10	6.47	im-CDI/CCRC	64
ap	25	16.9	50	3.66	24.00	15.2	im-CDI/CCRC	64
aq	25	17.1	50	3.49	18.70	18.7	im-CDI/CCRC	64
ar	25	19	50	2.00	23.90	8.4	im-CDI/CCRC	64
as	25	19.4	50	1.75	12.60	14.0	im-CDI/CCRC	64
at	25	19.8	50	1.50	8.40	17.8	im-CDI/CCRC	64
au	25	20.9	50	0.92	13.10	7.01	im-CDI/CCRC	64
av	25	21.3	50	0.77	6.71	11.4	im-CDI/CCRC	64
aw	25	21.4	50	0.73	5.05	14.5	im-CDI/CCRC	64
ax	8.56	6.4	50	0.77	1.88	40.7	im-CDI/CVRV	65
ay	1.71	1.57	50	1.61E-03	0.34	0.5	im-CDI/CVZV	66
az	8.54	7.58	50	0.15	3.36	0.4	im-CDI/CVRV	67
ba	8.54	7.55	50	0.16	6.58	0.2	im-CDI/CVRV	67
bb	8.54	7.3	50	0.25	9.20	0.3	im-CDI/CVRV	67
bc	100	96.65	50	0.15	0.50	0.31	im-CDI/CCRC	68
bd	13.35	12.91	50	0.02	1.08	0.02	im-CDI/CCRC	69
be	20	18.51	50	0.15	0..21	0.72	im-CDI/CCRC	70
bf	20	19.5	50	0.02	0.13	0.13	im-CDI/CCRC	70

§ These numbers refer to the references in the main manuscript, not that in the supporting information

* Δg and TEE for this reference are directly reported. The c_D were back calculated from Δg.

[#] Energy was actually recovered during discharge using a buck-boost converter.

Legend of Figure 2: the squares with left solid half are im-CDI processes with intercalation materials; the squares with bottom solid half are from inverted CDI; the square with upper solid half discharges at a positive voltage; and the square with right solid half recovers energy with a buck-boost converter. The bars represents of operations with possible energy recovery. The circles are conventional CDI processes.

Table A2. Data extracted from Ref. [75] (shown as "pink ovals" or labelled as "bg" in Figure 3.2).

c_0 (mM)	γ (%)	Δg (Wh/m^3)	*SEC* (Wh/m^3)	*TEE* (%)
20	50	19.73	0.28	1.43
20	50	20.96	0.49	2.34
20	50	23.84	0.22	0.90
20	50	25.89	0.51	1.97
20	50	29.18	0.94	3.23
20	50	30.82	1.13	3.66
20	50	32.47	0.56	1.72
20	50	37.40	1.06	2.83

20	50	37.40	1.81	4.84
20	50	40.27	1.33	3.30
20	50	44.38	1.96	4.42
20	50	46.85	1.99	4.26
20	50	53.01	4.06	7.66
20	50	55.89	1.62	2.90
20	50	56.71	2.86	5.05
20	50	57.12	1.37	2.39
20	50	58.77	3.80	6.47
20	50	65.34	5.81	8.89
20	50	69.45	2.70	3.89
20	50	76.44	5.21	6.81
20	50	80.96	3.17	3.91
20	50	83.01	1.69	2.04
20	50	87.12	5.56	6.38
20	50	91.64	5.21	5.68
20	50	109.73	4.59	4.18
20	50	112.19	7.27	6.48
20	50	115.07	4.29	3.73
20	50	121.64	5.99	4.92
20	50	162.33	3.98	2.45
20	50	192.33	2.42	1.26
20	50	19.73	0.28	1.43
20	50	20.96	0.49	2.34
20	50	23.84	0.22	0.90
20	50	25.89	0.51	1.97
20	50	29.18	0.94	3.23
20	50	30.82	1.13	3.66
20	50	32.47	0.56	1.72
20	50	37.40	1.06	2.83
20	50	37.40	1.81	4.84
20	50	40.27	1.33	3.30
20	50	44.38	1.96	4.42
20	50	46.85	1.99	4.26
20	50	53.01	4.06	7.66
20	50	55.89	1.62	2.90
20	50	56.71	2.86	5.05
20	50	57.12	1.37	2.39
20	50	58.77	3.80	6.47
20	50	65.34	5.81	8.89
20	50	69.45	2.70	3.89
20	50	76.44	5.21	6.81
20	50	80.96	3.17	3.91
20	50	83.01	1.69	2.04
20	50	87.12	5.56	6.38
20	50	91.64	5.21	5.68
20	50	109.73	4.59	4.18
20	50	112.19	7.27	6.48
20	50	115.07	4.29	3.73
20	50	121.64	5.99	4.92
20	50	162.33	3.98	2.45
20	50	192.33	2.42	1.26

Table A3. Summary of the literature data on RO.					
c_0 (mM)	γ (%)	Δg (Wh/m^3)	*SEC* (Wh/m^3)	*TEE* (%)	Ref.*
11	70	26	228	11.4	S1
8	65	18	119	15.3	S1
15	75	39	322	12.1	S1
15	75	39	264	14.8	S1
43	13	64	139	46.0	S2
43	23	68	133	50.7	S2
51	81	145	556	26.1	S3
34	79	93	378	24.6	S3
15	75	37	333	11.2	S4
43	66	96	389	24.7	S5
60	75	152	472	32.3	S6
712	45	1302	1806	72.1	S7
698	45	1276	1769	72.1	S7
602	28	972	1578	61.6	S8
841	13	1239	1717	72.2	S8
These references with an "S" prefix are for the supporting information and cited within this document only. The same rule applies to all references below.					

A.2 Calculation of TEE of CDI from published literature data

As discussed in the main text, SEC and Δg are calculated for CDI processes from the reported data. Here, a specific example is given to illustrate the detailed approaches for obtaining *TEE*. For a CDI process, Δg is calculated according to equation (1). Let us use an example from the publication authored by Zhao et al.[S9], who utilized a flow-by deionization cell with a constant flowrate of 1 mL/s. The data in Figure 3 of the publication was extracted using Plot Digitizer (http://plotdigitizer.sourceforge.net). With CV mode, the applied voltage was 1.2 V. The charging and discharge durations were both 300 seconds. The total energy consumption was the product of the voltage and the cumulative transferred charge (CTC). The CTC can be obtained from integrating the current with respect to time over the charging step (the left "triangle" in Figure A1). The CTC was calculated as 62.36 C, and thus the energy consumption was 74.83 J.

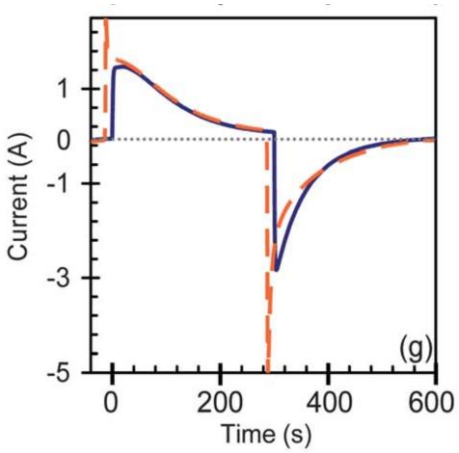

Figure A. 1. An example "current vs time" curve from literature (Zhao et al. [ref. 14], Figure 3). Data was extracted from each of such curves in the literature using a freeware called Plot Digitizer. The data was then used for numerical integration to calculate the energy consumption from the "current vs time" (for CV CDI) and "voltage vs time" (for CC CDI) curves. Similar approach was also applied to estimate the concentration of the diluted solution and the brine solution.

SEC can thus be calculated as

$$SEC = \frac{74.83\,J}{1mL/s\ \times 300s} = 249.44\frac{J}{L} = 0.0693\ kWh/m^3$$

Because both charging time and discharging time were same, and the flowrate was kept constant, the recovery $\gamma = 0.5$. The influent concentration to the cell was 20 mM, and the mean effluent concentration was 12.88 mM (this value is obtained by averaging the concentration from the effluent concentration vs time graph). In the mode of constant voltage charging, the effluent concentration changes with time, and the average effluent concentration was obtained to calculate Δg.

$$\Delta g = \nu RT\left\{\frac{c_0}{\gamma}\ln\left[\frac{c_0-\gamma c_D}{c_0(1-\gamma)}\right] - c_P\left[\frac{c_0-\gamma c_D}{c_D(1-\gamma)}\right]\right\} = 12.85\frac{J}{L} = 0.0036kW\cdot h/m^3$$

All other data points in Figure 3.2 of the main text were calculated following the same approach.

A.3 Explanation of 'flow system limitation'

For better illustration, we consider a different separation (c_0=20 mM, c_D=1 mM, c_B=39 mM, and γ=0.5) for which Δg is higher and the reversible cycle is "thicker" than that in Figure 3.3 (even this illustrated separation is very difficult to achieve in practice with current CDI

systems). The thermodynamically reversible cycle of such a separation is outlined in Figure A.2(A) by the solid contour enclosing the yellow region. We note that such a reversible cycle is attainable only in a batch CDI process in which the bulk concentration decreases gradually as salts are removed. Such a reversible process and the quantification of its energy consumption was described in detail by using Gouy-Chapman-Stern model and modified Donnan model. [S10, S11]

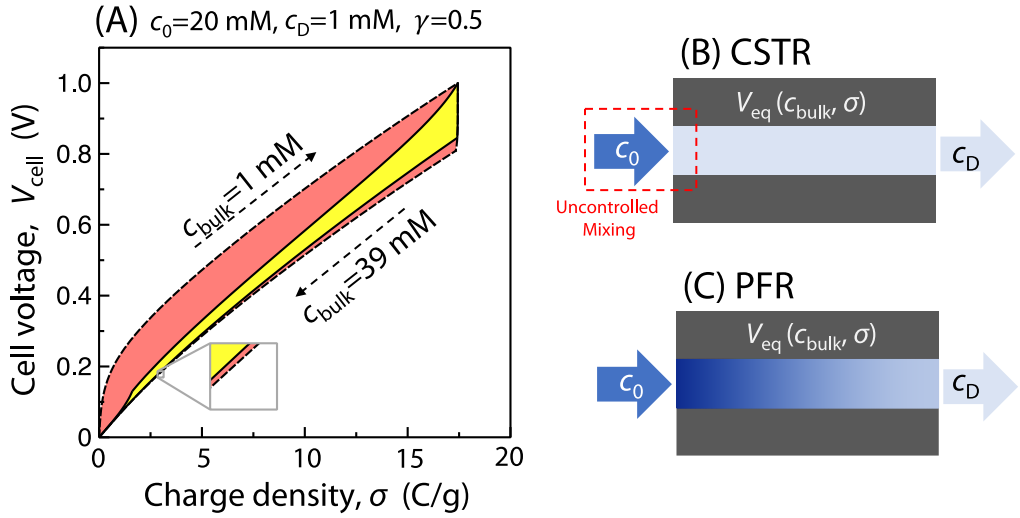

Figure A. 2. (A) cell voltage as a function of charge density for a thermodynamically reversible batch CDI process and a flow-by CDI process for which (1) both the spacer and macropores are modeled as one single CSTR and (2) V_{cell} always equals V_{eq}. The reversible batch CDI process is represented by the contour encompassing the yellow region, whereas the flow-by CDI process with the CSTR assumption is presented by the dash contour encompassing both the yellow and red regions. The separation achieved by both processes is characterized by c_0=20 mM, c_D=1 mM, c_B=39 mM, and γ=0.5. (B) Illustration of "uncontrolled mixing" for a flow-by CDI with the CSTR assumption. The darkness of the blue color represents salinity. (C) Illustration of spatially variant salinity in a flow-by CDI process with PRF assumption. The equilibrium voltage varies along the spacer channel as it depends on bulk concentration that is also spatially variant.

For flow-by CDI, we first consider a continuously-stirred tank reactor (CSTR) with constant effluent concentration, c_D, which may be achieved by an ideally mixed system with CC-RC operation. The charging and discharge curves are represented by the dash curves in Figure S2A. Accordingly, *SEC* is proportional to the area outlined by the dash cycle (i.e. the sum of yellow and red regions), which is significantly higher than Δg itself. The charging and discharge curves represent two series of equilibrium states with constant bulk concentrations, i.e., the electrodes are

always in equilibrium with a bulk solution of 1 mM and 39 mM in the charging and discharge stages, respectively. We also note that the current density must thus be infinitesimally small because the system is always in equilibrium. Such a process with constant current but infinitesimally small current density is theoretically possible with infinite electrode area.

The red region in Figure A2(A) represents the energy loss in a process where V_{cell} is always maintained as V_{eq}. Such energy loss is not of a resistive nature, but rather originates from the "uncontrolled mixing" between the influent stream of a concentration c_0 and the solution in the spacer of a concentration c_D (Figure A2(B)). Analogous phenomenon has been reported for close-circuit RO in which solutions of different salinities are mixed in an uncontrolled manner. [S12] The mixing of two solutions of different salinities releases the Gibbs free energy of mixing. Such energy can be either harvested to do work using controlled systems, such as pressure retarded osmosis or reverse electrodialysis, [S13] or dissipated as heat as in this case described by Figure A2(B).

If the spacer channel is modeled as a plug-flow reactor (PFR), this effect of "uncontrolled mixing" vanishes, but another effect prevents the CDI process from being thermodynamic reversible. Specifically, charging and discharge at V_{eq} is impossible in this case because V_{eq} is dependent on spacer channel concentration which is spatially variant in a PFR (Figure A2(C)). In other words, there is not a single V_{cell} that allows the system to achieve equilibrium at all positions. This is analogous to a constant pressure RO process in which the driving force varies spatially along the module.

Table S4. Parameters for simulating Figure 3.

Symbols	Description	Value*	Dimension
α	Charge dependence coefficient of Stern capacitance	20	F m^3 mol^{-2}
p_{sp}	Spacer porosity	0.708	
p_{ma}	Electrode macroporosity	0.43	
p_{mi}	Electrode microporosity	0.30	
A	Electrode geometric surface area	33.8	cm^2
$C_{st,vol,0}$	Volumetric Stern layer capacitance at zero charge	120	F mL^{-1}

D_e	Effective diffusion coefficient	1.68×10^{-5}	$cm^2\ s^{-1}$
D_{mem}	Diffusion coefficient in the membrane	1.12×10^{-5}	$cm^2\ s^{-1}$
L_{elec}	Electrode thickness	250	μm
L_m	Ion exchange membrane thickness	150	μm
L_{sp}	Spacer thickness	250	μm
M	Total mass of electrodes	4	g
N	Number of electrode pair	4	
$R_{contact}$	Specific contact and external resistance	30	$\Omega\ cm^2$
$R_{electrode}$	Specific electrode resistance	0.22	Ω mmol cm^{-1}
X	Intrinsic charge of ion exchange membrane	5	mol L^{-1}
* These values were used in the model section of this ref. S14 and were consistent with values that have been in reported in other literature.			

A.4 Methodology of simulating potential drops and energy losses in Figure 3.3

Theoretical analysis is carried out for simulating potential drops and energy losses presented in Fig 3 of the main text. Both CDI (Fig 3A, C, E) and MCDI (Fig 3B, D, F) are analyzed, with the identical target separation. The separation achieved is characterized by: c_0=20 mM (NaCl), c_D=12 mM, v_D =100 mL, and γ =50 %. The applied current density is 30 A m^{-2}. Details about the transport theory, which also can be found in our previous study,[S14] are presented below. The definitions and values of the parameters used in the model are summarized in Table S4. We combine the modified Donnan (mD) theory and the Nernst-Planck (NP) equation to relate the charge density, salt ion transport and potential to one another. The carbon electrode is considered to be of two types of porosity: micropores that majorly contribute to the ion adsorption capacity, and macropores serving as pathways for ion transport. The mD theory describes the formation of electrical double layers (EDLs) in the micropores, and the NP equation is used to calculate the transport of charged ions. When modelling the CDI process, salt concentration in the spacer channel is assumed to be same as that in the electrode macropores. For MCDI, the presence of ion

exchange membranes (IEMs) introduces two Donnan potentials (i.e. between spacer and the IEM, electrode macropores and the IEM), and one potential drop across the IEM due to ionic resistance. The potential drops (Fig 3A&B) in each component of the CDI/MCDI system are obtained from the transport model. From there, energy breakdowns (Fig 3C&D) are generated by integrate the voltage of each component with charge.

Detailed equations used in constructing Figure 3A, B, C, and D in the main text:

CDI: According to the mD model, the ion concentration inside the micropores is related to the salt concentration in the electrode macropores following the equation:

$$c_{i,mi} = c_{mA} \cdot \exp(-z_i \cdot \Delta\phi_d) \qquad \text{Eqn. A-1}$$

where $c_{i,mi}$ is the concentration of ion i in the micropores, c_{mA} is the salt concentration in the macropores, z_i is the ion charge (for monovalent salt, +1 for the cation and -1 for the anion), and $\Delta\phi_d$ is the dimensionless Donnan potential difference between the micropores and the macropores.

Inside the micropores, the charge density, σ_{mi}, is defined as the difference between $c_{cation,mi}$ and $c_{anion,mi}$.

$$\sigma_{mi} = c_{cation,mi} - c_{anion,mi} = -2 \cdot c_{mA} \cdot \sinh(\Delta\phi_d) \qquad \text{Eqn. A-2}$$

This charge density is also related to the potential drop ($\Delta\phi_{st}$) across the Stern layer, which is a charge-free layer in between the salt-storing micropores and the electrode matrix.

$$\sigma_{mi} \cdot F = -C_{st,vol} \cdot \Delta\phi_{st} \cdot V_T \qquad \text{Eqn. A-3}$$

where F is the Faraday constant and $C_{st,vol}$ is the volumetric Stern layer capacitance. An empirical relating $C_{st,vol}$ and σ_{mi} (i.e. $C_{st,vol} = C_{st,vol,0} + \alpha \cdot \sigma_{mi}^2$) is employed to account for the increase of $C_{st,vol}$ from the capacitance at zero charge ($C_{st,vol,0}$) due to the electrostatic compression at non-zero charge.

Upon charging the (M)CDI assembly, the volumetric charge density with the current density and their relationship is expressed as:

$$\frac{\partial}{\partial t}(p_{mi} \cdot \sigma_{mi}) = \frac{I}{L_{elec} \cdot F} \qquad \text{Eqn. A-4}$$

The ion concentrations in the electrode micro- and macropores change with respect to time, which is determined by the ion flux (J_{ions}):

$$\frac{\partial}{\partial t}\left(2 \cdot p_{mA} \cdot \mathrm{c}_{mA} + p_{mi} \cdot \mathrm{c}_{mi,ions}\right) = \frac{J_{ions}}{L_{elec}} \qquad \text{Eqn. A-5}$$

where p_{mA} and p_{mi} are the macropore and micropore porosities respectively, $c_{mi,ions}$ is the micropore ion concentration ($c_{mi,ions} = c_{cation,mi} + c_{anion,mi}$), and L_{elec} is the electrode thickness.

In the spacer channel, mass balance is used to describe the change of the salt concentration (c_{sp}):

$$p_{sp} \cdot \frac{\partial c_{sp}}{\partial t} = -\frac{J_{ions}}{L_{sp}} + \frac{c_{sp,inflow} - c_{sp}}{\tau} \quad \text{Eqn. A-6}$$

where p_{sp} is the spacer porosity, c_{sp} is the salt concentration in the spacer, L_{sp} is the spacer thickness, $c_{sp,inflow}$ is the influent concentration, and τ is the hydraulic retention time in the spacer channel.

The current, I, depends on the electrical potential difference across the spacer channel and the spacer salt concentration according to the NP equation neglecting the concentration gradient:

$$I = -4 \cdot D \cdot c_{sp} \cdot \frac{\Delta\phi_{sp,half}}{L_{sp}} \cdot F \quad \text{Eqn. A-7}$$

where D is the bulk diffusion coefficient of the charged ions, $\Delta\phi_{sp,half}$ is the half of the spacer channel potential drop and L_{sp} is the spacer thickness.

The potential drop in the carbon electrode material is related to the salt concentration in the macropore and the current density according to:

$$\Delta\phi_{elec} \cdot V_T = I \cdot R_{elec}/c_{mA} \quad \text{Eqn. A-8}$$

where R_{elec} is the specific electrode resistance.

MCDI: For the ion transport in MCDI, the existence of IEMs adds another level of complexity. The following equations are specifically for the MCDI model. By neglecting concentration gradient, the current in the IEMs is related to the potential drop across the IEMs according to the NP equation:

$$I = -D_{mem} \cdot \bar{c}_{mem} \frac{\Delta\phi_{mem}}{L_{mem}} \cdot F \quad \text{Eqn. A-9}$$

where D_{mem} is the diffusion coefficient of the ions in the membrane, $\bar{c}_{mem}$ is the average ion concentration in the membrane, and L_{mem} is the membrane thickness. Approximately, $\bar{c}_{mem}$ is calculated as the average of the ion concentrations at the two interfaces (i.e. membrane/spacer and membrane/electrode), which are given by the following equations:

$$c_{mem/elec} = 2 \cdot c_{mA} \cdot \cosh(\Delta\phi_{m/e}) \quad \text{Eqn. A-10}$$

$$c_{mem/sp} = 2 \cdot c_{sp} \cdot \cosh(\Delta\phi_{m/sp}) \quad \text{Eqn. A-11}$$

$$\bar{c}_{mem} = \frac{1}{2} \cdot (c_{mem/elec} + c_{mem/sp}) \quad \text{Eqn. A-12}$$

where $c_{mem/elec}$ and $c_{mem/sp}$ are the ion concentrations at the membrane/electrode and the membrane/electrode interfaces, respectively.

Donnan potentials ($\Delta\phi_{m/e}$ and $\Delta\phi_{m/sp}$) rise as the ion concentrations are different at the aforementioned interfaces. The potentials are calculated using Boltzmann equation and charge neutrality. The results can be expressed as:

$$\Delta\phi_{mem/sp} = sinh^{-1}\frac{\omega X}{c_{sp}} \quad \text{Eqn. A-13}$$

$$\Delta\phi_{mem/elec} = sinh^{-1}\frac{\omega X}{c_{mA}} \quad \text{Eqn. A-14}$$

In addition, the ion flux across the membrane, J_{ions}, can be expressed as

$$J_{ions} = -\frac{D_{mem}}{L_{mem}}(\Delta c_{mem} - \omega \cdot X \cdot \Delta\phi_{mem}) \quad \text{Eqn. A-15}$$

where Δc_{mem} is the difference between the ion concentrations at the two membrane interfaces (i.e. the difference between $c_{mem/elec}$ and $c_{mem/sp}$, ω is the sign of the membrane charge (+1 for anion exchange membranes, and -1 for cation exchange membranes), and X is the intrinsic membrane charge density. The energy consumption of each component is obtained by integrating the voltage drop of each component with respect to charge.[S15, S16]

To construct the thermodynamically reversible cycle as presented in Figure 3.3B and 3.3E (yellow region), we employ the modified Donnan (mD) model for a batch reversible process as described in detail in our previous publication.[S11] Briefly, the mD theory relates the micropore charge density, macropore ion concentration (which is the same as bulk concentration in a batch reversible process), Stern potential, and Donnan potential. As the cell potential changes, ions migrate either from the bulk solution (including macropore) to the micropores or the opposite way, which results in change of micropore charge density and distribution of ions between the micropore and bulk solution (including macropore). The cell voltage of the thermodynamic reversible process is the sum of the Stern layer and the Donnan potentials. The target separation is the same as that specified in the dynamic transport model.

A.5 Explanation of equation 7

TEE is defined as the ratio between Δg and SEC_w, based on equation 2. SEC_w is roughly proportional to $\Delta V \Delta c / \Lambda_{dyn}$. Here, ΔV is the difference between the average voltages in charging and discharge, which is exactly equal to the charging voltage in CV-ZV operation (Figure 4) and roughly equal to the average height of the blue region in Figure 3E and 3F in CC-RC operation. Therefore, $e\Delta V$ is roughly the energy consumed to transfer a unit charge. Since not all charge transfer can result in ion transfer due to co-ion repulsion and Faradaic reactions, the energy consumed to transfer an ion is equal to $e\Delta V / \Lambda_{dyn}$, which is or proportional to SEC_i. If SEC_i has the unit of J/mole and SEC_w has the unit of J/L, then we simply need to multiply SEC_i by the concentration reduction, Δc, (mole/L) to obtain SEC_w. Therefore, SEC_w should be proportional to $\Delta V \Delta c / \Lambda_{dyn}$. The coefficient β depends on the specific unit chosen for each parameter.

References of Appendix A

1. Huang, X. F.; Ling, J.; Xu, J. C.; Feng, Y.; Li, G. M., Advanced treatment of wastewater from an iron and steel enterprise by a constructed wetland/ultrafiltration/reverse osmosis process. *Desalination* **2011,** *269*, (1-3), 41-49.
2. Shen, J.; Richards, B. S.; Schafer, A. I., Renewable energy powered membrane technology: Case study of St. Dorcas borehole in Tanzania demonstrating fluoride removal via nanofiltration/reverse osmosis. *Sep Purif Technol* **2016,** *170*, 445-452.
3. Sambrailo, D.; Ivic, J., First land-based plant for RO desalination in Croatia. *Desalination* **2000,** *132*, (1-3), 329-335.
4. Belkacem, M.; Bakhti, S.; Aomraoui, S., Groundwater treatment by reverse osmosis: Effect of brine recycling on fouling. *Desalin Water Treat* **2009,** *9*, (1-3), 54-58.
5. Aljundi, I. H., Second-law analysis of a reverse osmosis plant in Jordan. *Desalination* **2009,** *239*, (1-3), 207-215.
6. Majali, F.; Ettouney, H.; Abdel-Jabbar, N.; Qiblawey, H., Design and operating characteristics of pilot scale reverse osmosis plants. *Desalination* **2008,** *222*, (1-3), 441-450.
7. Stover, R. L., Seawater reverse osmosis with isobaric energy recovery devices. *Desalination* **2007,** *203*, (1-3), 168-175.
8. Praptowidodo, V. S.; Khalik, A., Studies on seawater desalination by reverse osmosis at the Badak natural gas liquefaction plant, Bontang, East Kalimantan. *Desalination* **2000,** *132*, (1-3), 323-328.
9. Zhao, R.; Biesheuvel, P. M.; van der Wal, A., Energy consumption and constant current operation in membrane capacitive deionization. *Energ Environ Sci* **2012,** *5*, (11), 9520-9527.
10. Biesheuvel, P. M., Thermodynamic cycle analysis for capacitive deionization. *Journal of colloid and interface science* **2009,** *332*, (1), 258-264.
11. Wang, L.; Biesheuvel, P. M.; Lin, S., Reversible Thermodynamic Cycle Analysis for Capacitive Deionization with Modified Donnan Model. *Journal of colloid and interface science* **2017**.
12. Lin, S. H.; Elimelech, M., Staged reverse osmosis operation: Configurations, energy efficiency, and application potential. *Desalination* **2015,** *366*, 9-14.

13. Yip, N. Y.; Brogioli, D.; Hamelers, H. V. M.; Nijmeijer, K., Salinity Gradients for Sustainable Energy: Primer, Progress, and Prospects. *Environ Sci Technol* **2016,** *50*, (22), 12072-12094.
14. Wang, L.; Lin, S. H., Membrane Capacitive Deionization with Constant Current vs Constant Voltage Charging: Which Is Better? *Environ Sci Technol* **2018,** *52*, (7), 4051-4060.
15. Dykstra, J. E.; Porada, S.; van der Wal, A.; Biesheuvel, P. M., Energy consumption in capacitive deionization - Constant current versus constant voltage operation. *Water Res* **2018,** *143*, 367-375.
16. Dykstra, J. E. Desalination with porous electrodes : mechanisms of ion transport and adsorption. Wageningen University, Wageningen, the Netherlands, 2018.

APPENDIX B

SUPPLEMENTARY MATERIAL FOR CHAPTER 4

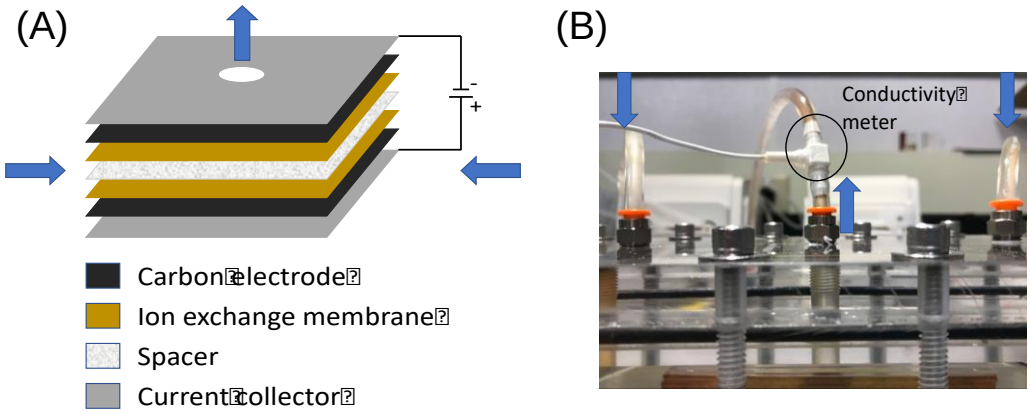

Figure B. 1. (A) The schematic structure of one MCDI cell (assembly). The MCDI stack is composed of four such assemblies. (B) The cross-section view of an actual MCDI stack. In both images, the blue arrows show the direction of the flow.

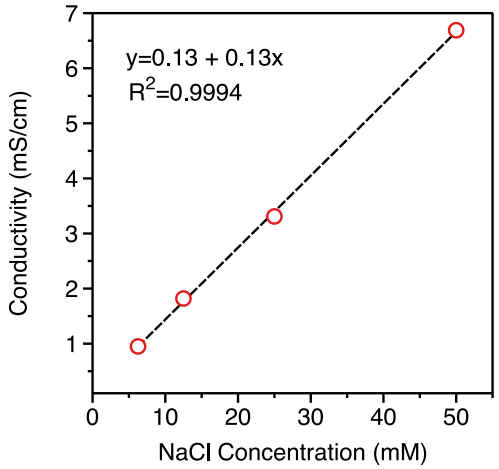

Figure B.2. Measured conductivity as a function of the NaCl concentration (in mM) of solution flowing through the inline conductivity probe.

APPENDIX C

SUPPLEMENTARY MATERIAL FOR CHAPTER 5

Table C1. Experimental conditions for achieving a target adsorption of c_0=20 mM, c_d=14.4 mM, and v_d=100 mL

	Flowrate (mL/min)				
	8.0	9.1	10.0	13.0	13.9
Voltage in CC charging (V)	1.16	1.18	1.2	1.25	1.30
Current in CV charging (mA)	74	89.3	92	126.3	135
Charging duration (min)	12.5	11	10	7.7	7.2

Table C2. Measured average dilute concentration, c_d (mM)

	Flowrate (mL/min)				
	8.0	9.1	10.0	13.0	13.9
CV charging	14.4	14.1	14.8	14.5	14.4
CC charging	14.1	14.4	14.6	14.3	14.2

Table C3. "Coefficient of determination" as a measure of the goodness of fitting for the data sets in Figure 5.2.

	ASAR	SEC^{-1}
CC charging	0.969	0.994
CV charging	0.854	0.949

Table C4. Parameter settings for the dynamic transport model

Symbols	Description	Value	Dimension
p_{sp}	Spacer porosity	0.708	
p_{ma}	Electrode macroporosity	0.43	
p_{mi}	Electrode microporosity	0.25	

L_{elec}	Electrode thickness	280	μm
L_m	Ion exchange membrane thickness	150	μm
L_{sp}	Space thickness	250	μm
A	Electrode area	33.75	cm^2
D_e	Effective ion diffusion coefficient	1.68×10^{-5}	$cm^2\ s^{-1}$
D_{mem}	Ion diffusion coefficient in the membrane	1.12×10^{-5}	$cm^2\ s^{-1}$
R_{elec}	Specific electrode resistance	0.7	$\Omega\ mol\ m^{-1}$
R_{ext}	External resistance	40.1	$\Omega\ cm^2$
$C_{st,vol}$	Stern capacitance	120	$F\ mL^{-1}$
α	Charge dependence coefficient of Stern capacitance	17.3	$F\ m^3\ mol^{-2}$
X	Fixed ion exchange membrane charge density	5	$mol\ L^{-1}$

APPENDIX D

SUPPLEMENTARY MATERIAL FOR CHAPTERS 6 AND 7

D.1 Experimental results fitting with model

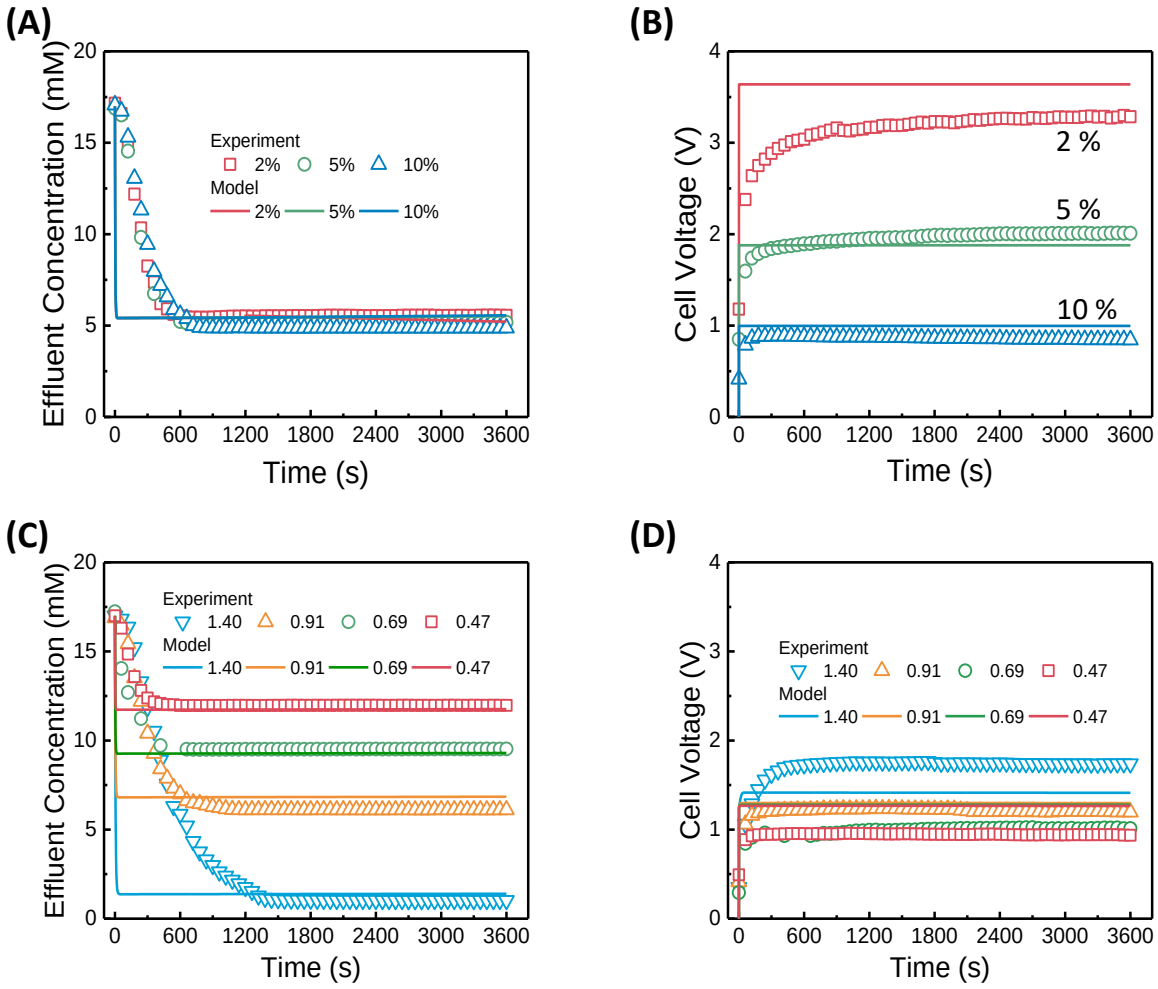

Figure D. 1. Model fits to experimental results. (A) and (B) are effluent concentration and cell voltage with carbon loadings of 2%, 5% and 10% when charging at 25.2 A m^{-2} and HRT of the flow in the spacer channel of 0.69min. (C) ad (D) are effluent concentration and cell voltage for HRTs in the spacer channel of 0.47, 0.69, 0.91 and 1.40min when charging at 16.8 A m^{-2} and carbon content of 5%.

D.2 Summary of parameters used in the model

Table D1. List of model parameters

Symbols	Description	Value	Dimension
α	Charge dependence coefficient of Stern capacitance	20	F m^3 mol^{-2}
ρ_{AC}	AC conductivity	105	S m^{-1}
λ_S	NaCl molar conductivity	0.0111	S m^2 mol^{-1}
γ	Empirical coefficient	0.25	
p_{sp}	Spacer porosity	0.60	
p_{ma}^{AC}	AC macroporosity	0.4	
p_{mi}^{AC}	AC microporosity	0.3	
p_{ma}	Overall macroporosity at 5% loading	0.05	
p_{mi}	Overall microporosity at 5% loading	0.91	
A	Cell projected area	11.9	cm^2
$C_{st\text{-}vol,0}$	AC microporous Stern layer capacitance at zero charge	120	F mL^{-1}
D_e	Effective diffusion coefficient	1.68×10^{-5}	cm^2 s^{-1}
D_{mem}	Diffusion coefficient in the membrane	1.12×10^{-5}	cm^2 s^{-1}
L_{elec}	Electrode thickness	0.2	cm
L_m	Ion exchange membrane thickness	0.015	cm
L_{sp}	Spacer thickness	0.05	cm
N	Number of subcells	8	
R_{esr}	Equivalent series resistance	660	Ω cm^2
X	Fixed charge density of ion exchange membrane	3	mol L^{-1}